Title
Field methods for collection of spatially distributed, hydrologic watershed data

Author
Chung, Michaella

Publication Date
2018

Peer reviewed|Thesis/dissertation

Field methods for collection of spatially distributed, hydrologic watershed data

by

Michaella Chung

A dissertation submitted in partial satisfaction of the
requirements for the degree of
Doctor of Philosophy

in

Engineering - Civil and Environmental Engineering

in the

Graduate Division

of the

University of California, Berkeley

Committee in charge:

Associate Professor Sally Thompson, Chair
Professor Mark Stacey
Professor Mary Power
Associate Professor Carrick Detweiler

Spring 2018

Field methods for collection of spatially distributed, hydrologic watershed data

Abstract

Field methods for collection of spatially distributed, hydrologic watershed data

by

Michaella Chung

Doctor of Philosophy in Engineering - Civil and Environmental Engineering

University of California, Berkeley

Associate Professor Sally Thompson, Chair

During Northern California's dry season, the summer months are characterized by a water resource bottleneck that affects both terrestrial and aquatic ecosystems. Though the sensitivities of these summer-dry watersheds to environmental variability are frequently studied, spatiotemporal improvements in monitoring of watershed variables are undoubtedly beneficial in the context of ongoing climate change.

This dissertation presents innovative field methods to observe and record spatially heterogeneous and distributed watershed data that are essential for accurate evaluation of a Northern California watershed's water budget and thermal regime. This work focuses on two hydrologic fluxes providing dry season relief to vulnerable vegetation and freshwater species: fog water in the atmosphere and groundwater in streams. For each flux, a new field method employing a combination of commercially available sensors, remote sensing, and robotics is first developed and tested; the method is then used to describe or quantify the flux in a case study. Where appropriate, field studies are followed by modeling approaches that allow extensive analysis of a broader range of conditions than could be observed in the field. The direct observations made by employing the new field methods and subsequent analyses presented indicate the importance of improving accuracy of measurements of these hydrologic fluxes in understanding their watershed-scale effects. This dissertation also identifies operational and system constraints of the new methods, as well as key areas for further development, such that these methods may eventually be generally applied across all seasonally-dry, Mediterranean-type climate watersheds.

Contents

List of Figures

List of Tables

Acknowledgments

Many thanks to my advisor, Professor Sally Thompson, for her mentorship and guidance in both my research and teaching pursuits; the Thompson Lab for their help and encouragement both in the field and in our office; my partner, Daniel Braz, for his love and laughter through my graduate school years; and my family, Seum Chung, Lauren Suh, and David Chung, the most unfailing supporters through all of my endeavors.

This research was supported by the USDA National Institute of Food and Agriculture project #2013-67021-20947 and the National Science Foundation Graduate Research Fellowship Program.

Chapter 1

Introduction

1.1 Dry-season hydrology in Northern California

In seasonally-dry ecosystems, periods of high water availability are followed by extended intervals of very low precipitation (Fatichi et al., 2012; Feng et al., 2012; Joffre et al., 1999). Specifically, in Mediterranean-type climates such as in Northern California, the dry season coincides with the summer, and the combination of lack of precipitation and warm atmospheric conditions results in a growing water budget deficit during a period of peak ecosystem productivity that affects both terrestrial and aquatic ecosystems. Therefore, monitoring the dry-season hydrologic balance and thermal regime is essential to developing an understanding of the sensitivities of watershed vegetation, fish, amphibians, and invertebrates to environmental variability. The importance of characterizing these summer-dry landscapes to the conservation of watersheds and the variety of species they support is only likely to increase as the global climate warms (Dominguez et al., 2012). However, the highly spatially heterogeneous nature of such watersheds poses a challenge to hydrologists in collecting relevant watershed data and relating them to environmental drivers.

During the dry season in coastal forests and scrublands, limited availability of water resources coupled with high air temperatures and vapor pressure deficits result in plant water stress (Adams et al., 2009; Allen et al., 2010; Vico and Porporato, 2010; Xu and Baldocchi, 2003). However, because the dry season and fog season coincide in Mediterranean-type climates (Fischer et al., 2009; Peace, 1969; Schemenauer and Cereceda, 1991), fog can directly influence this limited water availability by providing a supplementary flux of water into the watershed or indirectly through evapotranspiration suppression. The ecohydrologic benefits of dry-season fluxes of fog water are currently well-understood: Fog can serve as a crucial source of relief for summer water deficits in coastal vegetation (Breazeale et al., 1950; Burgess and Dawson, 2004; Dawson, 1998; Haines, 1952, 1953), thereby increasing ecosystem drought resilience.

Because fog advects horizontally and close to the ground, heterogeneity in vegetation cover and a topographically complex terrain are likely to generate highly complex but non-

random spatial heterogeneity in fog water fluxes to the terrestrial ecosystem, with terrestrial fluxes of fog water varying with topography and vegetation distribution (Azevedo and Morgan, 1974; Ewing et al., 2009; Fischer et al., 2009; Vogl, 1973; Weathers et al., 1995) and with vegetation canopy roughness (Dawson, 1996; Shuttleworth, 1977; Wang et al., 2006) along its advective pathway. Current methods to estimate rates of fog throughfall, however, are similar to those for non-occult precipitation and rely on point-scale sampling, whose ability to capture spatial heterogeneities are limited by the density and distribution of measurement locations. Furthermore, traditional interpolation methods that assume negligible correlation between point observations beyond a certain distance (Bacchi and Kottegoda, 1995) are not suitable considering the non-random nature of fog.

In ponds and streams, abiotic drivers regulate freshwater ecological structure: Changes in the thermal regime of surface water not only affect water quality (Alabaster and Lloyd, 2013), but also threaten habitats for populations with low physical tolerance for high temperatures (Bernardo et al., 2003; Daufresne et al., 2007; Daufresne and Boet, 2007; Power et al., 2015). Small, isolated ponds in complex topography currently serve as dry-season habitat for threatened amphibians and are critical for the survival of many species. In addition to disturbances to landscape and pond hydrology (Fellers et al., 2011; Fisher and Shaffer, 1996; Johnson and Chase, 2004) that alter the nutrient and water balance of the ponds, changes in water temperature can increase the presence of disease-causing organisms (Johnson and Chase, 2004; Johnson et al., 2007; Sparrow, 1968) to exacerbate habitat vulnerability. Water temperature also plays a significant role in determining habitat quality in streams, where salmonid fishes are dependent on thermal refugia during the summer. When the low-flow stream water temperatures exceed the optimal range of many of their physiological functions, groundwater-sourced inflows from tributaries (Ebersole et al., 2015; Sutton et al., 2007) and seeps (Bjornn and Reiser, 1991; Brunke and Gonser, 1997; Constantz, 1998) have been observed to interact with the main stem flow to create cold-water zones that are critical for freshwater biota that depend on cooler water temperatures.

Significant thermal gradients arise both vertically in the water column and in the horizontal plane in freshwater bodies, with such thermal variability compounded by a spatially heterogeneous landscape, including the presence of bank-side shading, confluences, and deep pools (Crook and Robertson, 1999; Ebersole et al., 2003). Empirically characterizing this heterogeneity in thermal structure is non-trivial, but the observation techniques for measuring temperatures of water bodies are constrained by cost of instrumentation and field and deployment conditions. Moreover, all methods have tradeoffs between spatial resolution, temporal resolution, and spatial coverage of observations (Buck and Null, 2013; Ebersole et al., 2001, 2003; Matthews and Berg, 1997; Torgersen et al., 2001), rendering it difficult to observe detailed three-dimensional (3D) thermal structures of ponds or streams and to understand the extent of suitable critical habitat across a large watershed.

This dissertation develops innovative observation approaches based on fusing multiple sensors and data streams to obtain spatially heterogeneous and distributed watershed data. The focus is on seasonally-dry climates, with watersheds from Northern California as case studies. The dissertation consists of two parts:

- Part I: Part I focuses on the development of a novel upscaling scheme to estimate a watershed-scale flux of fog water and assess the quantitative impact of summer coastal fog on the watershed hydrologic balance.
- Part II: Part II focuses on the development of an unmanned aerial system (UAS) platform to measure water temperatures and recreate existing 3D thermal structures. This work also addresses potential applications of the UAS to answer questions related to vulnerable dry-season freshwater habitat.

1.2 Part I: Quantifying fog water flux

Part I of this dissertation addresses a new spatial averaging method based on a stratified sampling design that upscales spatially distributed, local observations of throughfall inputs and evapotranspiration rates to a watershed-scale estimate of a fog water flux.

Chapter 2 overview

A mechanistic evaluation of fog effects on a watershed's dry-season hydrologic balance and the relative importance of direct fog water inputs vs. reduced evapotranspiration demand during fog events is lacking, to date, because it requires estimates of fog water input at watershed scales. In this chapter, the role of coastal fog is empirically characterized through monitoring of the various mechanisms that affect fog occurrence and extent: throughfall following canopy interception of fog, soil moisture, streamflow, and meteorological variables. A stratified sampling design, which uses multiple sensor and remote sensing data to capture a watershed's spatial heterogeneities relative to fog events, is incorporated into a new spatial averaging scheme, which upscales such point-scale observations to watershed-scale estimates of fog water fluxes. The upscaled estimates compare well to traditional interpolation approaches but the new combination of data types is shown to improve the consideration of spatially-averaged fog fluxes into the water balance. The presented scheme is applied to a coastal watershed on the San Francisco Peninsula to show that while fog's throughfall inputs are small in volume, fog's suppression of evapotranspirational loss can reduce summer water deficits by a significant amount at watershed scales.

The work presented in this chapter is published in *Hydrological Processes* (Chung et al., 2017) and was conducted in collaboration with the San Francisco Public Utilities Commission. I contributed to this work by conceiving and designing the sensor deployment in the field, analyzing data, and creating the new spatial averaging scheme.

1.3 Part II: Characterizing surface water thermal variations

Part II of this dissertation addresses the development of a UAS platform that is custom-equipped with an immersible pressure-temperature sensor system to measure water temperature. Remote yet direct observations of water temperature from aerial platforms are attractive because they do not require shoreline access or ingress into the water body; they can be quickly and repeatedly deployed to sampling locations to make multiple measurements. The measurements made by a UAS are, as with all temperature sensing methods, constrained by system and environmental limitations, which may limit its advantage over traditional methods. The UAS platform is tested in both lentic and lotic ecosystems to evaluate its ability to measure water temperatures against in situ sensors; the platform's effects on the environment are also explored. Its temperature sensing abilities are then applied to two critical freshwater habitats during the dry season to evaluate whether the UAS can improve collection of spatially distributed water temperature data across a watershed and facilitate better understanding of these aquatic habitats and their thermal heterogeneities.

Chapter 3 overview

Understanding the thermal structure of surface water bodies is essential in assessing the heterogeneous drivers of critical habitat provision, yet obtaining 3D, fully-resolved observations of thermal structure remains challenging. This chapter introduces a UAS platform that lowers a temperature sensor into shallow water to record temperatures throughout a water column. Initial field experiments at a lake in the Southern Coast Range show that the system is able to recreate mean variations in space and time of temperature as recorded by in situ sensors, and mixing disturbances induced by the aerial vehicle are observed to be comparable in magnitude to natural sources of perturbation in the water.

The work presented in this chapter is published in *Water* (Chung et al., 2015) and was conducted in collaboration with the NIMBUS Lab at University of Nebraska-Lincoln, which developed the UAS platform. I contributed to this work by conceiving and designing the field experiments, performing the experiments, and analyzing data.

Chapter 4 overview

Anthropogenic changes that drastically alter natural water bodies are driving a global extinction of amphibians, but evaluation of the effects of land use and hydrologic variation on habitat quality is hindered by the non-linear and bistable nature of shallow lake ecosystems, as well as their location in a topographically complex landscape. In this chapter, a potential application of the UAS is introduced: temperature measurements and sampling of water in vernal pools and farm ponds that serve as critical habitat for amphibians in the Southern Coast Range. This data can allow better understanding of the effects of hydrologic variation

and grazing practice on water quality, as well as the relationship between water temperature, nutrient concentration, and disease presence. Using water samples adhering to the UAS payload from ponds across sites with variable grazing measures, a novel environmental DNA (eDNA) technique is employed and standard water quality tests are conducted to explore nutrient concentrations and the presence of two disease-causing organisms, *Ribeiroia ondatrae* and *Batrachochytrium dendrobatidis*. However, published eDNA methods and thus this application of the UAS are shown to be unsuitable, with repeated trials of methods unable to detect either organisms in ponds with positive detection through host sampling or a history of disease presence.

Chapter 5 overview

Summer thermal refugia generated by cold-water stream inflows are important for many aquatic species, but understanding the extent of these cold-water zones remains challenging due to the difficulties associated with observing small-scale temperature heterogeneities over large, distributed river systems. This chapter focuses on tributary-main stem confluence mixing and groundwater discharge, two processes that can result in thermal refugia, to evaluate the overall field performance of a UAS temperature monitoring platform introduced in Chapter 3 and to explore the use of UAS-derived temperature data to reconstruct 3D thermal structures through idealized modeling and synthetic sampling. Though the UAS is observed to be comparable to in situ sensors in resolving flow behavior and the thermal structures of cold-water zones, flight operations challenges and stream mixing processes govern the scale of resolvable thermal structures, constraining this platform's use to small and shallow stream reaches.

This work was conducted in collaboration with the NIMBUS Lab at University of Nebraska-Lincoln. I contributed to this work by conceiving and designing both the field experiments and modeling study, and analyzing data.

Chapter 6 overview

In addition to fine-scale thermal characterization of thermal refugia, identification of these cold-water zones along a river network is essential for evaluation and management of critical freshwater habitat during the dry season. However, sites of groundwater entry to a stream and the resulting groundwater-fed cold-water zone are difficult to detect. In this chapter, a modeling study shows that cold-water zones with surface thermal signals can be created by groundwater-surface water mixing in a variety of cases of flow and groundwater intrusion. These cases represent the larger-volume and potentially oxygenated zones, suggesting that thermal infrared (TIR) imaging, previously used in habitat assessment by discerning the surface expression of groundwater thermal signals, may be a suitable method for detecting potential thermal refugia along a stream. This chapter also explores the operational and technical challenges that may limit the use of TIR on-board a small UAS vehicle for this application.

Part I

Quantifying fog water flux

Chapter 2

How much does dry-season fog matter? Quantifying fog contributions to water balance in a coastal California watershed

2.1 Introduction

Advection fog is a widespread phenomenon associated with deep marine upwelling along western continental margins worldwide (Garreaud et al., 2008; Leipper, 1995). It consists of liquid-phase water with droplet sizes ranging from 1–40 µm (Prada and da Silva, 2001), small enough for droplets to be advected with wind. Fog events are thus influenced by time-varying meteorological variables such as wind speed, direction, and dew point (Azevedo and Morgan, 1974; Hiatt et al., 2012; Weathers et al., 1995, 2000), which affect the size, density, and flux of these water droplets. Fog interaction with the terrestrial water balance occurs in three ways: climatically, through reductions in radiation, temperature, and vapor pressure deficit, which collectively suppress evapotranspiration during fog events (Fischer et al., 2009); through direct water inputs, when fog droplets are intercepted by vegetation canopies and form a non-rainfall water flux that reaches the soil as canopy throughfall (Dawson, 1998; Hutley et al., 1997); or indirectly by alleviating water stress in plant leaves when absorbed through foliar uptake (Burgess and Dawson, 2004; Wang et al., 2017) and reducing transpirational loss (Ewing et al., 2009; Templer et al., 2015). Fog water inputs and transpiration suppression can also enhance streamflow fluxes: Isotopic tracing has unambiguously identified the signature of fog water within soil moisture, groundwater, and streamflow (Ingraham and Matthews, 1988, 1995; Scholl et al., 2002). Furthermore, dry-season streamflow fluctuations correlate with fog occurrence (Sawaske and Freyberg, 2015) and respond to interception mechanisms through changes in vegetation cover (Harr, 1980, 1982; Ingwersen, 1985; Keppeler, 2007). Because fog zones coincide with large arid, semi-arid, and Mediterranean climate zones, and

because the fog season may also coincide with dry seasons in these regions (Fischer et al., 2009; Peace, 1969; Schemenauer and Cereceda, 1991), fog can have a significant contribution to the water balance and may increase ecosystem drought resilience (Breazeale et al., 1950; Burgess and Dawson, 2004; Dawson, 1998; Haines, 1952, 1953).

Fog advects horizontally and close to the ground, and thus terrestrial fluxes of fog water vary with topography and vegetation distribution along its advective pathway. Typically, fog inputs peak along topographic ridges and forest edges (Azevedo and Morgan, 1974; Ewing et al., 2009; Fischer et al., 2009; Vogl, 1973; Weathers et al., 1995), and vary with vegetation canopy roughness (Dawson, 1996; Shuttleworth, 1977; Wang et al., 2006). Heterogeneity in vegetation cover and a topographically complex terrain are therefore likely to generate high spatial heterogeneity in fog water fluxes. This poses a challenge in making spatially integrated estimates of fog effects on a system water balance. Most methods to estimate rates of fog throughfall rely on point-scale sampling, which has a limited ability to capture important spatial heterogeneities due to the finite density and distribution of measurement locations. Moreover, the spatial patterns adopted by fog are complex, but not random. Hence, traditional methods that assume negligible correlation between point observations beyond a certain distance (e.g., Thiessen polygon or kriging (Bacchi and Kottegoda, 1995)) are not suitable for interpolation between sampling points. Development of spatially integrated estimation techniques that can address the complex but non-random nature of fog, as well as its interaction with a heterogeneous land surface, are needed to allow quantitative evaluation of the importance of fog water fluxes at watershed scales.

Therefore, this study seeks to answer the following questions:

1. What are the dominant controls that characterize heterogeneity of fog in a seasonally-dry, coastal watershed?

2. In what ways does fog contribute to the water balance of this system and how significant are its quantitative effects?

3. How important is each sensor and its dataset in inferring fog's watershed-scale effects?

In this study, we characterize and quantify spatiotemporal heterogeneity in fog events and deposition in a small, coastal Northern California watershed during a period of extreme drought. By developing a novel spatial averaging scheme that accounts for watershed features and meteorological variables, we upscale these observations and make quantitative estimates of the hydrologic effects of fog within the watershed. We then explore the sensitivity of the upscaling scheme to changing data types, data density, and specific interpolation schemes employed while upscaling. The results highlight the importance of considering the non-random pattern of fog events when extrapolating point-scale observations to understand the hydrologic implications of fog at ecosystem levels.

2.2 Materials and methods

Site description

The Upper Pilarcitos Creek Watershed is a 9.6 km^2 watershed with a 630 m rise in elevation, located on the San Francisco Peninsula within the Santa Cruz Mountain range and draining into Lake Pilarcitos. It is one of the oldest components of San Francisco's water supply system and is managed within the larger Peninsula Watershed by the San Francisco Public Utilities Commission. The coastal, western divide of the watershed is covered by dense, old-growth Douglas fir forest (*Pseudotsuga menziesii*) and is characterized by highly uncompacted soil. Most of the eastern watershed is covered by chaparral rangeland; its dominant vegetation is coyote brush (*Baccharis pilularis*). The watershed averages approximately 100 cm of rain per year. It is also subject to frequent coastal fog events in summer, which, depending on wind direction, can either approach the watershed from the west, rising over a coastal ridge, or from the north or south, flowing through the river valley. During these events, the canopy of understory vegetation becomes thoroughly wet and pools of water collect beneath trees, although neighboring grasslands remain dry (Potter, 2016); up to 150 cm of throughfall were observed over a single month under a forest canopy within a neighboring watershed (Oberlander, 1956).

Field methods

We deployed a suite of sensors at multiple sites in the Peninsula Watershed during three summer fog seasons coinciding with the dry season, spanning June–October in 2014, 2015, and 2016 (Figure 2.1). The Peninsula Watershed is a single geologic and topographic unit in the coastal range and experiences no geologic, vegetation, or elevation change across sub-watershed boundaries created by a reservoir dam. Observation sites were located in the Upper Pilarcitos Creek Watershed and its neighboring watersheds, which share common directional gradients in fog presence. Sites were selected to represent locations with different elevation, vegetation, wind conditions, and ocean exposure, along with variations in fog frequency, density, and approach pathways to the watershed, as reported by on-site watershed managers. Ultimately, six sites were selected covering areas of peak fog intensity (Scarper Peak and Montara Mountain, associated with a frequently occurring west-east fog pathway) and areas of less frequent fog occurrence (Spring Valley, associated with some west-east and north-south fog pathways, and Cahill Ridge, associated with a south-north fog pathway) according to operator information. Site selection, however, was constrained by accessibility limitations associated with a steep topographic slope and the presence of endangered plant and animal species, which limited sampling to locations near roads at the ridgelines and a single east-west road that spans the topographic gradient of the watershed.

Each monitoring site consisted of a throughfall collector (sloping trough: 0.3 m diameter and 1.8 m length), installed 0.6 m above ground level, and one Juvik-type radial collector (Juvik and Nullet, 1995) consisting of a 24 cm radius circular mesh, installed at 1.8–2.5 m

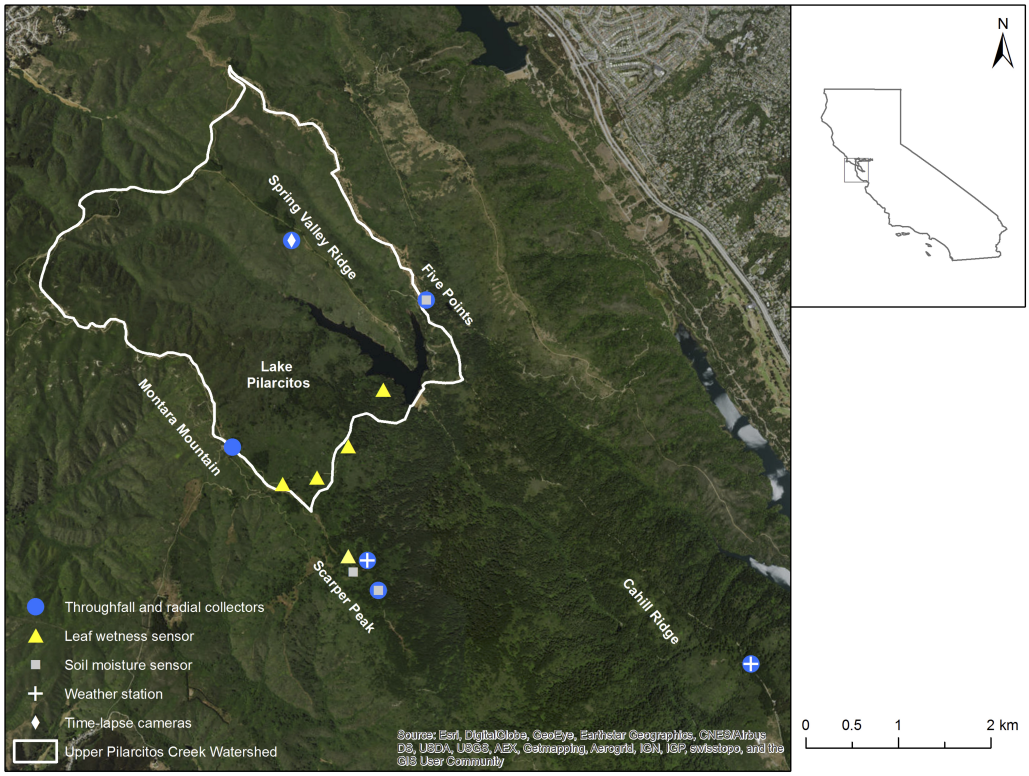

Figure 2.1: Map of Upper Pilarcitos Creek Watershed: study sites and instrumentation locations.

above ground level. Each collector routed water through a sealed pipeline to its own tipping bucket rain gauge (Campbell Scientific TE525WS) recording on 5 minute intervals. The two collectors were used to separately measure the vertical fog drip below the forest canopy (throughfall collector) and the horizontal component of wind-driven fog, or the amount of water transported horizontally by fog through the canopy system (radial collector). We interpret the radial collector data to provide an index of the advection fog flux density (volume water per area per time), allowing comparisons to be made between similar fog events in different locations. The fog collection sites spanned elevations from 245 to 580 m on both the west- and east-facing hillslopes (Figure 2.1 and Table 2.1) and covered the two dominant vegetation types of the watershed: Douglas fir forest and coyote brush scrub. The east-facing forest sites were located under varying forest conditions, with Montara Mountain at the forest edge and both Scarper Peak sites further in the forest stand.

Additionally, a weather station was deployed on each hillslope of the watershed. The weather stations (HOBO H21-002 Micro Station) logged local air temperature and relative

Site	Elevation (m)	Dominant vegetation	Distance from forest canopy edge (m)	Aspect
Five Points	258	DF	91	W
Cahill Ridge	321	DF	122	W
Spring Valley Ridge	329	CB		W
Scarper Peak 1	554	DF	135	E
Scarper Peak 2	581	DF	197	E
Montara Mountain	548	DF	20	E

Table 2.1: Descriptions of each study site in the Peninsula Watershed. DF is Douglas fir and CB is coyote brush canopy; W indicates west-facing and E indicates east-facing hillslopes.

humidity. A third weather station, a Remote Automatic Weather Station (RAWS), was already present at Spring Valley Ridge and recorded hourly precipitation, wind, solar radiation, temperature, and relative humidity. At three sites, soil moisture sensors (Decagon 5TM time domain reflectometers) were installed 75 mm and 300 mm below the surface to measure the soil volumetric water content (VWC) and temperature responses to fog drip; these sensors measure VWC using capacitance/frequency domain technology to determine the dielectric constant of soil and measure temperature using a built-in thermistor. Additionally, five leaf wetness sensors (Decagon LWS) were deployed, four along a topographic gradient on the east-facing hillslope and the fifth sensor co-located with a fog collection site in the forest stand. The leaf wetness sensors measure the accumulation of water on a surface with equivalent thermal properties to a leaf. All leaf wetness sensors were placed horizontally, 1–2 m off the ground in the under-storey of even-aged Douglas fir stands, minimizing the effect of vegetation change on observed wetness. During a fog event, accumulation of water is presumed to derive from fog impaction. This deployment is widely used to sample fog occurrence and strength, as it provides a relatively stable range of response to leaf surface wetness and minimizes water running off the sensor surface for small collected water volumes (Cobos, 2013). Two time-lapse cameras (Brinno TLC200), recording images at thirty minute intervals with viewsheds facing west and southward and aligned with major fog flow pathways, were installed on Spring Valley Ridge. Lastly, Landsat images from 1991–2011 and 2014–2016 were collected. All data were complemented by notes from weekly field visits, during which visual observations of fog presence and location were recorded.

Stream water, non-green, non-photosynthetic stem and tissue (e.g., tree twigs), and soil samples were collected throughout the fog season in 2014 and 2015 for stable isotope analysis. Fog samples were collected at three sites using harp-style passive collectors (Fischer and Still, 2007) over a 24-hour period: The collectors were set up during a field visit with foggy conditions, and the samples were retrieved the next day to avoid evaporative effects. Water samples were extracted from stem and soil samples by cryogenic vacuum distillation and stable hydrogen and oxygen isotope compositions were determined at the Center for Stable Isotope Biogeochemistry at Department of Integrative Biology, University of Califor-

nia, Berkeley. The ratio of concentration of deuterium to ^{1}H, δD, in water was analyzed in dual inlet (DI) using a hot chromium reactor unit (H/Device) interfaced with a Thermo Delta Plus XL mass spectrometer. Multiple standards were added to every run and different isotope ratios were used to correct for differential drift in standards. Long-term external precision is $\pm 0.80‰$. The ratio of concentration of ^{18}O to ^{16}O, δ^{18}O, in water was analyzed by continuous flow (CF) using a Thermo Gas Bench II interfaced to a Thermo Delta Plus XL mass spectrometer. A volume of water (20–200 µl, depending on the sample volume available) for both standards and samples was pipetted into 10 ml glass vials and quickly sealed. The vials were then purged with 0.2% CO_2 in helium and allowed to equilibrate at room temperature for at least 48 hours. The δ^{18}O in the CO_2 was then analyzed. Long-term external precision is better than $\pm 0.12‰$. For QA/QC, two lab standards were analyzed between every 20 samples.

Soil moisture analysis

Soil moisture-fog analysis was conducted using Pearson's correlation coefficient to estimate the linear correlation between soil VWC and fog throughfall data from one site (Scarper Peak 1). To evaluate changes in this correlation between different times of the fog season, we compared the correlation coefficient of the entire fog season (June-October) to the coefficient from early summer (June, July) and late summer (August, September).

Evapotranspiration estimates

We estimated potential open water evaporation from Lake Pilarcitos and potential evapotranspiration (PET) for forest and chaparral canopies using the Priestley-Taylor equation (Priestley and Taylor, 1972) and RAWS data and local data from deployed weather stations. Differences in open water evaporation and PET on foggy and clear days were used to estimate PET reduction due to fog for chaparral and forest canopy at a daily timescale. PET reduction estimates for each canopy were multiplied by the average number of foggy days per dry season to find a vegetation area-weighted estimate of avoided evapotranspiration loss for the watershed.

Reduction in solar radiation during a fog event was calculated by finding the average percentage reduction in daily solar radiation between clear and foggy days, classified based on fog collector data.

Upscaling scheme

The upscaling approach involved 8 steps, which are shown conceptually in Figure 2.2.

We assumed that the primary control on fog throughfall was the presence/absence of fog at any x-, y-coordinate location in the watershed. Based on discussions with watershed managers, visual field observations, time-lapse camera data, and analysis of Landsat records

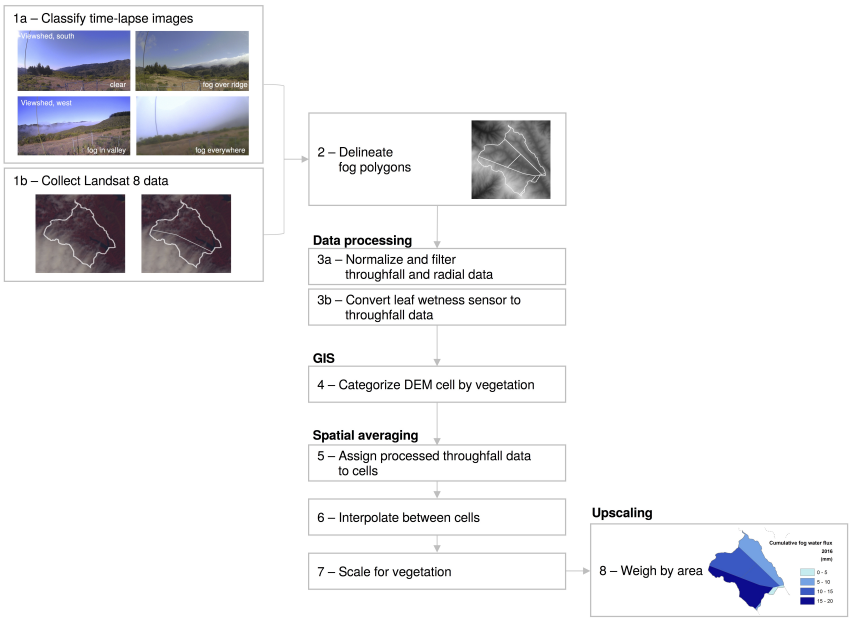

Figure 2.2: Schematic diagram of spatial averaging scheme.

over a 20-year period (1991–2011), we developed four classifications of fog extent, which were used to constrain the locations in the watershed over which fog occurred during any given event. We then assumed that the secondary control on throughfall occurrence was the elevation of the fog ceiling and thus the interaction of fog with local vegetation canopy. This fog ceiling elevation was assumed to be homogeneous throughout the area in which fog occurred. The effect of watershed elevation on wetness, as a proxy for fog-canopy interaction, was accounted for using a transect of leaf wetness sensors that spanned the elevation range of the watershed. We note that other effects of elevation, for example on temperature and moisture in the atmosphere, are generally negligible over the elevation range in the Upper Pilarcitos Creek Watershed under conditions of the Californian coastal climate (Mooney and Zavaleta, 2016). Furthermore, because different vegetation canopies exhibit varying roughnesses and vertical extents, we expected different quantities of throughfall under different canopies given fog presence at a given elevation. These tertiary canopy-related effects were controlled for by comparing throughfall for equivalent densities of advection fog between different vegetation types.

Therefore, the upscaling scheme firstly subdivides the watershed into places where fog occurs or does not, then controls for variations in the cloud ceiling within the fog-bound areas, and then adjusts these factors using vegetation to make an estimate of throughfall. This approach implicitly assumes that the elevation of the fog ceiling is comparable across the area where fog occurs and independent of vegetation type, and that there are no additional

interactions between throughfall, watershed elevation, and vegetation — an assumption supported by the well-mixed atmospheric conditions that typically prevail in the California coastal area.

We note that our upscaling scheme focuses on the Upper Pilarcitos Creek Watershed, located at the upper half of the Peninsula Watershed, as water balance computations can occur at the dam, but this boundary is not physical and has no influence on fog dynamics.

Step 1: For each day during the fog season, we manually classified time-lapse images from 7 a.m. to 3 p.m. according to fog presence and location within each camera's viewshed. This time window was chosen as images from outside this window were too dark for classification. The first camera's viewshed included Montara Mountain and its east-facing hillslope, while the second camera's viewshed included Scarper Peak and its east-facing hillslope. Four classifications were used for each viewshed: clear, fog over ridge, fog in valley, fog everywhere. All images could be unambiguously classified into one of these groups. The "clear" classification was used when there was no interaction of fog or low-lying clouds with the vegetation canopy in the image. The "fog over ridge" classification was used when fog was interacting only with the canopy along the ridgeline and the "fog in valley" classification was used when fog was observed only at low elevations on the hillside. The "fog everywhere" classification was used when the entire image was blurred by fog.

Next, the classified images were compared to images from Landsat 8. We collected remote sensing images from the same time period showing fog over the watershed. By relating the broad spatial patterns seen in the Landsat images to each of the four classifications from the time-lapse images, we were able to delineate general coverage extents of each classification. Although only 5 fog images could be identified that overlapped with the study period, Landsat 5 images from fog seasons over a 20-year period, as well as watershed site visits, confirmed the four patterns. These boundaries, which most importantly show the edge line of the typical fog event in the watershed, were drawn in ArcGIS to create Landsat polygons.

Step 2: A set of Thiessen polygons was created in ArcGIS using the larger Peninsula Watershed boundary and all throughfall collector locations. These polygons were then trimmed to the Upper Pilarcitos Creek Watershed, noting the importance of boundaries in precipitation interpolation (Dale and Fortin, 2014). The boundaries of the Thiessen polygons were combined with those of the Landsat polygons from Step 1 by overlapping the two sets of polygons' boundaries. These new polygons consider the distance-based spatial correlations that form the basis of conventional interpolation methods while retaining the spatial extents of the fog events that occur in the watershed. The polygons act as the general framework for our spatial averaging scheme.

Step 3: The throughfall and radial collector data were normalized and filtered for any rainfall using precipitation data from the RAWS to isolate the effects of fog on the water budget. Because fog can register on a rain gauge but at much smaller volumes than rainfall, we compared two rain gauges, one located at the RAWS, where fog occurs, and the other

located at Lake Pilarcitos, where fog is rare due to low elevation, to find a threshold rain gauge reading for rainfall water inputs. Precipitation was assumed to be rain-derived if RAWS-recorded data exceeded 0.25 mm per precipitation event, and throughfall and radial collector data from those time periods were set to zero so that we would not include rainfall water measurements in our fog water estimates.

Step 4: Using a vegetation map superimposed on a 3 m digital elevation model (DEM) of the Upper Pilarcitos Creek Watershed in ArcGIS, we categorized each elevation cell (3×3 m pixel) according to land and vegetation type (e.g., water, chaparral, forest). The DEM was then disaggregated into smaller DEMs corresponding to the polygons from Step 2.

Step 5: For each 5 minute time step, we assigned a subset of gauge points for each polygon. Each gauge point describes a location used in interpolation (Step 6) within each polygon. In polygons containing a fog measurement site, the site (with its throughfall data and elevation) served as the main gauge point, and secondary gauge points were the leaf wetness sensors. In polygons that did not enclose a fog measurement site, such as those covering the area between Montara Mountain and Spring Valley Ridge, data from another fog measurement site was assigned to the main gauge point, based on the time-lapse image classification and thus presence and location of fog at the time step. For example, in a polygon between Montara Mountain and Spring Valley Ridge, the main gauge point was set to zero for a "fog over ridge" classification because the time-lapse image showed fog only over the Montara Mountain ridge; for a "fog in valley" classification at another time step, for which the time-lapse image showed fog only in the lower elevations, the main gauge point was assigned throughfall data from Spring Valley Ridge, an adjacent lower elevation site. For a "clear" classification, when no fog was observed in any polygons by the time-lapse image, the main gauge point was set to zero.

Step 6: Within each polygon, the elevation cells that matched the elevations for the main and secondary gauge points were assigned corresponding data. Assuming a linear increase of moisture with elevation, we interpolated throughfall values for the remaining elevation cells. This assumption was based on regression analysis of throughfall data, which showed a linear effect of elevation on throughfall. Two sets of data from three fog seasons were considered: 1) daily throughfall data given fog presence from fog collectors from all forested sites except for Montara Mountain, spanning a range of elevation with similar forest stand conditions and 2) potential throughfall from leaf wetness sensor data from the four sites along a topographic gradient. Leaf wetness counts were converted to corresponding throughfall values to estimate potential throughfall from leaf wetness sensors: Previous work (Koohafkan et al., rial) using a simulated fog chamber showed that leaf wetness sensors respond near-linearly to wetness inputs below a sensor reading of 820 counts, and therefore, given a wetness count value for dry conditions, it is possible to predict fog water inputs from wetness counts. Though our range of leaf wetness counts exceeded 820, with the maximum around 1000 counts, we found that the difference between the linear relationship between throughfall and leaf wetness counts for

the range of sensor readings below 820 counts and the entire range observed was negligible. For each fog season, in which leaf water accumulation and throughfall total time series are stationary, we performed a regression to find a linear model that best predicts co-located throughfall volumes from leaf wetness counts (R^2=0.38–0.52). This linear model conversion provides supplementary estimates of potential throughfall at a higher spatial resolution along an elevation gradient.

Linear regressions on each set of data showed consistent and significant elevation scaling for throughfall (slope, m=0.0048 (data set 1), 0.0049 (data set 2)) despite noisiness of data (R^2=0.06 (data set 1), 0.15 (data set 2)). Therefore, fog collector throughfall data for the main gauge point and potential throughfall from leaf wetness sensors for the secondary gauge points were used to scale for elevation in the remaining elevation cells.

Step 7: To account for vegetation effects on throughfall (Section 2.3) and avoid over-estimation of throughfall in chaparral, we scaled down throughfall measurements in the chaparral elevation cells in polygons where the gauge points were under forest canopy. In polygons where the gauge points were under chaparal canopy, throughfall measurements in the forest elevation cells were scaled up. Water cells, with no vegetation, were set to zero.

Step 8: We found a polygon-scale throughfall estimate for each polygon by estimating an area-weighted average of each elevation cell's throughfall measurement. We then calculated a watershed-averaged throughfall by estimating an area-weighted average of the polygon-scale throughfall estimates.

Following this scheme, we developed a time series for watershed-averaged fog water flux for 2014, 2015, and 2016.

To evaluate the effect of the data sources and interpolation methods on our upscaling scheme, we compared the watershed-averaged estimates of fog water flux calculated from ten different schemes with varying data types. Our presented scheme uses data from all throughfall collectors and leaf wetness sensors, as well as time-lapse classifications, Landsat 8 imagery, the watershed vegetation map, and DEM (Table 2.2, Scheme 4). The nine other schemes were created using a factorial combination of the data sources, presented in Table 2.2. To evaluate the effect of data density, we systematically limited the number of throughfall collectors and leaf wetness sensors contributing to the final scheme.

2.3 Results

Observed heterogeneities in fog events and deposition

There were 89 foggy days in 2014, 74 in 2015, and 63 in 2016, occurring on 73%, 61%, and 52% respectively, of days during each dry season. Two approach pathways of fog to the Upper Pilarcitos Creek Watershed were identified, shown in Figure 2.3a: The most frequently

	Throughfall	Leaf wetness sensor	Landsat	Vegetation	DEM
1	×				
2	×	×			
3	×	×	×		×
4	×	×	×	×	×
5	×	×		×	×
6	×	×			×
7	×		×		
8	×		×	×	
9	×			×	
10	×	×		×	

Table 2.2: Sensors and datasets included in each upscaling scheme.

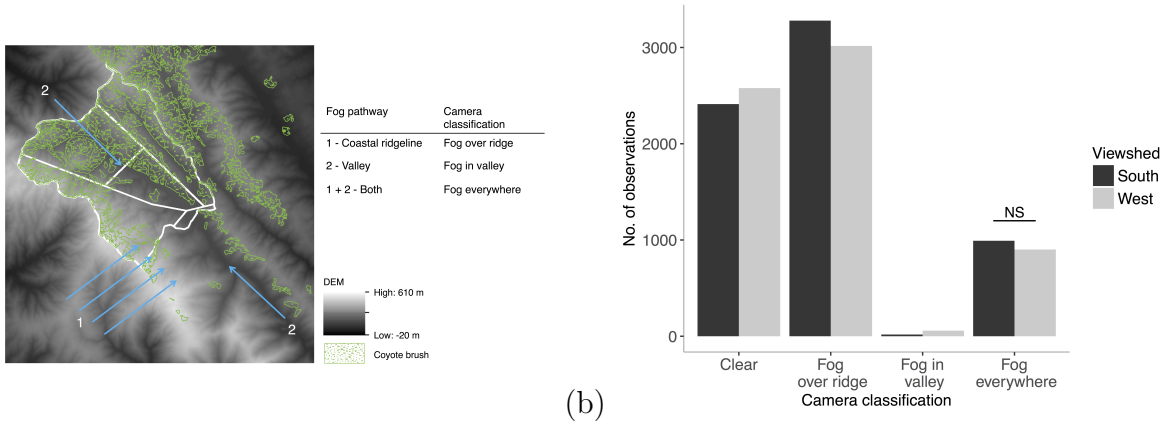

(a) (b)

Figure 2.3: Two fog pathways were identified in the watershed; the coastline ridge pathway was most frequent, resulting in fog's accumulation on the western ridge. The watershed and its neighboring watersheds share similar fog pathways, vegetation (dominant types and cover), and topographic gradients. In an analysis of camera viewsheds and fog classifications, all viewsheds and classifications were found to be statistically different except where noted in the figure.

occurring, around 83% of all foggy days, was over Montara Mountain from the coast, which caused the fog to accumulate on the western ridge of the watershed. The other, less frequent but concurrent when present with the first pathway, occurred in valleys, through which the fog travels 1) toward Lake Pilarcitos from its west fork branch and 2) to Cahill Ridge from the south; the valley pathways occurred around 17% of foggy days (Figure 2.3b).

The high-elevation, forest canopy sites on the east-facing hillslope received the highest amount of moisture from fog, with a decline moving down-slope and inland within the

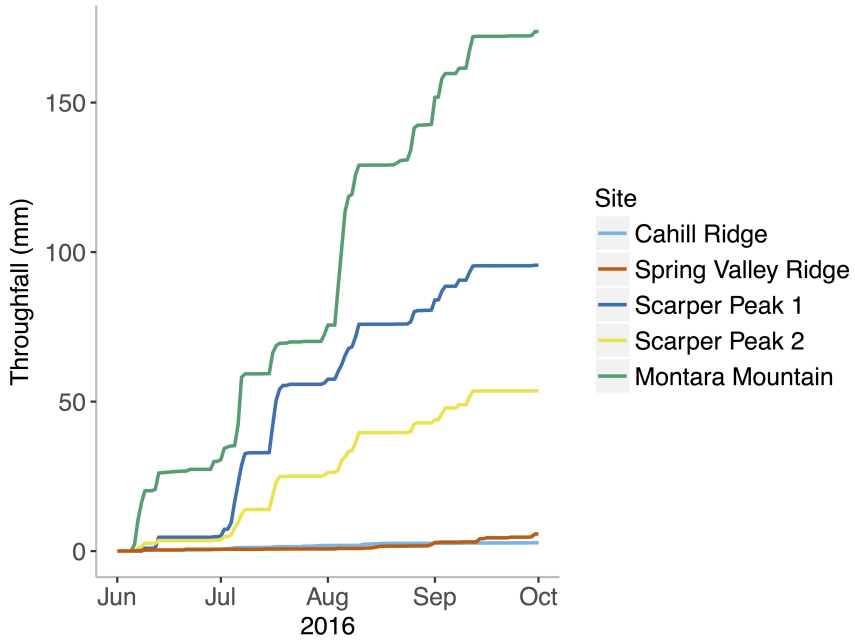

Figure 2.4: Cumulative throughfall at each fog study site in 2016: The high-elevation, forest canopy sites (Scarper Peak, Montara Mountain) on the western water divide, with direct ocean and wind exposure, received the highest amount of moisture from fog. Results from all three years are discussed in the text.

vegetation canopy. The forest edge site with direct wind and ocean exposure recorded up to three times the volume of seasonal cumulative throughfall compared to the sites located at similar elevation but situated >50 m within the forest stand (Figure 2.4, Montara Montain vs. Scarper Peak; illustrative data for 2016). The leaf wetness sensors also showed wetter conditions at the forest edge than interior (Figure 2.5a; illustrative data for 2016). However, frequency of wetness events (period of consecutive record) between forest edge and interior sites varied between years. In some years, the percentage of the season during which leaf wetness sensors recorded wet conditions was similar at both sites while in others, higher frequency of wetness events at the forest edge was observed. Leaf wetness counts generally declined with decreasing elevation along the east-facing hillslope (Figure 2.5b; illustrative data for 2016). The 400–500 m elevation band of the watershed experienced the wettest conditions for the highest portion of the dry season, with highest average leaf wetness counts observed around 470 m but also with higher variability at this elevation, while below 300 m, there was a sharp decrease in wet conditions.

We also observed differences in fog-derived moisture with vegetation type. For equivalent advection-fog intensities as measured in the radial collectors, less fog was captured

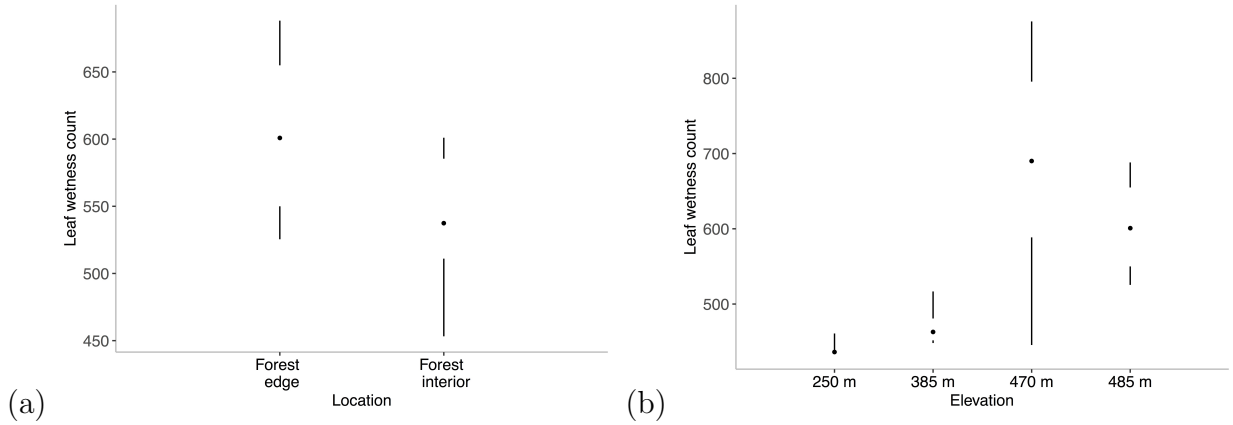

Figure 2.5: Box plot of daily average leaf wetness counts during a representative foggy period (2016) by a) site forest conditions and b) site elevation. Wetness counts generally decrease with elevation down a hillslope, and are reduced with distance into the forest stand during this illustrative period in 2016. Results from all three years are discussed in the text. The point indicates the median and the gap indicates the interquartile range. One site is presented for each category.

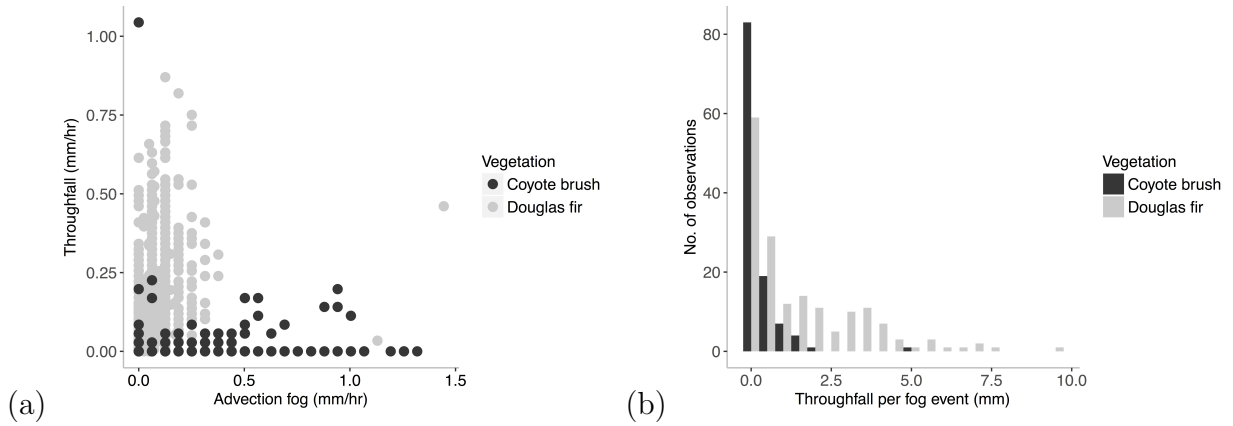

Figure 2.6: The difference in throughfall observations under chaparral and forest canopy are shown through a) the relationship between advection fog and throughfall in 2016 and b) a histogram of fog event size from 2014–2016.

under chaparral than forest canopy (Figure 2.6; illustrative data for 2016), although these differences varied in their magnitude: 5:1 vs. 6:1 vs. 28:1 in 2014 vs. 2015 vs. 2016. It is also important to note that because the radial collector measured advection fog at only one elevation per site, its data are unable to distinguish between the absence or reduced bulk intensity of fog and a lifting of the fog ceiling. In 2014 and 2016, advection fog occurred with higher frequency and intensity along the open, wind-exposed chaparral ridgeline of Spring Valley Ridge than on forested Scarper Peak; in 2015, advection fog intensity was similar at the two sites. For the same intensity of advection fog, lower throughfall measurements were observed at the chaparral site than at the forest sites. Furthermore, while the increase in fog advected through the canopy signifies greater availability of moisture for interception by vegetation, less throughfall occurred overall at the chaparral site than at the forest sites.

Lastly, the three study years showed considerable temporal variability in fog intensity and event size (Figure 2.7). Between 2014 and 2015, the size of the average fog event and fog event frequency decreased markedly at Spring Valley Ridge, with a a 62% decrease (21.5 vs. 8.2 mm/season) in throughfall. This was related to a 96% decrease (12.4 vs. 0.5 mm/season) in horizontal transport of fog measured by the radial collectors. At Scarper Peak, the size of the average fog event and fog event frequency remained the same between 2014 and 2015, though the frequency of high-volume fog events, or events recording volumes higher than the seasonal average, was reduced. Between 2015 and 2016, the size and frequency of fog events decreased further at Spring Valley Ridge (8.2 mm/season vs. 5.7 mm/season), though horizontal transport of fog increased at all sites to volumes exceeding those in 2014. At Scarper Peak, the size of the average fog event increased while fog event frequency decreased by a third from the previous year, resulting in similar throughfall volumes observed through the three years at this site.

Watershed-scale effects of fog on water balance

Using the upscaling scheme, we estimated a watershed-averaged monthly input of fog water flux of 6.7 mm contributing directly to the Upper Pilarcitos Creek Watershed during the 2014 fog season, an average of 2.6 mm in 2015 and 2.9 mm in 2016 ($\sigma^2 = 0.02$ mm). This results in 10–30 mm/year of additional water flux from fog, or 1–3% of the total water input to the watershed. The decrease in direct water input in 2015 and 2016 is largely due to the decrease in throughfall in interior, low-elevation chaparral sites, as recorded at Spring Valley Ridge, which represents much of the watershed area.

Soil moisture peaks under forest canopy were weakly positively correlated with fog events and correlation decreased with depth from the soil surface over the entire fog season (r=0.36, r=0.15 at 75 mm and 300 mm below surface). Such correlation coefficients are dependent on timing during the dry season, however, with values decreasing from the early months of the season (June, July) to the late months (August, September): r decreases from 0.46 to 0.21 at 75 mm and from 0.15 to no correlation at 300 mm below surface. The average volumetric water content of soil was greater following periods of persistent fog (3 or more consecutive days of fog events) than during clear, no-fog periods, at both depths in the soil column

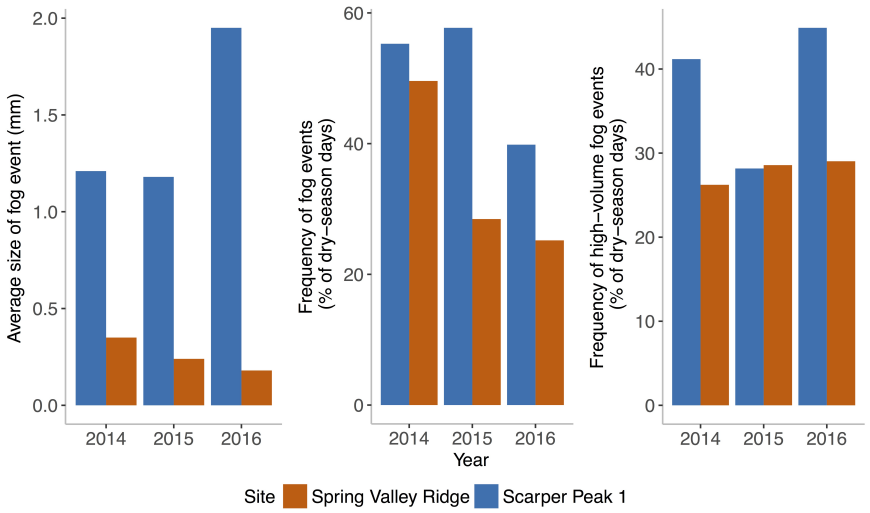

Figure 2.7: Comparison of average size and frequency of fog events shows interannual variability. High-volume fog events are events recording volumes higher than the seasonal average.

(p<0.05, one-sided t-test), but soil moisture responded only to throughfall percolating into the soil during above-average events (>1 mm/day; Figure 2.8).

The isotopic composition of fog, stream, soil, and stem water samples are presented in Figure 2.9. Fog water was enriched with heavy isotopes of deuterium and ^{18}O compared to rain. Though the isotopic signature of fog samples plot along the local meteoric water line, fog could not have been generated from local water sources given the proximity to the coast and the prevailing summer conditions. By contrast, stream water samples showed a similar isotopic signature to rain (i.e. depleted in composition) and exhibited little variation over time. Stem water, representing water sourced by vegetation, and shallow soil water samples exhibited similar isotopic composition to streamwater. The temporal variation in signature of soil water, however, did not correspond to trends in fog events (e.g., occurrence or duration), reflecting the low correlation between fog events and changes in soil moisture observed in the watershed.

During the fog season, the total PET was 570 mm. Changes in climatic variables resulted in a 9.5% decrease in potential open water evaporation from Lake Pilarcitos between clear and foggy days (3.3 vs. 3.0 mm/day). At a high-elevation, forested site with direct ocean exposure, there was a 37% reduction in PET on foggy days and, at the open, chaparral site, a 17% reduction. We note that the radiometer was located at the chaparral site, which often experienced clear conditions while the forested site was under fog. When fog events occurred, there was a 7% average reduction in solar radiation; considering this decrease on foggy days, we found a 41% reduction in PET at the forested site. Considering these magnitudes of PET reduction, there was an approximate decrease in transpiration demand of 125 mm/year from

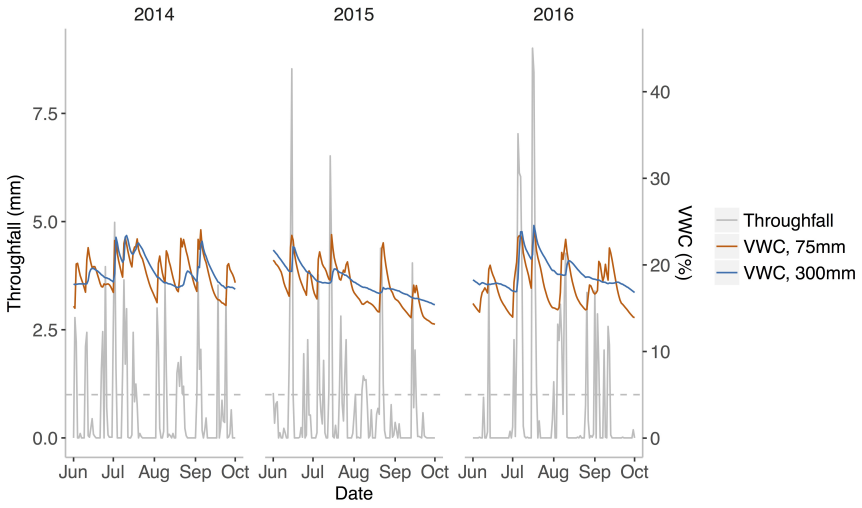

Figure 2.8: Normalized throughfall and volumetric water content of subsurface soil: Changes in soil moisture occur when fog events produce daily throughfall volumes greater than 1 mm, as indicated by the horizontal dashed line.

fog.

Sensitivity of upscaled values to data sources and interpolation methods

Relative to the final scheme with the highest information content, which we considered as our baseline estimate of watershed-scale fog water flux, the loss of data types in the nine other schemes resulted in increasing deviation from the baseline estimate. The increase in deviation from the baseline when supplementary watershed data was not included is shown as the difference in the three-season totals between each scheme and the final scheme, Δ, which increased when neither vegetation or elevation data were considered (Figure 2.10a). We found that the upscaled estimates were sensitive to an omission of vegetation cover data, while the omission of elevation data had a lower impact. The same trends were observed when comparing the average difference of upscaled totals at the original 5 minute time step. Once these data were added, the watershed-scale estimate remained sensitive to the inclusion of Landsat data: The use of Landsat-based polygons, which combine Landsat-observed patterns with Thiessen polygons per our upscaling scheme, generally resulted in a reduction in Δ. On the other hand, the use of Thiessen polygons created from throughfall collector locations resulted in increased Δ. Furthermore, Δ was reduced through an increase in number of throughfall collectors at forested sites on the east-facing hillslope, but fog water flux estimates were less sensitive to an increase in the number of leaf wetness sensors along

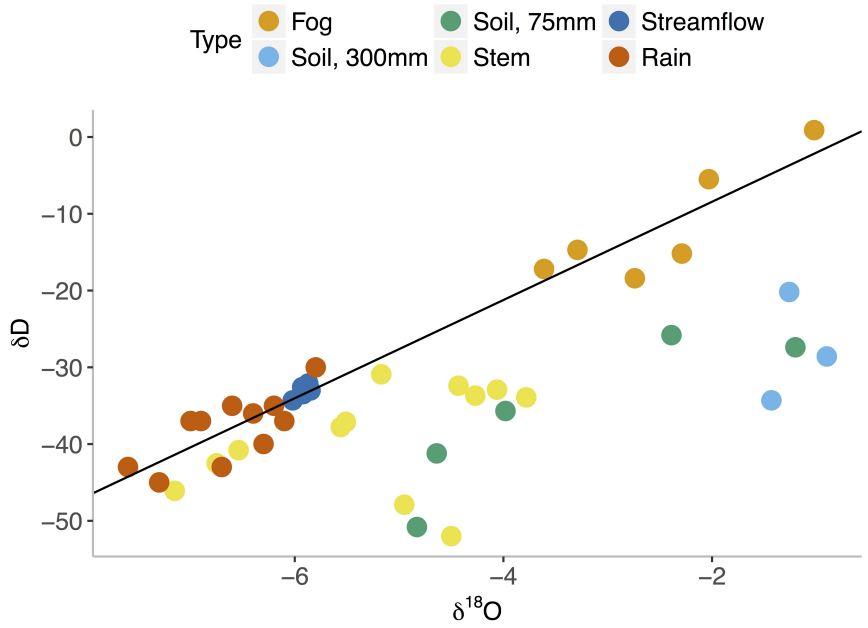

Figure 2.9: Dual isotope plot of water isotopes of rain (Ingraham and Matthews, 1995), fog, stream, soil, and vegetation stem. LMWL represents the local meteoric water line (based on fog and rain data: $\delta = 4.4 + 6.4\delta^{18}O$).

a topographic gradient (Figure 2.10b).

2.4 Discussion

The dominant controls of heterogeneity in fog occurrence and flux in the Upper Pilarcitos Creek watershed are both spatial and temporal: topography, vegetation, and interannual variability. High-elevation sites with direct wind and ocean exposure experienced the highest frequency of fog events, and this high volume of fog throughfall decreased with lower elevation. As fog advects inland through the watershed and elevation decreases, the vegetation canopy begins to lower and its interaction with the fog ceiling is reduced. The fog also begins to evaporate as it moves inland, reducing the advective fluxes of fog water, and thus fog-vegetation interception. Our observations of substantial fog water flux at the high-elevation, ridgeline sites and negligible flux at low elevations east of the ridge reflect findings of previous studies (Fischer et al., 2009; Sawaske and Freyberg, 2015). We, however, find a reduced difference in magnitude of flux totals between these two elevations and forest conditions: A comparison of daily leaf wetness counts from a ridge site and a lower hillside site shows that the ridgeline had counts that were on average 1.1 times higher (with a 2-times

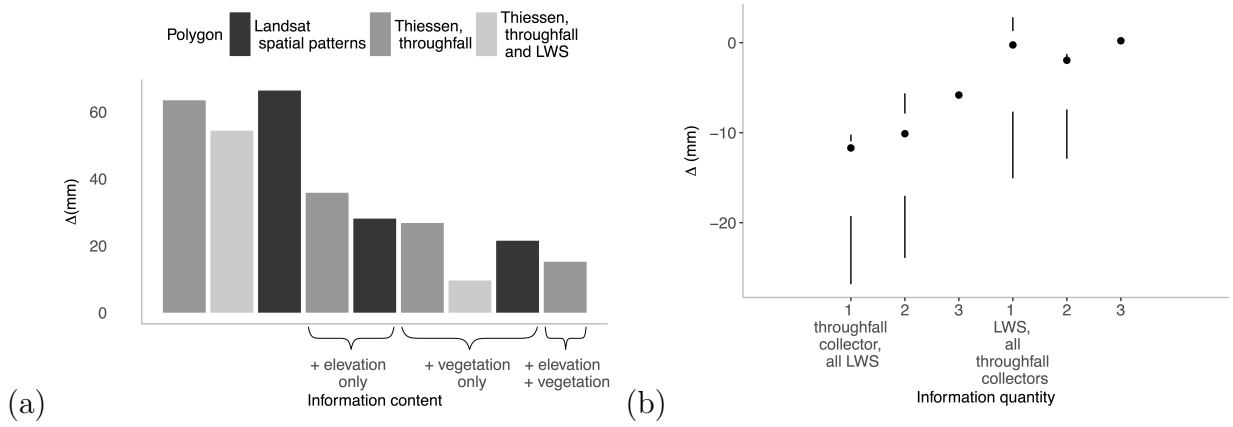

Figure 2.10: Considering the highest information content scheme as our baseline, decreasing the a) number of data types and b) data density results in an increase in deviation from the baseline.

maximum), compared to a 70-fold increase in monthly throughfall rates found by Sawaske and Freyberg (2015) in the same region. Vegetation cover and type also serve as major determinants of spatial heterogeneity. The leaf wetness sensors showed wetter conditions at the forest edge than interior, from which we infer that interaction with the vegetation canopy decreases the droplet density and advective flux. We also found that throughfall totals averaged 4-fold higher at the edge than compared to the interior of the forest, similar to a 6.6-fold increase seen by Ewing et al. (2009). Furthermore, physical differences in vegetation type across the watershed affect canopy interception of fog and subsequent fog water flux. Forest and chaparral canopies differ in height: While coyote brush scrub are generally smaller than 1.5 m, Douglas fir trees reach to 70 m, increasing frequency of fog-canopy interaction. The needle-like leaf surface of Douglas fir shoots also provides more surface area than the small, round leaves of coyote brush for fog to impact and on which droplets can accumulate.

In addition to their spatially heterogeneous nature, the frequency and intensity of fog events varied between fog seasons. For example, the intensity of advection fog fluctuated over the study years, decreasing between 2014 and 2015, and increasing in 2016. This can potentially be attributed to changes in sea surface temperature (SST) anomalies in the north Pacific Ocean basin (Johnstone and Dawson, 2010). The 2014 fog season saw above-average SSTs in the eastern basin starting and peaking in mid-July (+3 °C). In 2015, however, such anomalies began earlier in June and remained +3–3.5 °C until the end of August (NOAA Office of Satellite and Product Operations, 2015). Because above-average SST anomalies decrease the ocean-land pressure gradient that drives the coast-to-inland advection of fog, an increase in anomalies in 2015, especially during the month of August when historically, fog events reach maximum frequency, may have resulted in decreased intensity of fog events for the season. SST anomalies were minimal in the summer of 2016 (NOAA Office of Satellite and

Product Operations, 2015), potentially facilitating the advection of fog into the watershed.

The new upscaling scheme allows us to incorporate these spatiotemporal controls on point-scale observations to further our understanding of how fog events affect the watershed hydrologic cycle. The Upper Pilarcitos Creek Watershed receives 1000 mm/year of rainfall. In this basin, the direct water additions from fog, 10-30 mm/year, are relatively minor but comparable to other studies (Ewing et al., 2009; Sawaske and Freyberg, 2015). The addition of a water flux from canopy interception of fog results in wetting of the shallow subsurface, with greater average volumetric water content of soil from the surface to 300 mm below following periods of persistent fog. Low correlation between soil moisture upticks and throughfall, however, is likely due to soil moisture's response to throughfall from above-average fog events early in the dry season. After August, the deeper soil likely experiences a dry-down, in which soil below the sensor becomes dried out such that the soil is unaffected by additional moisture. As this soil stops responding to throughfall pulses, even lower correlation coefficients between soil moisture upticks and throughfall are observed. While fog water was enriched with heavier isotopes than rain, as fog represents early-stage condensate that is not subject to the 'rain-out' effect, or depletion throughout a precipitation event (Dawson, 1998), similar isotopic compositions of stem, shallow soil, and stream water suggest that mixing and damping of fog signature has occurred, possibly due to small fog volumes and a larger soil moisture reservoir. Furthermore, the isotopic results confirm that soil water pools are simultaneously contributing to vegetation uptake and streamflow, while the difference in signature between fog and streamflow suggests an absence of direct fog water isotopic input in the watershed's surface waters. These results relate to the challenges in fog water tracing through isotope signatures, as streamflow isotopes are temporally invariant and mixing can average out the signal of individual fog events (Brooks et al., 2010; Kennedy et al., 1986; Oshun et al., 2016).

Avoided transpiration, from reduced vapor pressure deficits during fog events resulting in decreased transpiration demand from vegetation, however, is more significant, along the lines of 125 mm/year. Decreased fog interception and deposition in chaparral likely results in a smaller change in transpiration demand when compared to Douglas fir trees, whose canopy is able to capture more moisture from fog due to canopy height and shape. The high PET rates under forest canopy on clear days, which can comprise nearly half of the dry season, signal a potential offset of water savings accrued during preceding fog events. Yet, we must note that these additional inputs and reduced losses occur during the dry season, alleviating the watershed water deficit during this time from 570 mm to 430 mm, a 25% decrease. This is comparable to previous findings that show that fog can comprise 13–45% of annual transpiration in a heavily fog-inundated coastal forest (Dawson, 1998). These contributions to the dry-season water balance can relieve the watershed's low flow conditions that serve as a major stressor for anthropogenic and natural processes and are thus non-trivial.

Estimation and evaluation of such watershed-scale effects of fog are dependent on the upscaling scheme, and specifically, the data sources and interpolation methods used. Commonly-used spatial interpolations to estimate a watershed-averaged flux, including Thiessen polygons and inverse distance weighting, are limited by heavy dependence on the location and

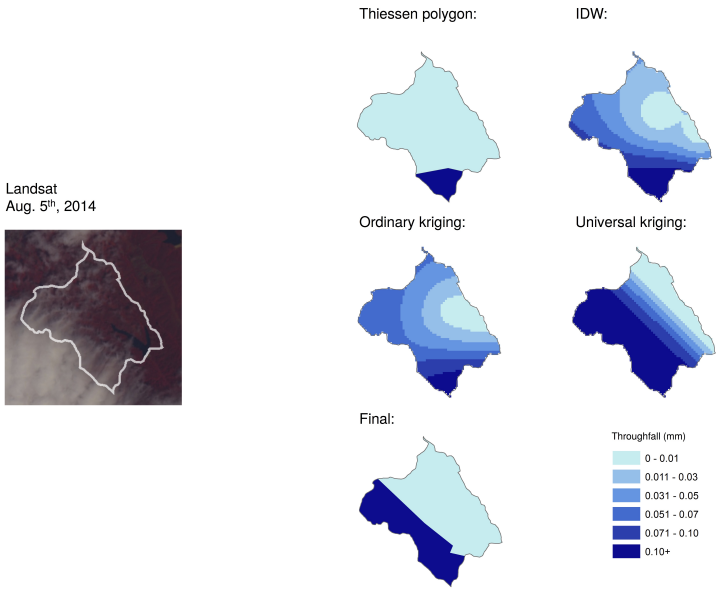

Figure 2.11: The final upscaling scheme captures spatial heterogeneities and reflects actual fog patterns observed in the watershed via Landsat 8 (cf. standard spatial interpolation methods).

density of sampling points, while kriging methods cannot incorporate the wide array of watershed features that may be spatially correlated to throughfall, producing inaccurate isohyetal fog patterns. The presented scheme, however, reflects the spatial patterns of a watershed's fog events observed by remote sensing and incorporates a suite of sensors that is able to capture the spatial range of vegetation cover and topography to predict the watershed-scale fog water flux (Figure 2.11).

In our upscaling scheme, both watershed vegetation and elevation influence fog water flux, consistent with models of deposition over heterogeneous terrain (Weathers et al., 2006). Vegetation effects, however, are more pronounced than the topographic effects, with greater sensitivity of fog water flux estimates to vegetation than elevation information. As observed by Weathers et al. (2006), though high elevation sites have large potential for high throughfall volumes due to frequent fog occurrence, this potential is captured and high volumes are observed where coniferous forest canopy, with large leaf surface area, occurs at high elevations. Therefore, the throughfall collectors and watershed vegetation map, which characterize the difference in throughfall under heterogeneous canopies in the basin, have higher information value than the leaf wetness sensors and DEM, which quantify the varying moisture conditions along a topographic gradient. We note that we have assumed collinearity between distance from forest edge and elevation in the Upper Pilarcitos Creek watershed, and this

may result in an over-estimation of watershed-scale flux by not including possible non-linear forest edge effects along an elevation band. Reducing the number of throughfall collectors in the scheme decreases the watershed area for which there is information, forcing two assumptions: 1) Larger portions of the watershed are experiencing zero effects from fog or 2) the spatial effects of fog are more uniform than in reality. This first assumption results in an underestimate of watershed-scale estimates, while the second assumption can also produce an underestimate if the included throughfall collectors are placed in an area that experiences minimal fog effects. On the other hand, reducing the number of leaf wetness sensors in this placement, along a topographic gradient, does not affect the inference of spatial coverage of the watershed under the influence fog. It does worsen, however, the accuracy of the elevation gradient by obscuring identification of elevation-dependent spatial patterns of fog events and deposition. Lastly, failing to condition the interpolation polygons on observed spatial patterns of fog (i.e. by including Landsat data) leads to higher estimates because often, areas that are rarely fog-covered and thus a larger percentage of the watershed, are assumed to experience fog.

When estimating a watershed-scale fog water flux, sensor instrumentation governs appropriate spatial interpolation. The watershed's dominant vegetation types should first be identified, and differences in fog interception and deposition under the different vegetation canopies should be closely monitored and compared through installation of multiple throughfall collectors. The throughfall collectors should be deployed strategically to span the non-random spatial patterns of fog, which can be inferred from remote sensing imagery prior to field work and data collection. Assuming that the location and density of throughfall collectors cover the full spatial extent of fog events, deployment of leaf wetness sensors along a topographic gradient can be useful in understanding elevation effects. Leaf wetness sensors could be installed along a topographic gradient to further elucidate the spatial patterns of fog; at least three leaf wetness sensors should be deployed along the gradient, as the elevation effects on throughfall may be non-linear in some cases. Additional monitoring across different topographic gradients is desirable, but may be practically limited by access and safety considerations. Furthermore, in this study, there was only one site where leaf wetness sensors and throughfall collectors were co-located. Due to throughfall's high spatial variability, more extensive calibration of throughfall-leaf wetness relationships across multiple sites, canopy conditions, and vegetation types could allow a wider use of relatively inexpensive leaf wetness sensors as a proxy for throughfall inputs. In coastal watersheds similar to the Upper Pilarcitos Creek Watershed, where elevation and vegetation are independent, both vegetation and elevation data are required for upscaling. Deployment of sensors in multiple co-located sites can capture variability under similar fog exposure and canopy and reduce the uncertainty in regression for improved scaling of throughfall. In watersheds where vegetation and elevation are correlated, both sets of data may not be required. The polygons within the interpolation scheme should be created from a combination of remotely-sensed fog patterns and distance-based methods to accurately identify and delineate watershed areas that experience fog. For larger-scale applications, we suggest employing automated image processing of time-lapse imagery for fog detection due to the labor-intensive nature of data processing.

This combination of sensors, time-lapse imagery, and remote sensing allows observation of heterogeneities in fog events and deposition to be upscaled to a spatially-averaged flux to evaluate fog's effects on the watershed hydrologic balance.

2.5 Conclusion

Watersheds with frequent occurrence of fog events experience water stress relief during the dry summer months, but fog's quantitative effects on the water balance of a basin are less well-known. To better understand fog's hydrologic role during the dry season, the dominant controls on spatial and temporal heterogeneity of fog events must be identified. This study presents a novel stratified sampling plan using a suite of sensors, time-lapse imagery, and remote sensing data, as well as an upscaling scheme that combines these datasets to estimate watershed-scale fog water fluxes and evapotranspiration suppression. The upscaling scheme allows evaluation of the mechanisms through which fog contributes to the overall water budget: We find that while fog interacts with the water balance directly via a fog water flux and climatically through reduced evapotranspiration suppression in the Upper Pilarcitos Creek Watershed, the avoided transpiration provides a more significant relief of summer watershed water deficit. Fog is therefore critical in regions such as northern coastal California, where precipitation and transpiration are out of phase and high terrestrial and aquatic ecosystem demand for water coincides with the dry season.

Part II

Characterizing surface water thermal variations

Chapter 3

Obtaining the thermal structure of water bodies from the air

3.1 Introduction

The thermal structure and regime of aquatic ecosystems are primary physical determinants of habitat quality (Alabaster and Lloyd, 2013; Caissie, 2006) and important physical forces driving macroscopic dynamics (e.g., stability and overturning of the water column, which affects biogeochemistry, oxygen demand and, ultimately, ecology (Bowler et al., 2012; Jankowski et al., 2006; Mooji et al., 2005; Vannote and Sweeney, 1980; Ward and Stanford, 1992; Wilby et al., 2010)). While the bulk thermal properties of surface water bodies are often well represented by a vertically-resolved suite of measurements that captures the existence and migration of a thermocline, such measurements implicitly assume well-mixed conditions in the longitudinal and lateral directions. Increasingly, however, thermal heterogeneities in surface water bodies are recognized as drivers of mixing and providing critical habitat. For instance, lateral temperature variations in two alpine rivers in floodplain environments in Italy were shown to be as large as the diurnal variation at any given point (Tonolla et al., 2010). Thermal gradients can drive mixing at stream confluences (Lewis and Rhoads, 2015a), and where water temperatures in tributaries are significantly lower than in main channels, such confluences can represent important thermal refugia (Rice et al., 2008). Bank-side shading, deep pools, and groundwater inputs (Ebersole et al., 2003) also create persistent thermal structure and cold-water refuges that are critical for fish habitat, particularly in streams impacted by anthropogenic changes, warm water inputs, or climate warming (Holtby, 1988; Ruesch et al., 2012; Torgersen et al., 1999a). In small lakes, lateral temperature gradients can be established by differential heating or cooling. Differential heating occurs when there are contrasts in lake depth, bottom sediments, shading, or exposure to winds (Romero and Kling, 2002; Wüest and Lorke, 2003). These gradients may be sufficient to establish convective currents within the lake or to contribute to changes in mixing layer deepening and subsequent over-turning dynamics (Horsch and Stefan, 1988; Michael and John, 1994; Old-

ham and Sturman, 2001; Romero and Kling, 2002). In large lakes, temperature differences may reflect changes in inflows, meso-scale climatic variations, and upwelling (Rinke et al., 2009). It is clear that, across a wide range of surface water bodies, significant thermal gradients may arise both vertically and in the horizontal plane, with important implications for the physical mixing processes in the water bodies, as well as the water quality and habitat values that result. Empirically characterizing this heterogeneity in the thermal structure is non-trivial. At present, researchers have four broad options for measuring the spatio-temporal thermal structure of water bodies: manual sampling, in situ sensors, remote and mobile sensing.

Manual observations of temperature structure are spatially and temporally discrete. They require the presence of a researcher and, frequently, the use of a vehicle to transport the researcher to the measurement location or wading in shallow water. While the major challenges associated with manual sampling relate to workload, there is also the potential for the presence of a vehicle or researcher to disrupt the in situ thermal structure. This is particularly true in small water bodies or if dense observation grids are required in a limited time frame.

A wide range of continuously-reporting, in situ sensors is available and requires minimal maintenance and ingress to the water body (Moore et al., 2005), which makes them particularly suitable for long-term deployments. The major limitation associated with in situ measurements lies in capturing 3D spatial structure: Doing so requires a dense grid of sensors, which can rapidly become costly, challenging to deploy and can disrupt recreational or commercial uses of the water body. Developments in thermal sensing using fiber optics provide greater spatial continuity in the measurements made. In these measurements, the exponential dependence of the scattering of light on fiber temperature allows travel times for light within a fiber optic cable to be used as a proxy for temperature, and local variations in temperature can then be inferred along the cable length (Selker et al., 2006). However, this technique requires managing long cables, which, while well suited to longitudinal sampling along stream corridors, are poorly suited to the development of a 3D gridded observational array. In addition, cost remains a constraint for fiber optic cable-based temperature measurement.

Remotely sensing water temperatures through thermal infrared imaging is an appealing technique to capture the lateral structure of surface temperatures. Surface temperatures can be observed using manned helicopters (Torgerson et al., 2001), fixed-wing aircraft (Handcock et al., 2006), or autonomous aerial vehicles (Jensen et al., 2012) equipped with thermal cameras, and on much larger scales through satellite measurements. Temperatures are typically inferred from the relationship between the intensity of the emitted radiation of a water body, with radiant temperature corrected for emissivity to yield kinetic temperatures. The resulting datasets are robust, agreeing with in situ measurements within 0.5–1°C (Kay et al., 2005; Schmugge et al., 2002; Torgerson et al., 2001). Their obvious limitation, however, is that only surface observations can be made.

An attractive approach that combines rapid spatial coverage of remote sensing with the ability to probe multiple depths in the water column (cf. in situ or manual measurements) is to use mobile sensors that are moved to multiple measurement locations by autonomous

vehicles. Autonomous surface vehicles (ASVs, i.e. "robot boats") and autonomous underwater vehicles (AUVs, i.e. "robot submarines") have growing applications in thermal mapping (Dunbabin et al., 2009; Laval et al., 2000; Marouchos et al., 2015; Zhang et al., 2014, 2012). These systems are mobile, do not need a human operator and can be deployed for long periods of time, allowing researchers to generate high spatiotemporal resolution maps of the full 3D thermal structure of the water. The major challenges associated with these systems are that they can be difficult to deploy (for example, many require a boat ramp or dock to launch the vehicle), are costly and have limited obstacle avoidance capabilities that prevent operation in shallow areas near shore or where there is significant underwater vegetation. AUVs are further limited by the lack of GPS and radio communication underwater, which makes obtaining geo-referenced readings challenging and costly. Because of these limitations, ASVs and AUVs are typically only deployed in large bodies of water.

This chapter proposes and evaluates an alternative automated temperature sensing system based on the use of an unmanned aerial system (UAS) to quickly obtain 3D thermal maps of water bodies by lowering a temperature probe into the water at controlled depths. UASs offer several advantages for thermal sensing in surface water bodies: They do not require shoreline access, can be quickly and easily deployed and redeployed, facilitating repeated sampling, and can rapidly move between measurement locations. In addition, unlike thermal infrared sensors, the UAS can resolve the full 3D thermal structure of the water. The proposed UAS is limited in the depths of the water column that can be feasibly sampled, making them most suitable for deployment in shallow water bodies. UASs are also subject to well-known and previously-reported limitations, related to vehicle restrictions, such as flight times and payloads, as well as regulatory constraints (Dunbabin and Marques, 2012; Hardin and Jensen, 2011).

Here, we introduce the aerial sensor platform and the adjustments made to enable temperature measurements throughout a water column at multiple points. We explore preliminary results from initial field experiments, which were designed to directly compare the temperature measurements made from the UAS platform with measurements recorded by an in situ array while also considering the possibility of UAS platform-induced disturbances in the vertical thermal structure of the water column. We also identify key needs for improving future applications and explore the potential scalability of future UAS water sampling platforms for 3D mapping of temperature structure.

3.2 Materials and methods

Site description

Temperature sensing experiments were undertaken at Big Lake in Blue Oak Ranch Reserve (BORR), a 13 km^2 undeveloped ecological reserve managed as part of the University of California's Natural Reserve System. BORR is a locus for the development of ecological sensing technologies and was considered an ideal site to test the UAS platform due to its

remote location and multiple surface water habitats. Big Lake is the largest of the perennial ponds at BORR. It has a surface area of 0.0125 km^2 and a maximum depth of nearly 9 m.

Two vertical arrays of temperature sensors (6.5 m apart) were installed 10 m from the shoreline in 1.3 m water on the western boundary of the lake. Five HOBO Pendant temperature loggers were attached to the vertical array at depths of 0.25, 0.41, 0.56, 0.79 and 1.17 m. See Table 3.1 for sensor details.

Sensor	Specifications
In situ temperature	HOBO Pendant Temperature/Light Data Logger Resolution: 0.14 °C at 25 °C Accuracy: ±0.53 °C Operating range: -20–50 °C
UAS pressure-temperature	Measurement Specialties MS5803-01BA sensor Pressure resolution: 0.012 mbar Pressure accuracy: ±2.5 mbar Temperature resolution: 0.01 °C Water contact detector

Table 3.1: Sensor specifications for the in situ temperature sensor and UAS pressure-temperature sensor system.

Vehicle and sensors

Figure 3.1 shows the UAS system in flight at BORR. The UAS platform used in these experiments was an Ascending Technologies FireFly Achtelik et al. (2012) Hexrotor with a 600 g payload and a flight time of approximately 20 min. The FireFly is equipped with a variety of sensors to measure position: a GPS, an inertial measurement unit, and a pressure altimeter. The vehicle is controlled by input from two 802.15.4 XBee 2.4 GHz radios: One radio channel provides input from a remote control station on a laptop (allowing, for example, a pre-programmed flight path to be sent to the UAS) and another for manual control by a human pilot.

To facilitate the use of the UAS for freshwater ecology, we augmented the base platform with several sensors and subsystems (Ore et al., 2015). Most importantly, we added multiple downward-facing ultrasonic rangers (Maxbotix MB1240-EZ4: ±1-cm accuracy within 2 m) to improve altitude estimation over water and thus provide better flight elevation control. To enable sensing within the water column, we attached a custom-built pressure-temperature embedded sensor system to a 4 m tube, which terminates in a pump, allowing water samples to also be taken with the same system. A basic conductivity sensor is also attached to the end of the tube, allowing a direct indication of whether it is submerged or in air. This is

Figure 3.1: UAS in flight at Big Lake, Blue Oak Ranch Reserve, California, UAS.

primarily a safety feature to protect the pump and to ensure that it is submerged before pumping. An image of the system is shown in Figure 3.2, and the sensor specifications are provided in Table 3.1. During flight, the tube is reeled into the UAS, using a thin thread that runs through clips. The clips are attached to the tube at 0.75 m intervals, and the tube is retracted by spooling the thread beneath the UAS, causing the tube to coil below the vehicle. A long length of tube can become entangled in the environment and its swinging motion during flight can induce dangerous and unstable flight dynamics. Therefore, the spooling mechanism reduces the hazards associated with flying with an object attached to the UAS.

To make measurements, the UAS hovers above the water surface and the tube is extended through the water column. Varying water depths can be sampled either by changing the length of the tube that is extended into the water column or by changing the UAS altitude with a fixed length of tube extended. For each flight, the data from the UAS's pressure-temperature system are transmitted from the UAS to a laptop ground station, where it is time stamped and written to a data log along with the UAS's GPS coordinates and altitude.

Flights for temperature sampling

To compare temperature measurements from the UAS and in situ sensors, we made four flights. The fully-unspooled tube and thermal sensor were lowered through the water column near ($\sim$0.5 m radius) one in situ thermal array, while maintaining a maximal distance from the other array. Temperatures were recorded at 4 Hz for 30 s at each of the five points through the water column, at 0.2 m intervals from 0.2 m deep from the bed of the lake.

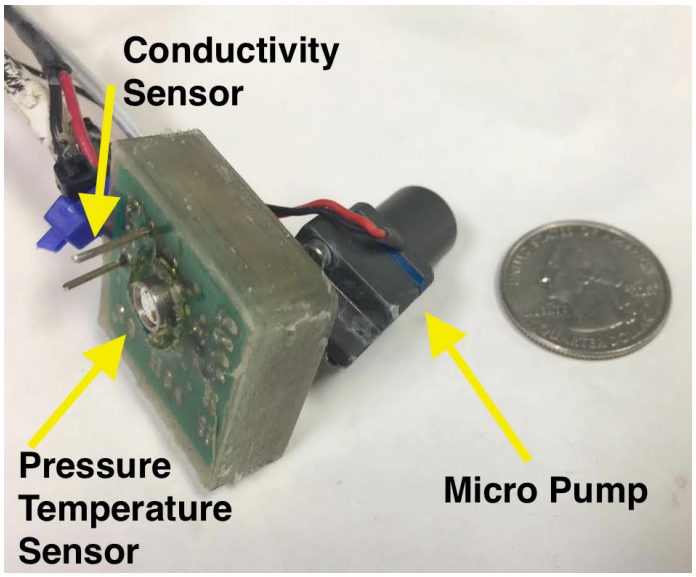

Figure 3.2: Detail of the pressure-temperature embedded sensor system contained at the end of the UAS tube. A U.S. quarter piece is shown for scale.

We waited 30 min between flights to allow the array to re-equilibrate to the background value. We selected 30 min because we previously confirmed that this duration was sufficient to achieve equilibrium following a disturbance. Flights were made in the late afternoon of March 20, 2015, with an average air temperature of 18 °C and a wind speed of 2.1 m/s. A comparison of these conditions with in situ temperature logging made during the preceding days indicated that the water column experienced mild diurnal temperature variances, with no evidence of over-turning or significant change in the surface mixed layer depth. Due to these stable, stratified conditions, we did not expect to observe exaggerated temperature dynamics in the lake during the experiments.

Data from the in situ array and the UAS were post-processed as described in the following section and compared for each flight.

To explore the feasibility of larger scale mapping with the UAS, we made two flights, using the spooling mechanism, to measure vertical profiles at three points along two parallel lines, as shown in Figure 3.3. The two parallel lines are separated by 10 m, with points in each line spaced 5 m apart. We flew ∼4 min at each location, starting at a higher altitude to submerge the pressure-temperature sensor to a shallow depth of ∼0.5 m, then descending by 0.5 m increments every 30 s. After eventually submerging and holding the sensor at a maximum depth of ∼2.5 m at each location, we ascended high enough to completely clear the water, then flew to the next location.

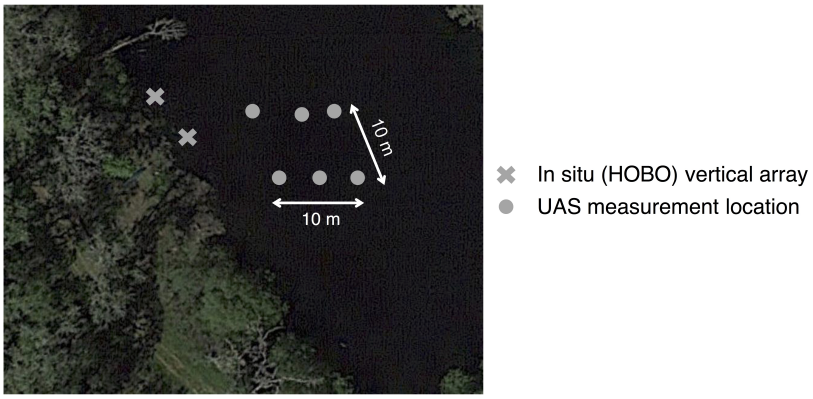

Figure 3.3: Map of locations of vertical profile measurements made by the UAS at Big Lake.

Post-processing

Post-processing involved two steps: filtering UAS temperature data and calibrating the UAS and in situ sensors to a common temperature datum.

Filtering

We filtered the temperature data because unintentional altitude changes in the UAS during flight result in the temperature sensor moving periodically up and down 25 cm through the water column. This movement causes multiple temperature readings to be associated with a given target depth and is problematic because the thermal response time of the MS5803 sensor is long compared to the rate of vertical movements. On average, the sensor requires 90 ± 45 s to converge to 90% of the actual temperature (the temperature response time of the sensor system is slowed due to polyurethane waterproofing that protects the electronics). To avoid erroneous data associated with these long equilibration times, we filtered the temperature data based on the joint rates of the change of pressure sensor depth and temperature. Specifically, we excluded temperature readings when either temperature or depth changes quickly: $\frac{\partial T}{\partial t} \geq 0.04\,^{\circ}\mathrm{C}s^{-1}$ or $\frac{\partial m}{\partial t} \geq 0.35\mathrm{ms}^{-1}$. These thresholds were determined by visually inspecting plots of the temperature and depth rates of change and observing that during periods of minimal change, nearly all values are bounded by the aforementioned thresholds. As shown in Figure 3.4, this filtering method retained 15% of the original readings and discarded most readings from the descent periods between the five measurement points in the water column.

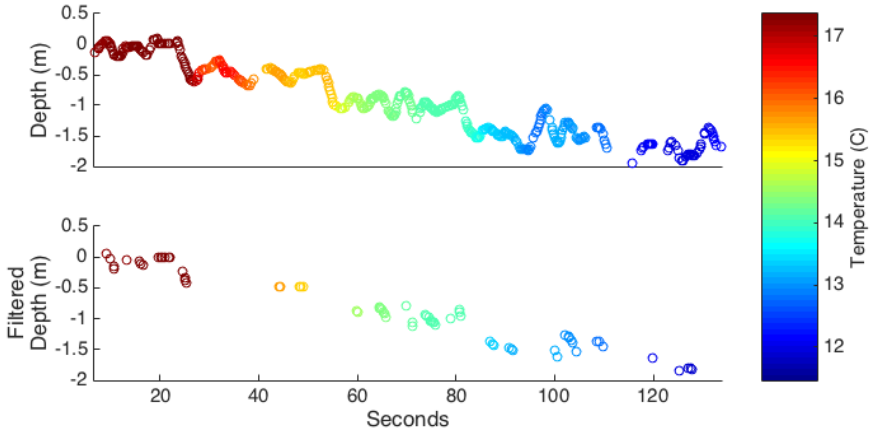

Figure 3.4: The filtering method removes data when temperature and depth change rapidly.

Calibration

Prior to comparing UAS and in situ temperature readings, we calibrated the sensors against each other in the laboratory using room temperature water (21.8 °C) and ice water (0.1 °C). The MS5803 (UAS) sensor reported higher temperatures than the HOBO (in situ) sensor, except during periods of rapid temperature change, when the two sensors reported comparable values. We assumed that temperature changes imposed during calibration would be large compared to temperature changes measured in the field and therefore adjusted the UAS temperature data to improve correspondence with the in situ sensor readings obtained during calibration. The UAS temperatures were offset by -0.3 °C.

3.3 Results and discussion

Comparison of UAS and in situ temperature measurements

Over the four test flights, the UAS sensors reproduced the temperature variations in space associated with the water column's thermal gradient and the mean variations in time during the two-hour experimental window. However, the temperatures measured from the UAS were consistently higher than the in situ array-recorded temperatures, even following calibration. The magnitude of the temperature bias varied with depth in the water column and was highest in deeper areas of the water column. Figure 3.5 shows box plots of the bias associated with each temperature measurement made by the UAS over the four flights, binned by depth in the water column. The bias is on the order of 0.5 °C in the surface 0.5 m of the water column and increases to 2 °C at greater depths below the thermocline.

While it is encouraging that these deviations in temperature are comparable to those made by other methods (e.g., TIR (Torgerson et al., 2001); fiber optics (Selker et al., 2006; Tyler et al., 2009)), the deviations are much greater than previously seen in mobile sensing

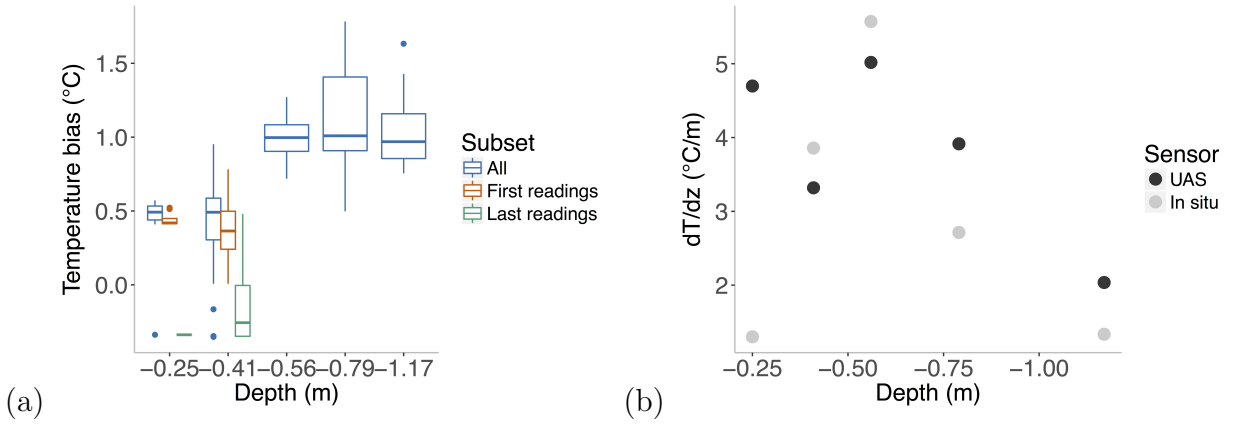

Figure 3.5: Comparison of UAS-borne and in-situ temperature sensors, including logged data and detected thermal gradient: a) box plot of bias in temperature measured at each depth and b) comparison of derived temperature gradient at each depth.

systems (Laval et al., 2000). Furthermore, the depth dependence in the magnitude of the bias suggests that a physical mechanism may be responsible. We hypothesized that several mechanisms could explain the bias: thermal lag effects when the sensor was first introduced into the water column from the air or entrainment of cold water from a depth to surface layers as the sensor was raised from the lake bed to the surface. As a preliminary means to distinguish between these hypotheses, we explored whether the magnitude of the thermal bias at the surface varied between the first shallow readings and the final readings made during a flight.

As seen in Figure 3.5, the UAS sensor temperatures remain higher than the in situ sensor temperatures near the surface, but the bias is decreased in the first readings during a flight. The direction of the bias switches for the final shallow readings during a flight, with temperatures measured from the UAS being lower than the in situ array-recorded temperatures. We suggest that these observations are more consistent with the entrainment of cold water as the tube and sensor were moved up through the water column at the end of a flight, than with the effect of thermal lags. Thermal lags in the on-board UAS sensor would be expected to have led to large positive biases in temperature upon initial entry into the water column. Despite the temperature bias between the UAV and in situ sensors, the UAV sensor's temperature resolution of 0.01 °C is sufficient for capturing fine-scale thermal heterogeneities in the water column.

To remove systematic bias from the temperature sensors during the field trials and to consider only relative variations in temperature, we also compared estimates of the local thermal gradient in the water column as made from each of the sensing platforms, presenting the results in Figure 3.5. Below the water surface, both platforms produced comparable trends in the thermal gradient, again within 0.5–1 °Cm^{-1} of each other. Both the peak in

the thermal gradient associated with the thermocline, at a depth of approximately 0.6 m, and increased thermal stability with depth were identified by both sensor platforms. Significant disagreement between the measurements was only observed in the top 0.25 m of the water column, when the UAS measurements indicate a peak in thermal gradient comparable to that at the thermocline, while the in situ sensors indicate a fairly consistent temperature change with depth. The source of this high temperature gradient as sensed by the UAS is not completely resolved, but may be associated with a lack of elevation stability, causing the sensor to be suddenly pulled out of the water when at the surface and to undergo a rapid temperature change.

What water column disturbance is induced by the UAS?

We hypothesized that water column disturbance induced by the UAS due to propeller wash and the motion of the tube would result in greater mixing and, thus, higher variance in temperatures measured below the UAS compared to a control. First, we confirmed that temperature variance measured at a given depth did not depend on the time window over which variance was calculated. We then computed temperature variances over 30 s periods for all depths and compared the profiles of the temperature variance at the test and control temperature arrays with a paired t-test. We did not find a significant difference in the temperature variances at any depth ($p>0.05$), except for the shallowest in situ sensor depth: $t=-2.53$, $p=0.01$. This suggests that any disturbance caused by the UAS in the water column is comparable in magnitude to natural sources of perturbation in the water profile. However, increased temperature variance at the surface of the water column provides evidence of UAS-induced disturbances due to propeller wash or mixing from the sensor occasionally being pulled out of the water.

Feasibility of mapping 3D temperature structure

Figure 3.6 illustrates the interpolated temperature structure in a 10 × 10 × 2.5 m region of Big Lake. The UAS sensors allowed multiple sites and depths to be measured on a fine grid. The platform also resolved the thermal structure of Big Lake, including vertical trends and the more subtle lateral trends, specifically a general decrease in temperature away from shore. Obtaining these 30 data points required 26.5 min of flight time during two UAS flights, plus time for setup and deployment.

While still faster than some manual techniques, rapid development of comprehensive spatial maps over large areas with short time frames will require further advances. The obvious technical limitations include battery life, which, coupled with the relatively slow response time of the thermal sensors used, limited the number of locations that could be sampled per flight. Thermal sensors better suited to this application are available, and future deployments will focus on a thermocouple with response times of 5 s or less (Garnier and Lanzetta, 2011). Using such a sensor, the UAS could measure temperatures every 0.5 m at depths from 0–4 m at twenty different sampling locations within the 18 min battery life. At

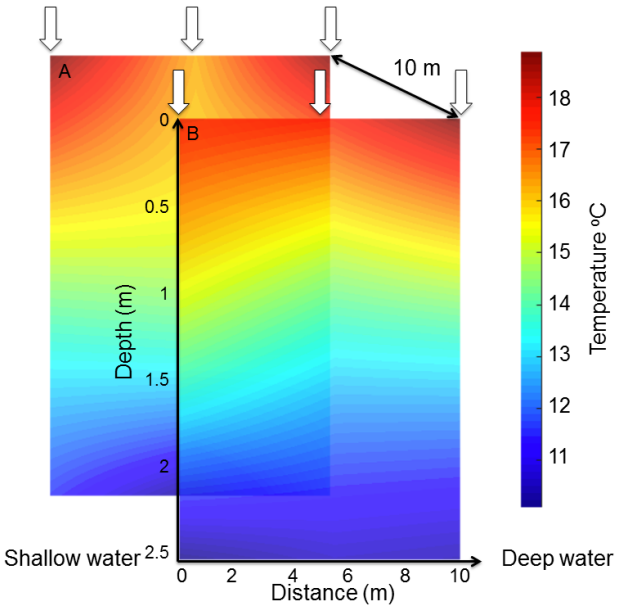

Figure 3.6: Thermal structure of a 10 × 10 × 2.5 m grid, interpolated and reconstructed using temperature data from two UAS flights. White arrows indicate the UAS's sampling locations; depth measurements were made throughout the water column at these sites.

this rate, approximately five flights would be needed to measure Big Lake on a 10 × 10 m grid. This would be achievable in under 2 h, and repeat flights would be sufficient to allow diurnal cycling to be resolved.

Use of the UAS platform, as with other mobile sensing methods, presents a tradeoff between the detailed information from the high spatial resolution of temperature measurements and the limitations of a discontinuous time frame in which measurements are taken. While in situ sensors provide a temporally-continuous record of temperature at a location, the UAS captures a snapshot of the thermal structure in time. To account for general trends in temperature changes over time and a large area, sampling on a less dense grid may be necessary to avoid spatial biases, because the time frame of measurement is significantly longer than the time frame of temperature adjustment. For high resolution sampling with a single UAS, a nested sampling grid approach may be appropriate: The UAS could be flown to points on a less dense grid to record an initial thermal structure, then flown to points on subsections of a denser grid during shorter, constrained flight times to avoid any significant warming or cooling during the flight. Data from the a small set of in situ temperature loggers could then be incorporated to detrend warming during the flight time period; in practice, we expect to use both in situ and UAS sensors.

The quality of the resulting data and the ease of deployment would be enhanced by improved sensor calibration and improvements in stabilizing the UAS with respect to drift and altitude variation. Because this was an initial evaluation of the UAS platform's temperature

probing capabilities, the sample size used in the experiment is not very large. To further assess the accuracy of this methodology, a new on-board thermocouple with a faster response time is required to compare its measurements with in situ sensors and to calibrate accordingly. Additionally, the latest commercially-available UASs are characterized by improved stability and altitude control, which would address these issues, and we expect that UAS and battery technology will continue to improve.

Operational modes

The temperature readings were made using two different modes of flight: 1) flying down to within 1.2 m of the water surface, then unspooling the tube while hovering; and 2) flying with a completely unspooled tube and approaching the water from a higher altitude. We found no clear differences in the disturbances induced in the in situ lake temperatures between the flight modes, but made some operational observations. Specifically, flying with an unspooled tube enabled the UAS to remain high above the water surface. This offered a safer flight mode by increasing the buffer distance between the vehicle and lake and reducing the visual disturbance of the lake surface. However, altitude variation was more pronounced in this flight mode (typically above 1.8 m). At these altitudes, the UAS relies on a barometric altitude sensor that drifts due to wind and the continual natural variation in ambient air pressure. We often observed changes of ± 0.2 m within less than a minute. However, when flying closer to the water surface (within 1.8 m), the UAS uses short distance ultrasonic rangefinders that enable steadier flight. In practice, we would recommend flying farther from the water to reduce operational stress on UAS pilots.

Pragmatic limitations

Technological challenges aside, researchers must navigate a volatile regulatory landscape that varies by country (Mulero-Pázmány et al., 2014; Vincent et al., 2015). Recently, some countries have proposed rules governing the use of UASs by academic researchers that are focused on limiting payload, altitude, visual range and proximity to densely-populated areas (Whitehead and Hugenholtz, 2014). Researchers seeking official sanction should allow ample time to address local regulations or risk derailing a project's timeline for data collection. Clearer and simpler regulations for environmental sensing with UASs in low-risk, low-altitude, and low-population areas would increase their practicality and usefulness.

3.4 Conclusion

This chapter outlines a novel method using a UAS to characterize the thermal structure in shallow bodies of water. The preliminary experiments illustrate that physically lowering a sensor from air with a UAS can obtain reliable and robust measurements of ambient water temperature, with reasonable agreement with in situ measurements and without significantly

disturbing the water column. The results suggest that operationally, the best results are obtained when a sensor is lowered into the water column from an unspooled tube. Furthermore, the most reliable measurements are made when the elevation change of the sensor is slow and the sensor is descending. Future research should focus on improving the UAS elevation stability and minimizing drift, along with incorporating faster temperature sensors to capture the thermal structure with high resolution even when moving quickly through the water. With improved temperature sensors, as many as twenty 4 m surface water profiles could be obtained in a single 18 min flight. This would be fast enough to allow multiple flights to capture key diurnal variations and sufficient to allow complete characterization of small water bodies (circa 1 ha) in less than two hours. Although the system tested here focused on a small lake, the aerial platform could be used to characterize the thermal structure and regimes in streams, rivers, wetlands, and larger lake systems.

Chapter 4

eDNA detection for amphibian disease

4.1 Introduction

Amphibians are undergoing a global extinction event that threatens one-third of all species worldwide (International Union for Conservation of Nature and Natural Resources, 2015), and all of California's 76 native frogs and salamanders. Such global decline (not attributable to natural, large fluctuations in population size but rather anthropogenic changes (Hof et al., 2011)) is of concern because amphibians comprise the highest fraction of vertebrate biomass and serve as indicators of environmental health and resilience (Blaustein and Wake, 1990). In California, all native species show a decline varying geographically and taxonomically, with the most extreme case in which the northern red-legged frog (*Rana aurora*) has been lost in 24 of 28 counties of original habitat and only exists in a few isolated ponds in the state's Coast Range (Fisher and Shaffer, 1996).

In these regions, drastic alteration of natural water bodies has left vernal pools and farm ponds as critical habitat for the survival of many of these species, thus decreasing population size and increasing the degree of population isolation (Knapp et al., 2007). However, these small, isolated ponds are vulnerable to hydrologic and biogeochemical perturbations that alter the quality of habitat they provide. This vulnerability is exacerbated by both climate change, which drives changes in watershed hydrology and thermal regimes of the small ponds, and land use, or specifically, conservation grazing. The presence of cattle in watersheds alters the nutrient and water balance for the ponds (Fellers et al., 2011; Johnson and Chase, 2004) and the condition of riparian vegetation, and by extension, the whole pond ecosystem. The combined abiotic and biotic effects of climatic drivers and land use on ponds have been observed to foster conditions that are hospitable to disease-causing organisms such as *Ribeiroia ondatrae* (Rib) (Johnson and Chase, 2004; Johnson et al., 2007) and *Batrachochytrium dendrobatidis* (Bd) (Sparrow, 1968). Rib is a parasite that causes teratogenesis in tadpoles while Bd, widely known as the "chytrid fungus," causes chytridiomycosis and is considered a key agent of global amphibian extinction.

Evaluating the effects of both hydrologic variation and grazing practice on habitat qual-

ity for amphibians in California is challenging for several reasons. Ecosystems under certain environmental conditions could potentially exhibit bistability between two alternate stable states separated by an unstable equilibrium. A growing body of research highlights the ubiquity of bistability between oligotrophic and eutrophic conditions in shallow lake ecosystems under comparable nutrient forcings (Carpenter et al., 1999; Scheffer and Carpenter, 2003; Scheffer et al., 2001). This bistability, if present, would confound the simple interpretation of habitat quality as a function of water column nutrient status, specifically phosphorus concentration, and may explain the lack of relationship between nutrient status, Chlorophyll-A (ChlA) levels, and presence of disease in literature (Fellers et al., 2011), despite observations that increased phosphorus concentrations increase the density and vigor of the planorbid snail hosts for Rib (Johnson and Chase, 2004; Johnson et al., 2007) and prevalence of algae substrate for Bd fungal growth (Sparrow, 1968). Because such bistability can result in heterogeneity in pond oligotrophy and eutrophy across a watershed, high spatial and temporal frequency sampling of pond water across the landscape is required to accurately monitor the interaction between watershed hydrology, land use, and water quality. Additionally, established protocols for disease detection are host sampling and biological assays, which involve invasive testing of amphibians and planorbid snails (amphibians: (Hyatt et al., 2007); snails: (Reinitz et al., 2007)) and often results in sacrificing animals in early stages of infection when treatment may be possible.

Sampling nutrient concentrations and water temperatures from multiple ponds, and in particular repeat sampling, to evaluate habitat conditions and vulnerability is time-consuming and challenging, as these ponds are spatially distributed within a topographically complex landscape. Though small, they are dispersed throughout a large watershed and are remote, often a hike from the nearest vehicular access point. Host sampling also requires ingress into the pond, which when sampling multiple ponds across a landscape, may promote spread of disease.

This work aimed to employ innovative field techniques to address these challenges and test the following hypotheses:

1. Vernal pools and farm ponds experience bistability with respect to trophic status: i.e. ponds with similar thermal regimes and water column nutrient concentrations will display different levels of oligotrophy and eutrophy, as quantified by ChlA concentrations.

2. Rib and Bd presence increases with ChlA concentration, subject to the dynamics of the snail and zoospore hosts of these diseases.

A cursory exploration of these hypotheses was conducted using a combination of the previously-developed unmanned aerial system (UAS) water sampling platform (Chapter 3), water quality analysis, and novel environmental DNA (eDNA) techniques to facilitate both quick, repeatable sampling and non-invasive disease detection across pond sites. However, multiple trials of eDNA methods with UAS payload-constrained water samples published were unable to detect either Rib or Bd in ponds with a history of disease presence or positive

detection through host sampling, and thus it was not possible to examine the relationship between water temperature, nutrient concentration, and disease presence. Exploratory field trials show that it is more likely that eDNA sampling is not suitable for disease detection at these sites, rather than UAS use being limited in this application.

4.2 Materials and methods

Site description

This research was focused on three sites in the Mount Hamilton area of the Southern Coast Range. Located on the west-facing slope of the Diablo Range, the area supports grasslands, chaparral, and oak woodland communities, with stands of conifers appearing above 1200 m. The climate of central coastal California is Mediterranean; the range sees mild winters with moderate rainfall but dry and hot summers.

Blue Oak Ranch Reserve, a 13 km^2 undeveloped ecological reserve that encloses four watersheds, served as the control site. The streams and 17 ponds of the reserve serve as habitats for rare species such as California tiger salamander (*Ambystoma californiense*), foothill yellow-legged frog (*Rana boylii*), and red-legged frog (*Rana draytonii*). Additionally, there are at least seven species of amphibians supported by the reserve. Neighboring Kammerer Ranch Reserve, managed by the Nature Conservancy, and Joseph D. Grant County Park, managed by the County of Santa Clara and the largest of the county's regional park and recreation areas, both employ conservation grazing measures with varying cattle stocking rates. Kammerer Ranch is stocked, year-round, at no more than 50 AUM as per the state's Department of Fish and Wildlife's conservation easement that covers half of the property. At Grant Park, cattle graze from mid-November to July and is stocked at 135 AUM; in 2015, the south side of the park was stocked at 84 AUM due to dry conditions.

Field and laboratory methods

Monthly water samples, in volumes allowed by the UAS payload (60 ml), were collected between May and September 2015 from a total of ten ponds spanning the three sites (Figures 4.1 and 4.2):
Blue Oak Ranch Reserve

- Big Lake (BORR-B)
- Cabin Pond (BORR-C)
- Upper Turtle Pond (BORR-UT)

Grant Park

- Grant Lake (GP-G): Rib- and Bd-positive

- McCreery Lake (GP-M): Rib-positive
- Eagle Lake (GP-E; September only): Rib-positive
- Manzanita Pond (GP-MA; September only): Rib- and Bd-positive

Kammerer Ranch

- Wood Duck Pond (KR-WD)
- Trout Pond (KR-T)
- Mallard Pond (KR-M): Rib-positive

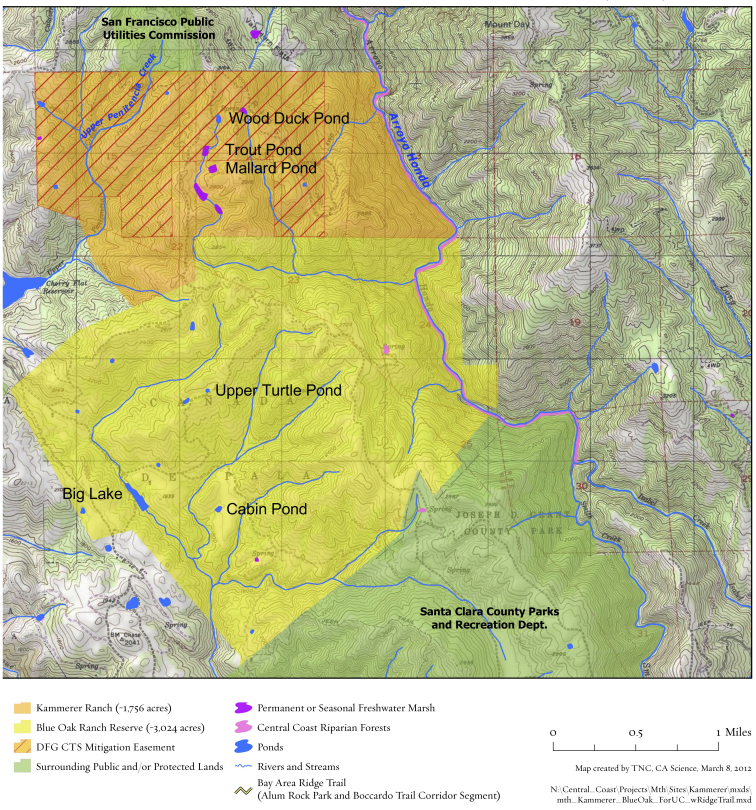

Figure 4.1: Map of ponds at Blue Oak Ranch Reserve and Kammerer Ranch, provided by the Nature Conservancy.

Water samples for nutrient and ChlA analysis were filtered through Whatman 25 mm GD/X Syringe Filters (glass microfiber, 0.45 µm). The manually-collected samples were analyzed for total nitrogen, total phosphorus, and ChlA.

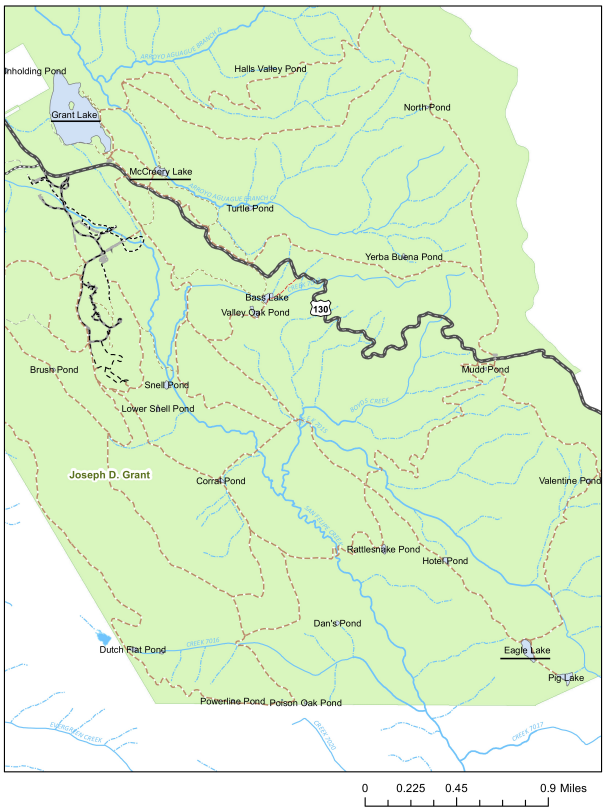

Figure 4.2: Map of ponds at Grant Park, provided by Santa Clara Parks and Recreation Department. Sampled ponds are underlined; Manzanita Pond is not shown on this map due to size.

Triplicate samples for Rib and Bd eDNA detection were collected following the USGS Amphibian Research and Monitoring field protocol (USGS, 2007). eDNA was extracted according to Chestnut et al. (2014) and Kirshtein et al. (2007), with modifications reflecting USGS quality control measures (Akob, 2015). Real-time, quantitative polymerase chain reaction (qPCR) assays using synthetic standards (Longo et al., 2013) and SYBR Green-based detection were run in triplicate according to Huver et al. (2015) (Rib) and Kirshtein et al. (2007) (Bd).

Refer to Appendix B for detailed eDNA sampling and extraction methods, and qPCR assay protocol.

4.3 Results and discussion

This study addressed the possible presence of 1) bistabilty through water quality analysis and 2) Rib and Bd through tests and trial runs of published eDNA methods, under the sampling constraints of the UAS water sampling system.

Pond nutrient status

During the dry-season, summer sampling months, ammonium and nitrate levels in the ponds were very low (<0.05 mg/L detection limit), with no difference observed between ungrazed and grazed sites. Higher nitrogen and phosphate concentrations were observed at a grazed site at Grant Park (GP-G) throughout the sampling period, possibly reflecting the higher cattle stocking rate at Grant Park vs. at Kammerer Ranch and the control sites. ChlA concentrations varied spatially across sites with land use: There was a significant difference in concentrations between control and grazed sites as shown through a t-test, with clear, oligotrophic ponds at the control site showing the lowest concentrations and ponds at the remaining grazed sites showing higher concentrations (t=-4.44, p<0.05). However, a t-test showed that there was no significant difference in concentrations between ponds at Grant Park and Kammerer Ranch (t=-0.77, p=0.45) despite their varying stocking rates. Therefore, the higher stocking rate at Grant Park vs. at Kammerer Ranch was not reflected in levels of oligotrophy and eutrophy, as indicated by ChlA concentrations.

ChlA levels also showed temporal variation, with increasing concentrations in the beginning of the summer, from May to June, then decreasing from June to July. This decrease is unexplained at most sites, though at Grant Park, it may be attributed to the decrease in stocking rate in July. At Kammerer Ranch's Wood Duck Pond (KR-WD), a significant increase in ChlA concentrations was observed between July and August, with the pond switching from oligotrophic to eutrophic conditions. However, during the same time period at neighboring ponds with the same grazing conditions, and thus similar expected nutrient inputs, concentrations did not increase.

This display of different levels of oligotrophy and eutrophy in water columns of similar nutrient regime suggests the possibility of alternate stable states in the sampled ponds. In pond ecosystems, the two alternate stable states are clear, oligotrophic water with submerged vegetation and turbid, eutrophic water. Water clarity is nonlinear and unaffected by increasing nutrient concentrations, such as phosphorus that accumulates in sediment and biota, until a critical threshold is passed, at which point the body of water shifts suddenly from a clear to turbid state; this increased turbidity is associated with disappearance of submerged plants, loss of animal diversity, and increased algal biomass (Genkai-Kato and Carpenter, 2005; Scheffer and Carpenter, 2003). When the phosphorus source from sediments remains low and is negligible compared to loss rates, one stable equilibrium point of oligotrophy or eutrophy results, and a pond will stabilize in one state due to feedbacks involving biological, physical, and chemical mechanisms. However, when recycling of phosphorus from sediments increases more rapidly than loss or sink rates from the water column

over a range of phosphorus, an unstable equilibrium and alternate stable states can occur (Carpenter, 2005). Such rapid recycling from sediments can cause eutrophic lakes to fail to respond to decreases in phosphorus input and thus maintain a eutrophic state. It is possible that at Kammerer Ranch, ponds with similar nutrient loading are experiencing highly varied levels of algal biomass due to this hysteresis.

Disease presence

qPCR was used to generate a calibration curve of synthetic DNA standards and interpolate unknown concentrations of Rib and Bd in sampled ponds.

R. ondatrae (Rib)

Huver et al. (2015)'s qPCR assay was initially tested using a synthetic DNA block of 160 base pairs (bp) in length, which amplified well under the primers (Ro-ITS 3 F/R) and cycling conditions (annealing temperature at 46 °C). With a serial dilution, a set of standards using this synthetic block was created to be used in a standard curve. The standard assay produced amplification curves as shown in Figure 4.3, which reflect the serially decreasing concentration of standards and a uniform melting point of 81 °C.

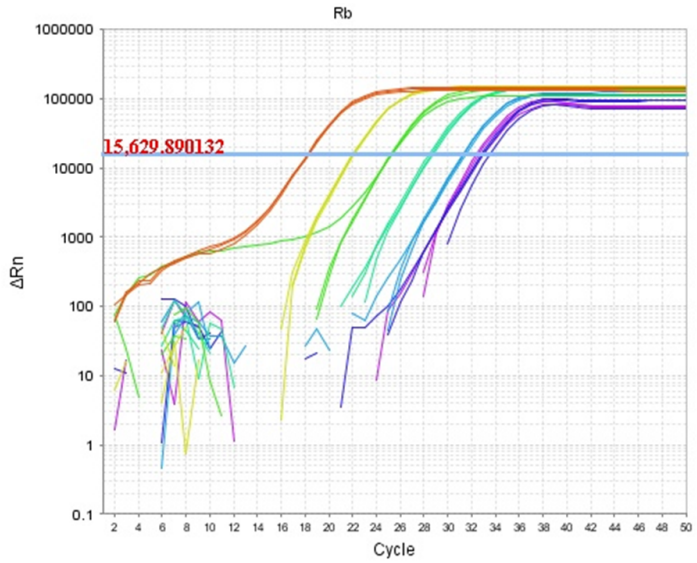

Figure 4.3: Amplification curves for Rib standards using Ro-ITS 3 F/R primer.

However, nearly all samples from May to September (including those from control sites and no-template controls) showed amplification at high levels, though the melt curves show multiple peaks and indicate more than a single amplicon (Figure 4.4). Samples from May were run out on an agarose gel using electrophoresis (Figure 4.5), in which standards showed

a single band around 160 bp, as well as some primer-dimer. None of the samples, however, showed a single amplicon at this size, as suggested by the melt curves. This seems to suggest that the ponds contain sub-populations of related Rib with polymorphisms or various organic contaminants that interfere with amplifications, or that the amplifications are from PCR artifacts due to contaminants causing various mispriming (i.e. annealing to the target, with transient melting and thus causing various lengths of products) (Whyard, 2015).

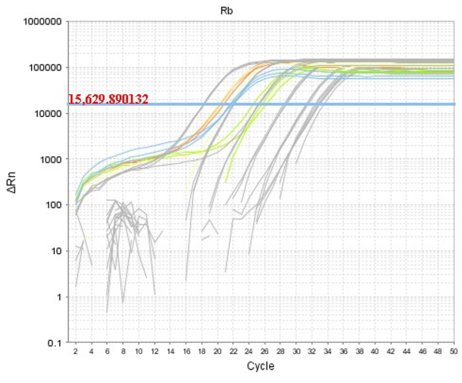

(a)

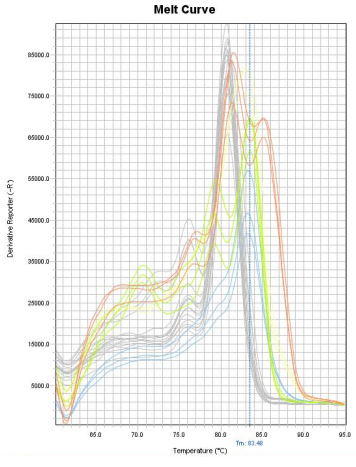

(b)

Figure 4.4: a) Amplification and b) melt curves for standards (grey) and a subset of Rib pond samples using Ro-ITS 3 F/R primer. These samples are from negative, control sites yet show amplification.

Because mispriming can often be fixed by raising the annealing temperature, a subset of May samples was run in the thermocycler with an adjusted annealing temperature of 60 °C. This produced no false positives but also produced no amplification in the lower concentration standards. Therefore, to find the optimal annealing temperature, the same subset of samples was run at five different annealing temperatures: 48, 52, 54, 57, and 60 °C. Between 48 and 54 °C, all samples showed amplification; between 54 and 60 °C, there were fewer false positives. At 57 °C, one sample from a known positive site (KR-M) had a melting curve similar to those of the lower concentration standards; when a gel was run out using electrophoresis, the sample showed multiple bands at the lower annealing temperatures, but two clear bands with one at 160 bp when run at 54 and 57 °C (Figure 4.6). This seemed to indicate that this is the range of optimal annealing temperature for these primers.

To further narrow down the range of the optimal annealing temperature, the same subset of samples was run in the thermocycler at six different annealing temperatures: 54, 55, 56, 57, 58, and 59 °C. Within this range, there was no detection at KR-M, with melting points differing from the previous mispriming test. When a gel was run out using electrophoresis, the standards continued to show a band at 160 bp, while two samples from control sites (BORR-UT-1 and BORR-B-1) showed multiple bands at all annealing temperatures. We

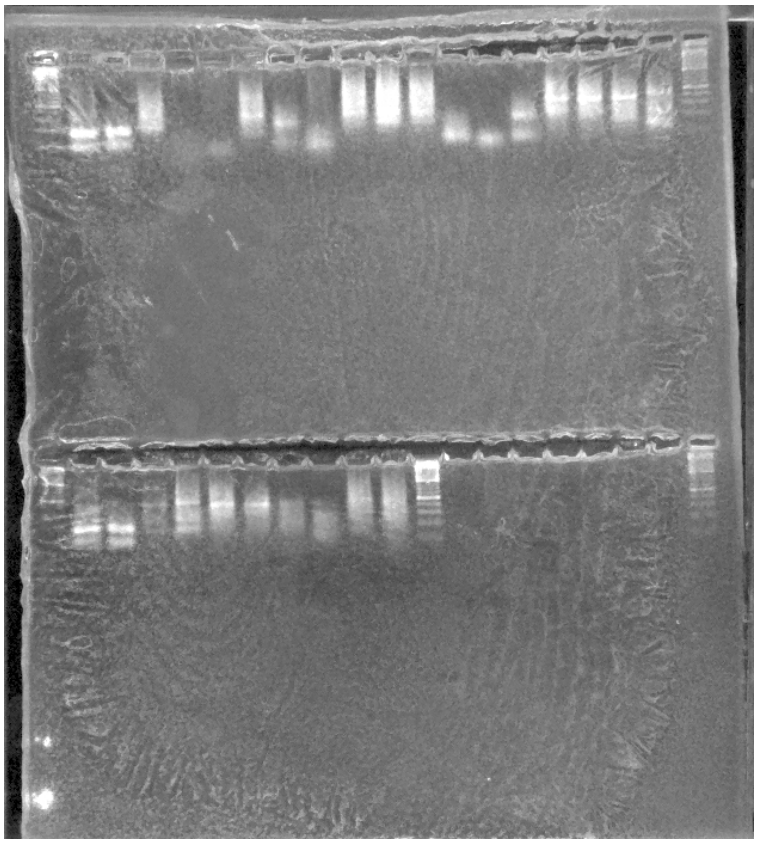

Figure 4.5: Snapshot of agarose gel electrophoresis with two Rib standards (two left-most wells after the ladder in each row) and pond samples in each gel. None of the samples show a single band around 160 bp, the size of the Rib standards.

concluded that the mispriming cannot be corrected by adjusting annealing temperatures, and new primers were selected.

The qPCR assay was again tested using a synthetic DNA block of 160 bp in length, which amplified well under the new primers (Rb-ITS 4 Fa/R and Rb-ITS 4 Fb/R) and cycling conditions (annealing temperature at 60 °C). Again, the standard amplification curves reflect the serially decreasing concentration of standards and a uniform melting point of 79 °C (Figure 4.7). However, negative samples continued to amplify with cycle threshold values similar to those of the lower concentration standards (1–100 copies/well). For one set of primers (Rb-ITS 4 Fa/R), the melt curves for the samples had two peaks, with one near the melting point of the standards; for the other set (Rb-ITS 4 Fb/R), the melt curves are completely unlike those of the standards, which suggests negative samples with primer-dimer. In the case of both primer sets, one of the samples (KR-M-1) had a melt curve similar to the standards', which is consistent with results from previous assays.

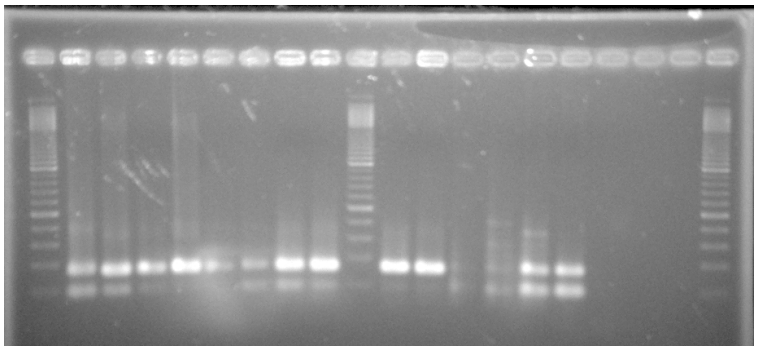

Figure 4.6: Snapshot of agarose gel electrophoresis with ten Rib standards (ten left-most wells after the ladder) and five samples from KR-M with different annealing temperatures: 48, 52, 54, 57, and 60 °C (left to right). At 54 and 57 °C, there are two clear bands with one at 160 bp.

Mispriming was frequently encountered when following published techniques, as well as newly developed sets of primers, resulting in lack of detection of *R. ondatrae* with certainty or confidence at any sampled site. Two sources of mispriming are hypothesized: contaminants in the pond samples and non-specificity of primers. Primer design is non-trivial because while SYBR Green-based detection is both simple and cost efficient, the SYBR Green dye has medium specificity (cf. TaqMan-based detection with high specificity) and binds to any matching double-stranded DNA product, increasing the risk of mispriming and false positive detection in samples. Furthermore, contaminants in samples that interfere with amplification hinder qPCR genotyping and quantification. Therefore, these eDNA sampling and qPCR

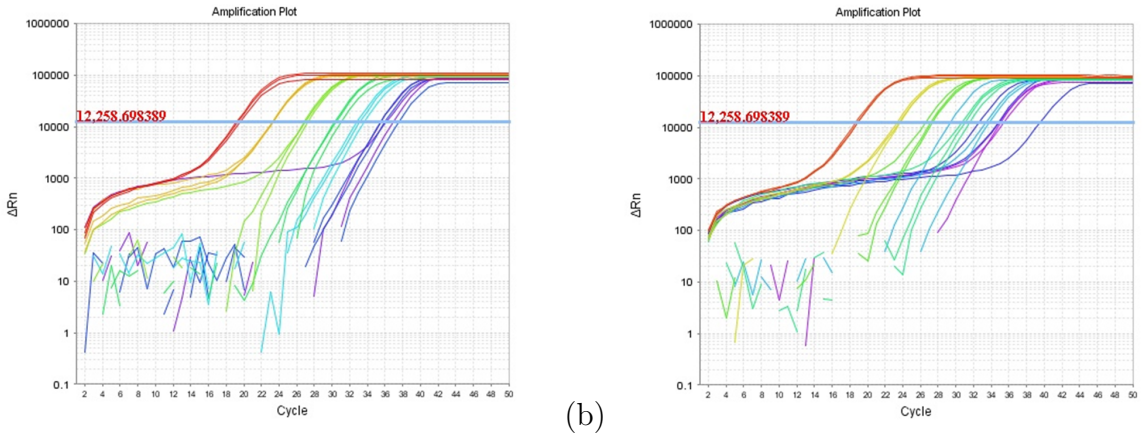

(a) (b)

Figure 4.7: qPCR amplification curves for Rib standards using a) Rb-ITS 4 Fa/R and b) Rb-ITS 4 Fb/R primers.

methods are not easily applicable for detection of *R. ondatrae* from these ponds.

B. dendrobatidis (Bd)

Kirshtein et al. (2007)'s qPCR assay was initially tested using a synthetic DNA block of 146 bp in length, which amplified well under the primers (ITS1-3 Chytr and 5.8S Chytr) and cycling conditions (annealing temperature at 60 °C). With a serial dilution, a set of standards using this synthetic block was made to be used in a standard curve. The standard assay produced amplification curves as shown in Figure 4.8, which reflect the serially decreasing concentration of standards and a uniform melting point of 73 °C.

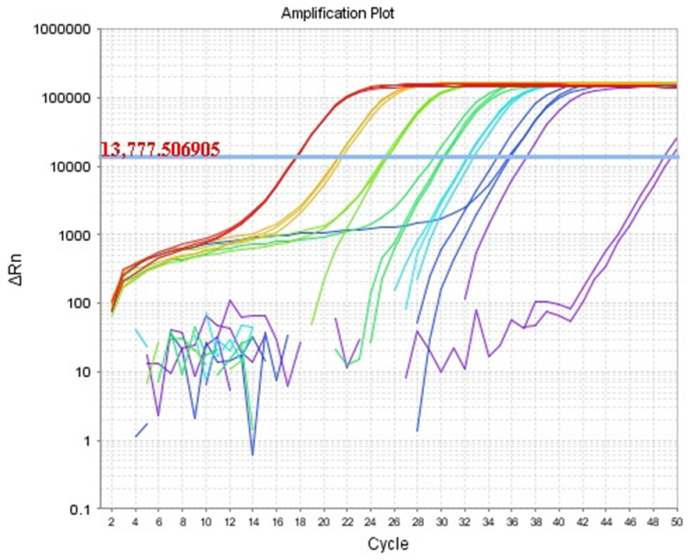

Figure 4.8: Amplification curves for Bd standards.

However, nearly all samples from May to September, including those from known positive sites, showed no amplification (Figure 4.9), though when pond water from a control site (i.e. Bd-negative) was spiked with Bd standards, amplification occurred. Because it is far more common to find traces of disease in water via eDNA sampling without having the disease persist in amphibians in a pond, rather than not catching traces based on sampling location, the negative results suggested the presence of inhibitors (e.g., ions, metals, humic acids) that could be retained in filtration. Several samples remained a dark color post-extraction; this dark color is due to humic acids that inhibit the PCR reaction. To test for such inhibitors, samples were cleaned up using a purification kit, and a spiked well (cleaned-up sample plus 100 copies) was run on the same plate.

When the cleaned-up samples for known positive sites were run in the thermocycler, they showed amplification. The standards showed serially decreasing concentration of Bd and the no-template control showed no amplification. Around 100 copies/well or µl of Bd

was observed at GP-G and 80 copies/µl was observed at GP-MA. Additionally, the spiked well showed +100 copies, suggesting that the sample qPCR runs are not inhibited post-clean up step. The melt curves and melting points of the samples, however, did not match those of the standards. Samples from these sites were run out on an agarose gel with electrophoresis (Figure 4.10), in which standards showed a single band around 146 bp, as well as some primer-dimer. None of the samples, however, were at this size, reflecting the different melt curves produced from the qPCR assay. This could be another example of a case in which using a more specific detection method, such as the TaqMan assay, would help distinguish between amplification of the target, Bd, and amplification of another organism of a similar size. Due to this mispriming, there was a lack of detection of Bd with certainty or confidence at any sampled site. Again, these eDNA sampling and qPCR methods were deemed not easily applicable for detection of *B. dendrobatidis* from these ponds.

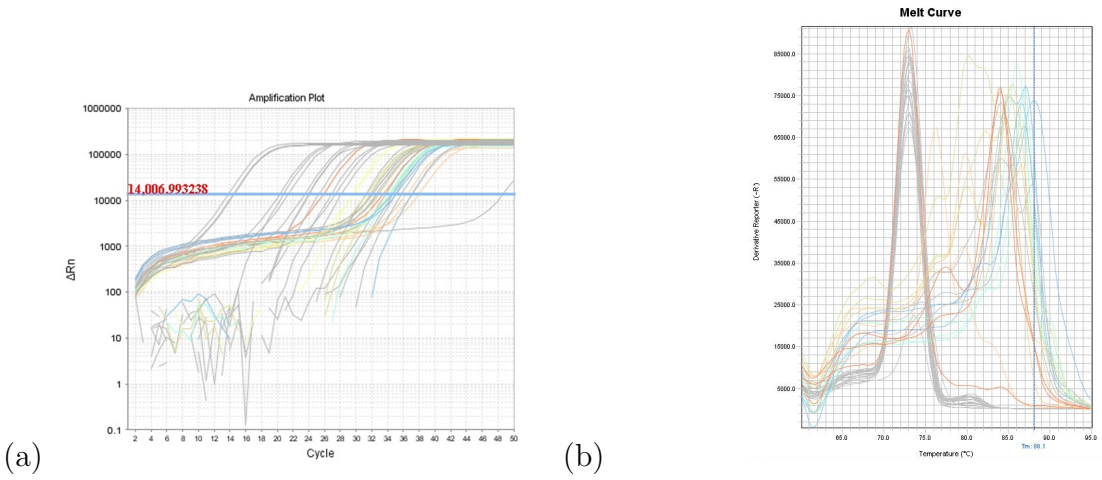

Figure 4.9: a) Amplification and b) melt curves for standards (grey) and Bd pond samples. Samples from known positive sites show amplification up to 100 copies/well. However, sample melt curves show a different amplicon than the standards.

4.4 Conclusion

Northern California amphibian populations have been forced into marginal habitats such as vernal pools and farm ponds as watersheds have been degraded by hydrologic and land use change. Endangered frogs and salamanders may result in loss of ecosystem resilience and render the system more fragile and vulnerable. Therefore, protection of these habitats through collaborative management between hydrologists, ecologists, and managers is crucial. In these ponds, correlation between ChlA concentrations and disease presence was expected to increase through positive correlation, yet be subject to the dynamics of the disease hosts;

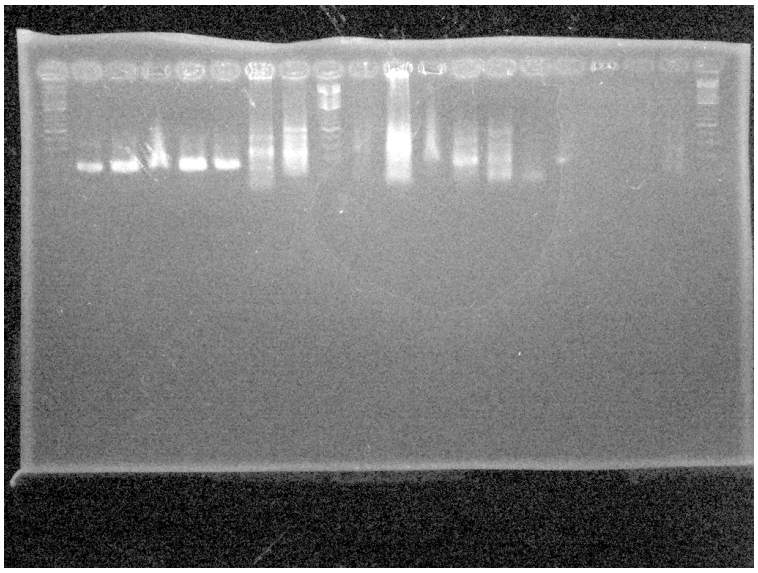

Figure 4.10: Snapshot of agarose gel electrophoresis with five Bd standards (five left-most wells after the ladder) and pond samples. None of the samples show a single band around 146 bp, the size of the Bd standards.

however, the tested eDNA and qPCR methods were not able to successfully detect *R. ondatrae* or *B. dendrobatidis* in a subset of ponds in the Southern Coast Range. This work demonstrates the roadblocks for innovative sampling methods and robotics platforms to be used in addressing water quality and disease issues. Significant challenges associated with monitoring and predicting water quality in large-scale, dynamic freshwater ecosystems remain and inhibit understanding of transport processes. Though the UAS water sampling platform can help better enable interactions between non-expert operators and robots to ensure safety of operators and the environment, eDNA techniques for disease detection need to be further evaluated in the field and laboratory to ensure accurate results and conclusions regarding the health of amphibian habitats. Establishment or improvement of simple and non-invasive methods, however, will help overcome the current limitations in the evaluation of amphibian habitat quality using the UAS and the development of effective management plans.

Chapter 5

Cold-water zone detection in streams

5.1 Introduction

The seasonal thermal regime of rivers worldwide varies from relatively stable (e.g., an annual temperature range of 20–30 °C in the Mekong and similar tropical rivers) to highly variable (e.g., an annual temperature range of 0–25 °C in rivers such as the Missouri that experience continental climates) (van Vliet et al., 2013). The magnitude of these annual swings in stream temperature depends on atmospheric conditions, which are responsible for river surface heat exchange (Mohseni et al., 2003; Pilgrim et al., 1998; Sinokrot et al., 1995), stream discharge, which controls rivers' thermal capacity through mixing (Sinokrot and Gulliver, 2000; van Vliet et al., 2011), and catchment topography and morphology, which shape heat fluxes and flow regimes (Caissie, 2006). Rising summer water temperatures and declining low flows, expected with climate change and increased seasonal extrema (Arnell, 1999; Nijssen et al., 2001), threaten freshwater habitats for aquatic species with low physiological tolerance for high temperatures (Balcombe et al., 2011; Bowler et al., 2012; Eaton and Scheller, 1996; Mohseni et al., 2003; Todd et al., 2005; Wilby et al., 2010). For example, water temperature is important for fish growth (Elliott, 1975; Elliott and Hurley, 1997), the development of eggs (Combs, 1965), as well as the timing of fish emergence from gravel (Beer and Anderson, 2001; Elliott et al., 2000) and movement (Jensen et al., 1998); temperatures can similarly affect aquatic invertebrates (Cox and Rutherford, 2000; Markarian, 1980) and primary producers (Power et al., 2015). Therefore, increases in summer water temperatures can potentially lead to long-term changes in species assemblage (Daufresne and Boet, 2007; Hawkins et al., 1997; Morrongiello et al., 2011). Cold-water habitats, or refugia, are thus crucial for sustaining biodiversity in river ecosystems.

Summer thermal refugia, an essential mitigating feature in warming rivers, can result from cold-water inputs from tributaries (Ebersole et al., 2015; Sutton et al., 2007), groundwater seeps and upwelling (Brunke and Gonser, 1997; Constantz, 1998; Ebersole et al., 2001), thermal stratification (Matthews and Berg, 1997; Matthews et al., 1994), and channel shading (Bowler et al., 2012; Crook and Robertson, 1999; Ebersole et al., 2003). Refugia are

particularly important in seasonally-dry, Mediterranean-type climates, where peak radiation and air temperatures coincide with minimum streamflows in unregulated rivers, exaggerating summer warming (van Vliet et al., 2013). For example, in Northern California, the sustainability of populations of economically, culturally, and ecologically significant salmonid fishes is already believed to be dependent on such refugia (Sutton et al., 2007; Sutton and Soto, 2012). The importance of thermal refugia is only likely to increase with warming air temperatures and increasing water demands and therefore their identification and characterization are essential for conservation and vulnerability assessment. However, understanding how the extent of cold-water zones that form refugia covaries with changes in air temperature, flow regime, or changing watershed land use remains challenging in part because of difficulties associated with observing heterogeneous temperature fields over spatially distributed river systems.

Field researchers have several options for measuring the thermal structure of water bodies, and specifically temperature variations occurring at small spatial scales across cold-water zones. Selection of any method, however, typically represents a tradeoff between spatial resolution, temporal resolution, and the spatial coverage of observations. For example, manual observations of temperature require the presence of a researcher and ingress into the water body. Temperature measurement locations must be selected to maximize the probability of detection of temperature heterogeneities and are followed by intensive sampling, presenting workload challenges and limiting observations to accessible reaches, thereby resulting in potentially sparse datasets that preclude characterization of smaller cold-water zones that require finer-scaled sampling (Ebersole et al., 2001, 2003). As an alternative to manual measurements, in situ sensors can be deployed to increase frequency of sampling or to monitor over longer periods. Nevertheless, such sensors are typically fixed in space, often requiring local knowledge or reconnaissance for strategic placement of costly sensor grids to adequately describe long-term spatial distributions of cold-water zones (Matthews and Berg, 1997). Distributed temperature sensing is a more recently developed in situ technique that uses travel-times for light within a fiber optic cable to infer local variations in temperature (Selker et al., 2006). While providing greater longitudinal spatial coverage along the cable transect, its data is limited to capturing temperatures in the longitudinal transect. It generally does not provide lateral or vertical temperatures unless the cable is coiled, meaning that this method cannot detect cold-water inflow that occurs outside of the cable's monitored reach (Buck and Null, 2013). Lastly, thermal infrared imaging (TIR) can also produce observations of spatially continuous and extensive temperature fields by using the relationship between intensity of emitted radiation of a water body with radiant temperature to infer kinetic temperatures (Torgersen et al., 2001). Although used to characterize thermal refugia in stream reaches, TIR assumes that the surface water temperature measurements are valid representations of stream temperature (Torgersen et al., 2001, 1999b). As the temperature effects of cold inflows must be visible at the stream surface to be captured by thermal imaging, subsurface inflows that create cold-water zones are difficult to detect using TIR.

Many of the spatiotemporal challenges associated with stream temperature monitoring can be overcome with unmanned aerial systems (UAS), which offer the potential for exten-

sive spatial coverage and sampling of river systems, even in hard-to-access areas. Previous work (Chung et al., 2015; Ore and Detweiler, 2018) introduced an innovative aerial thermal sensing platform that lowered a temperature sensor into a shallow water body in a lentic ecosystem to record temperatures throughout a water column. The system was able to capture mean temperature variations in space and time as recorded by in situ sensors, including identification of the thermocline, with accuracy similar to that associated with other methods. Mixing disturbances induced by the vehicle were comparable in magnitude to background perturbations in the water column. The tests in the lake system demonstrated that a grid of UAS-derived data could be interpolated to generate a high-resolution map of the 3D thermal structure of the water body. However, it remains unclear how effective a UAS platform could be in mapping small-scale temperature heterogeneities, such as those forming thermal refugia. Some refugia (for example, directly under riparian vegetation or undercut banks) are clearly inaccessible to flying platforms. Thermal refugia generated by cold-water inflows from confluences or groundwater inputs should be accessible to a UAS, but the question remains whether given the operational limitations of a UAS platform and the energetic mixing processes that arise in lotic environments (Lewis and Rhoads, 2015b; Rhoads and Kenworthy, 1995, 1998), a UAS can be operated in such a way as to locate and accurately characterize these refugia.

The aim of this study is to firstly evaluate the performance of the UAS temperature monitoring platform in a lotic environment, and in doing so characterize the set of operational limitations that might constrain design of stream-based sampling campaigns. We then develop a series of synthetic temperature fields using an idealized modeling study and explore the ability of different sampling designs to reconstruct these fields, subject to the constraints identified during field tests. Both components of the study focus on important processes for generating thermal refugia: confluence mixing and groundwater discharge. The field evaluation took advantage of existing in situ temperature sensors installed in the South Fork Eel River at confluences of cold-water tributaries with a warmer main stem channel. The modeling study focused on groundwater inflow, which is generally more difficult to characterize in terms of relevant discharge and length scales, and thus poses an appropriate test bed for considering UAS performance and sampling design. Finally, we discuss the potential values and limitations of a UAS in this application and suggest key areas for improvement of aerial platforms that will shape new UAS-based data collection methods.

5.2 Methods

Study sites

The study sites comprise two densely monitored confluences between the main channel of the South Fork Eel River and its tributaries Elder Creek and Cedar Creek. The South Fork Eel River drains a 1784 km^2, mostly forested and minimally regulated catchment in Mendocino County, Northern California. The river is primarily fed by groundwater inflows (Salve et al.,

2012). The forested tributaries maintain stream temperatures close to that of groundwater inputs (10–17 °C) year round, while the main stem is more exposed to solar radiation and becomes much warmer (>20 °C) during summer low flow conditions. These summer stream temperatures are close to or exceed the thresholds for physiological stress in the river's populations of anadromous salmonids including steelhead (*Oncorhynchus mykiss*), which have experienced steady population declines since the late 19th and early 20th centuries (Anderson, 2005). Ongoing observations suggest that during periods of elevated summer main stem water temperatures, cold-water tributaries such as Elder and Cedar Creeks, along with groundwater seeps, provide habitat that is preferentially used by salmonids (Wang et al., prep).

The two study confluences differ in terms of stream bathymetry and local shading of the channels (Figure 5.1). Elder Creek flows steeply over the cobbles of a tributary delta before entering a deep pool in the main stem. The confluence is shaded by abundant near-channel vegetation and coastal conifer forest. Cedar Creek gradually slopes into the South Fork Eel River at a sparsely vegetated riffle about ten miles downstream of Elder Creek. Both confluences were monitored using a dense grid of in situ temperature sensors (Elder: 97 sensors; Cedar: 101) sampling every hour. The grids extended from just upstream of the confluence to several meters downstream (Elder: 22 m; Cedar: 37 m), with downstream spacing of 4 m and cross-stream spacing of 1–2 m. Due to the variable bathymetry and water depth at each confluence, the number of temperature sensors and their depths in the water column were not uniform across the vertical arrays at each grid point. A maximum of 5 HOBO Pendant temperature loggers were installed per vertical array, deployed at roughly equidistant intervals from the stream bed to just below the water surface.

Vehicle and sensors

The UAS platform is an Ascending Technologies Hummingbird quadcopter that has been custom-equipped with a 6 m flexible cable, spooling mechanism, and pressure-temperature sensor system consisting of a thermistor and piezoresistive pressure sensor (Figure 5.2 and Table 5.1). The Hummingbird quadcopter is 0.54 m in diameter and weighs 510 g unloaded, with a total system weight of approximately 650 g with the pressure-temperature sensor system. This sensor system differs from that used in Chapter 3, which recorded temperatures using the built-in temperature sensor of the pressure sensor with a slower response time. The current pressure sensor is also suited for a larger range of pressure for measurements in deeper water bodies. The cable and spooling mechanism allow the sensor to be held close to the vehicle during flight and lowered before measurement. Temperature measurements are taken by lowering the UAS altitude such that the unspooled sensor moves through the water column until reaching the stream bed; the UAS is then flown higher to raise the sensor out of the stream before moving to the next location. An on-board GPS provides coordinates for geo-location. Two 2.4 GHz XBee radio links are installed on the UAS: The first establishes wireless communication of GPS and altimeter data between the vehicle and computer ground

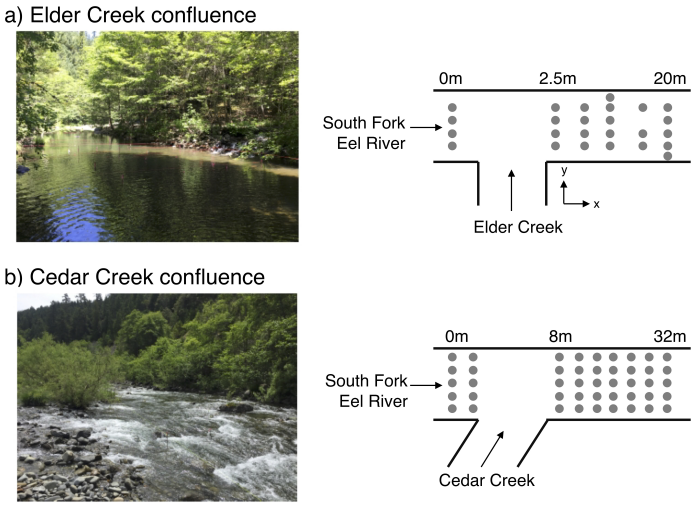

Figure 5.1: Study confluences and locations of in situ temperature sensor arrays. Sensor grids are not to scale.

station, and the second reads the pressure-temperature sensor system data and broadcasts to a data-logging ground station.

	Pressure	Temperature
Name	MS5803 05BA	US Sensor GP103J4F
Type	Piezoresistive	NTC thermistor
Operating range	0–5 bar	-40–300 °C
Accuracy	±120 mbar	
Resolution	0.036 mbar	0.1 °C

Table 5.1: Sensor specifications for the UAS pressure-temperature sensor system.

Field measurements

To evaluate the performance and identify the operational limitations of the UAS thermal sensing platform in a stream environment, four UAS temperature surveys were conducted at the two tributary study sites. Temperature data was collected with the UAS at Elder confluence on July 10 and September 2, 2016 and at Cedar confluence on July 11 and September 4, 2016. Flights took place in the afternoon, with air temperatures of 21 to 29 °C

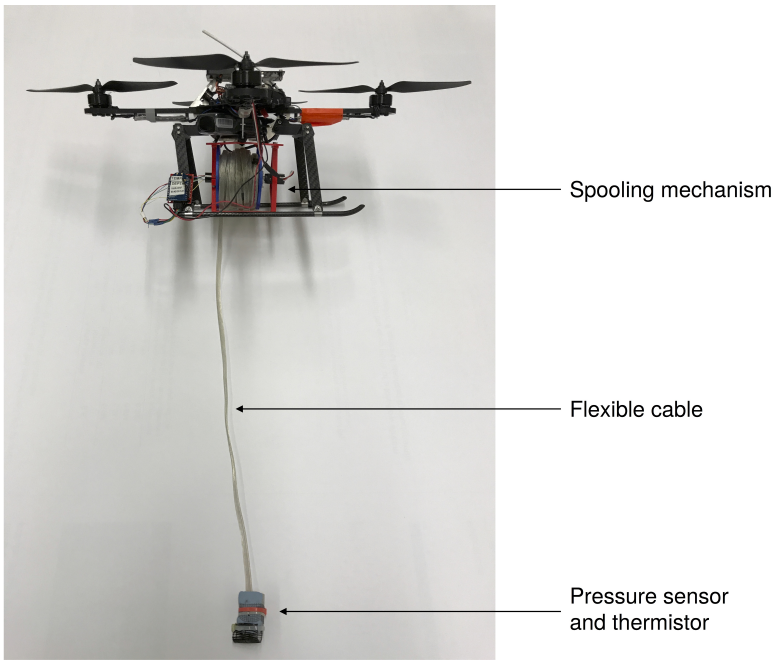

Figure 5.2: The UAS platform with its pressure-temperature sensor system. The pressure-temperature sensor system is updated with a thermistor with a faster response time and a pressure sensor whose pressure-depth range is larger.

and average wind speeds of 1.2 m/s. UAS temperature observations were collected at or half-way between in situ vertical sensor arrays.

UAS performance was evaluated by comparing the spatial extent of cold-water zones inferred from the temperature observations made by the UAS platform and in situ sensors during the sampling period; UAS temperature data was compared to in situ sensor temperature data from the same hour. Specifically, we compared the temperatures observed at each in situ sensor location and the spatial autocorrelation of the thermal fields inferred by trilinear interpolation between all observation points. Spatial autocorrelation was measured as Moran's I, a measure of multi-dimensional autocorrelation, ranging from -1 to 1; zero indicates a random spatial pattern while a positive I suggests positive spatial autocorrelation (Moran, 1950). For both platforms, we also examined correlation length scales, or the maximum distance at which similar values are still clustered together. Correlation length scales were calculated as the distance where I=0.5, as this value of I signifies strong positive spatial correlation.

We also evaluated the positional accuracy of the UAS measurements by comparing the reported data of the UAS's on-board, conventional GPS, with locations of the in situ sensor grids. Detailed flight observations were recorded during all flights, allowing us to note additional operational constraints on the UAS.

Idealized modeling

The modeling scenarios focused on groundwater inflows to a riffle-pool sequence under low flow conditions typical for the dry season. The riffle-pool sequence provides a representative geomorphic unit found throughout the South Fork Eel River and many other systems (Montgomery and Buffington, 1997). As in the South Fork Eel River, groundwater inflow in the model was provided by bedrock fractures in the stream bed, located along either the centerline of the riffle or the pool in the model. The idealized model considered combinations of stream discharge, bed geometry (e.g., sinusoidal amplitude and wavelength, with a wavelength-to-width ratio of around 1, comparable to commonly reported ratios (Trauth et al., 2013)), and groundwater flux (e.g., vertical flux and location of fracture), with the range of parameters selected to represent field-observed dry-season conditions in the Eel River Watershed. Information about groundwater vertical fluxes in the Eel River Watershed is not available, and thus the range was based on data from similar rivers (Gerecht et al., 2011). The parameters used are shown in Figure 5.3 and Table 5.2.

The mixing and transport of groundwater inflows through the riffle-pool sequence are described by the Navier-Stokes equations in three dimensions, coupled with the heat transport equation. These equations were solved in OpenFOAM (Weller et al., 1998), an open-source computational fluid dynamics model, using the buoyantBoussinesqPimpleFoam solver and run to steady state. OpenFOAM's blockMesh mesh generation utility was used to create a 3D, hexahedral mesh of the stream channel. Boundary conditions under hydrostatic pressure were set to: zero at the stream bed and walls, slip at the surface, and zero normal gradient at the outlet. Initial conditions were set to reflect stream discharge, Q, at the inlet, and groundwater vertical flux, w_{gw}, at the groundwater inflow location. Temperature was initially set to have zero normal gradient everywhere other than the inlet and groundwater inflow location.

Parameter	Value
Stream slope	1%
Stream width	15 m
Stream discharge, Q	1.5, 5 cu. m/s
Amplitude of riffle-pool sequence, A	0.5, 1, 2 m
Wavelength of riffle-pool sequence, λ	10, 20 m
Groundwater vertical flux, w_{gw}	6×10^{-6}, $3{\times}10^{-5}$ m/s
Groundwater fracture location	riffle, pool

Table 5.2: Model parameters used in CFD simulations of an idealized riffle-pool sequence.

Synthetic UAS sampling

We evaluated two contrasting operational modes that highlight certain constraints of UAS temperature monitoring in streams: 1) GPS-guided sampling, which relies on GPS for posi-

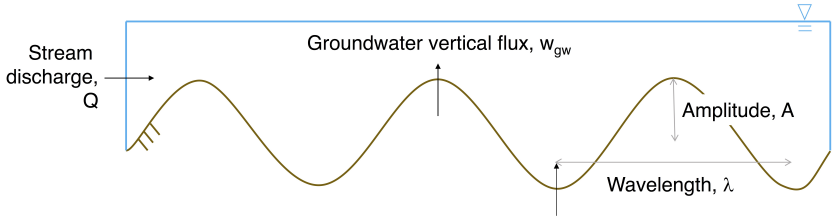

Figure 5.3: Model setup with parameters used in CFD simulations of an idealized riffle-pool sequence.

tional accuracy but reduces operator fatigue, allowing for more observations per flight; or 2) manual sampling, which allows greater precision and accuracy in the location of temperature measurements but reduces the number of observations achievable, as pilots become fatigued while operating the UAS in manual mode. We also identified two measurement densities: Spatially intensive measurements would enable detection of fine-scale thermal features but could potentially miss interesting phenomena at larger scales, while extensive measurements would be intended to make a broad survey of thermal patterns without resolving finer details of thermal structure.

Given these constraints, we devised multiple sampling strategies corresponding to automated and manual flight modes with varying measurement densities. Manual sampling was simulated by limiting observations to 30 points per UAS survey, based on the field experiences which suggested that 30 sample locations represented the upper-end of a feasible manual UAS flight. Three manual sampling grids were designed based on the wavelength of the pool-riffle sequence. Intensive sampling corresponded to ∼5 stream cross-sections per half wavelength of the riffle-pool sequence and 6 measurements per cross section, with all cross-sections situated either upstream or downstream of the simulated groundwater inflow location and covering the inflow location. Extensive sampling corresponded to ∼5 cross-sections per wavelength, covering the entire riffle or pool. GPS-guided sampling allowed 50 observations per survey, constrained primarily by battery life, with ∼8 stream cross-sections per wavelength of the riffle-pool sequence with 6 measurements per cross section, covering the entire riffle or pool. In total, this yields four synthetic sampling strategies that were used to "observe" the thermal structures generated by cold groundwater inflow into a warm main stem channel, generated through idealized modeling.

Synthetic observations were made from the model output by extracting the modeled temperature at each x-, y-, z-coordinate in the sampling grid. To simulate positional errors in GPS-guided sampling, we added uniformly distributed noise (Monte Carlo; 100 runs) to the grid point locations from the GPS-guided sampling runs; we assumed that there was zero positional error associated with manual sampling (Table 5.3). However, we note that this is a simplification of positional error, as GPS error can partly be due to atmospheric effects that cause a positional offset, which drifts over time. For each of these runs, uniformly distributed noise (Monte Carlo; 10 or 100 runs, GPS-guided or manual sampling run, respectively) was added to the temperature data to account for UAS sensor error observed during field surveys. The range of the uniformly distributed additive error terms was set to match the observed errors found during the field campaigns (Section 5.3).

Sampling strategy	No. of obs. points	Cross-section (cs) spacing	Location error (m)	Temperature error (°C)
Manual: intensive, upstream	30	5 cs/half λ	–	$\pm$0.88
Manual: intensive, downstream	30	5 cs/half λ	–	$\pm$0.88
Manual: extensive	30	5 cs/λ	–	$\pm$0.88
GPS grid	50	8 cs/λ	$\pm$3	$\pm$0.88

Table 5.3: Grid and additive error properties of the four synthetic sampling strategies.

Having extracted synthetic "observations," we used trilinear interpolation to reconstruct a 3D thermal field on the same mesh grid used to initially solve the model. The reconstructed synthetic temperature field was then compared to the original model output temperature field by evaluating the R^2 value for a linear regression of the interpolated temperatures against the original model temperatures at each grid point. The R^2 values provide a quantitative measure of the ability of each operational mode and measurement density to resolve stream thermal structures for a given model.

To define a range of in-stream conditions under which the UAS could resolve the thermal structure of cold-water zones, we focused on the model cases where R^2>0.5. Additionally, we examined the horizontal mixing length scales of each model case, which is a function of channel depth, stream water velocity, shear velocity, and width (Fischer et al., 1979). The horizontal mixing length scale in channel flow describes the mean free path of a water particle undergoing mixing in channel flow, where longitudinal distribution of a tracer (e.g., cold inflow) occurs under the influence of turbulent shear dispersion.

5.3 Results

Operational constraints on UAS use

During the field surveys, the UAS was subject to operational challenges related to the system platform and environmental conditions. Thirty seconds to 1 minute were required to measure

temperatures across the <1.5 m deep water column at each sampling location. Measurements were made at ∼30 locations in 20 minutes with 2 batteries (∼15 locations per battery). Although the on-board GPS used multiple (5+) satellites for geo-location in all surveys, GPS measurements were highly uncertain, with an absolute horizontal accuracy of 3 m (WAAS TE Team, 2017), compared to the 2 m sampling grid. Consequently, positions of measurements were obtained from the fixed in situ sensor arrays, rather than the GPS data. Flight times were not affected by differences in the surface area of the two sites. Environmental conditions, however, affected the UAS performance. The high flow velocities during early-summer measurements (u=0.15 m/s) exerted sufficient drag on the sensor cable to prohibit lowering of the sensor to the stream bed. This drag also imposed additional uncertainty regarding the location of the temperature sensor and tended to pull the UAS downstream, requiring continuous manual adjustment of the UAS position. These issues were not problematic during late summer studies when velocities were lower. The combination of drag on the sensor, relatively high wind speeds, and riparian vegetation and rocks near the channel all required extensive operator adjustment of UAS position during the flights. Consequently, operator exhaustion was the most obvious operational challenge associated with the UAS temperature surveys.

Resolution of thermal structures by UAS field observations

The UAS temperature measurements were in good agreement with temperatures measured by the in situ sensors (p<0.05, paired t-test): UAS-measured temperatures were within ±1.5 °C of in situ sensor-measured temperatures over the four surveys (Table 5.4). The average (mean) absolute temperature difference between the two platforms was 0.88 °C, which is comparable in magnitude to deviations from traditional in situ sensors seen in other temperature sensing methods (e.g., TIR (Torgersen et al., 2001); fiber optics (Selker et al., 2006; Tyler et al., 2009)).

Measurements from the UAS, however, were not perfectly linearly related to the in situ observations (mean R^2=0.47). Rather, the error in measured temperature between the two platforms varied as a function of both water column position and flow velocity. The absolute temperature difference decreased with increasing depth, from a 2.3 °C average difference in sampled points near the surface of the stream to a 1.1 °C difference at a depth of 1.5 m in the water column. Errors also decreased with decreasing flow velocity: The observed temperature differences were higher in July under high flow conditions than in September, and R^2 values also increased at the end of summer.

At larger scales, the longitudinal temperature distributions obtained by interpolating observations from the in situ sensors and the UAS were similar. At Elder confluence, cold-water input from the tributary entered the main stem of the South Fork Eel River, where cross-flow was low, and traveled downstream through the thalweg while having little effect near the inner bank. Both the UAS and in situ sensors, whose measurements covered the same sampling domain, identified a warm zone near the inner bank and a cold-water zone spanning much of the cross-stream width and extending approximately 10 m downstream

Confluence, month	No. of in situ sensors	No. of UAS data points	Mean absolute temperature difference (°C)	S.E.	R^2
Elder, July	72	7010	0.998	0.155	0.130
Elder, September	57	3812	0.227	0.081	0.718
Cedar, July	89	10256	1.493	0.574	0.412
Cedar, September	76	2298	0.799	0.368	0.636

Table 5.4: Average absolute temperature differences between UAS and in situ sensor measurements.

of the confluence, as seen in Figure 5.4a. However, differences in the interpolated thermal structure at Elder confluence were observed in the vertical profiles. During the July survey, the UAS recorded much cooler temperatures at the stream surface than at depth, while the in situ sensors recorded decreasing temperatures with increasing depth.

At Cedar confluence, the cold-water zone was pinned to the inner bank with a strong cross-flow from the main stem in the early summer months, but moved away from the bank towards the thalweg with decreased flows. In Figure 5.4b, interpolations from in situ sensors and the UAS showed the dispersion of cooling effects from the tributary in the cross-stream direction. However, the UAS's longitudinal interpolated thermal structure and vertical profiles differed from those observed by the in situ loggers at Cedar confluence. Longitudinally, the temperature distribution interpolated from the UAS was characterized by sharp and uneven gradients. Cross-stream, the UAS-derived profile showed depth-dependent mixing of the thermal gradient while the in situ sensor-derived profile showed a vertically uniform thermal gradient from the cold tributary to the warmer outer bank.

We observed reduced spatial autocorrelation of the temperature field reconstructed by the UAS observations as compared to the field reconstructed from observations from the in situ sensors. At Elder confluence, the correlation between pairs of points as distance between them is increased showed similar patterns, in both the longitudinal and lateral directions. The lateral, cross-stream correlation length scales, however, diverged between the two platforms, with a shorter UAS correlation length scale as seen in the correlograms in Figures 5.5b and c. At Cedar confluence, the UAS had a shorter correlation length scale but detected very different longitudinal and lateral spatial structures (Figures 5.5d, e, and f) compared to the in situ sensors.

Idealized model output

The idealized model output reproduced expected flow features of a riffle-pool sequence. For example, in each modeled riffle-pool sequence, there was a lateral convergence of flow at the pool entrance and divergence at the pool exit, where convergence and divergence refer to the spatial transverse velocity patterns in flow. Velocity and bed shear stress in the riffle were greater than in the pool, consistent with previous studies (MacWilliams et al., 2006;

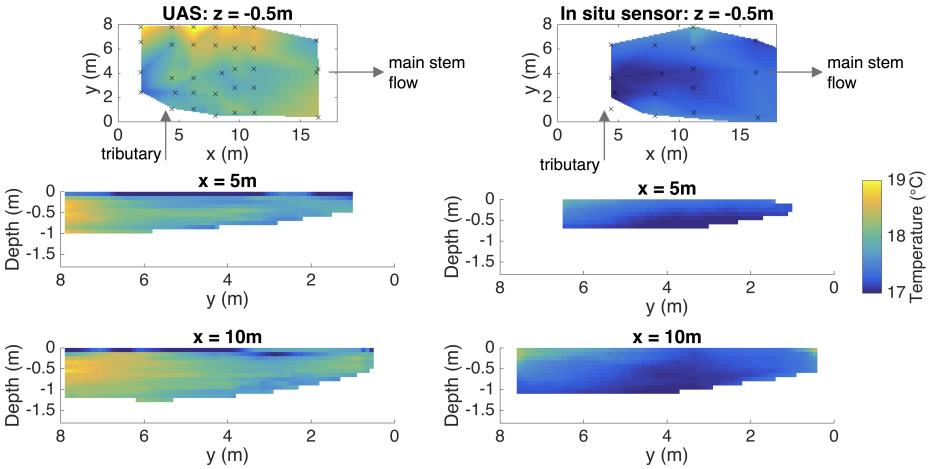

a) Elder confluence, July

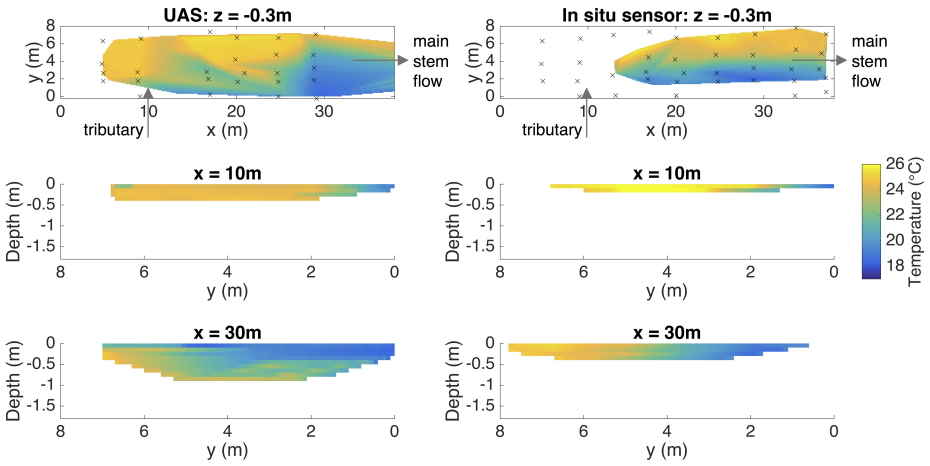

b) Cedar confluence, July

Figure 5.4: Interpolated thermal structures show similarity in the longitudinal direction but differences in lateral cross-sections of the stream at a) Elder and b) Cedar Creek confluences. ×s indicate the locations of measurements with the UAS temperature sensor or in situ sensors.

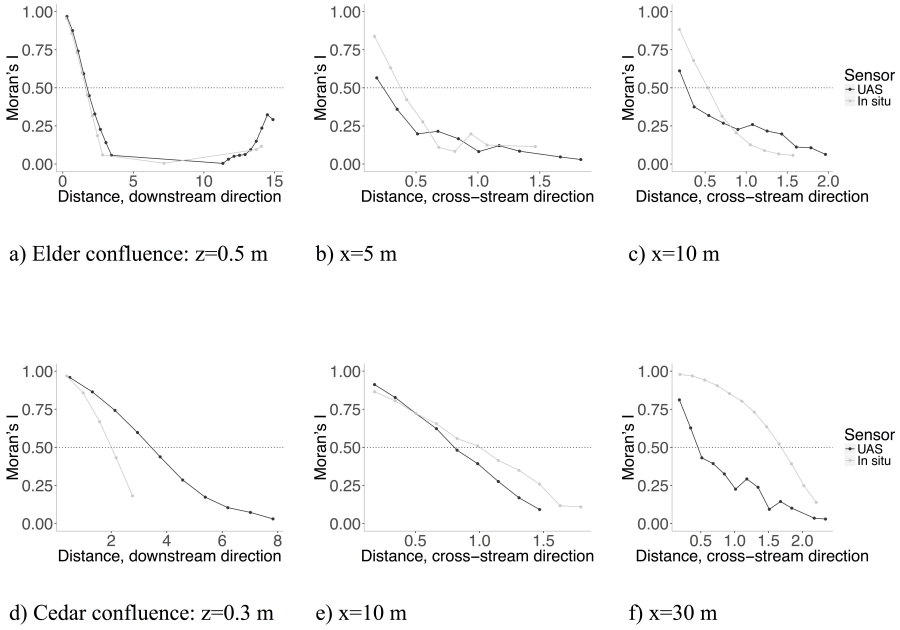

Figure 5.5: Correlograms of autocorrelation vs. distance. a)–c): In July at Elder Creek confluence, UAS's detection of a cold surface layer results in differences in lateral correlograms between the in situ and UAS sensors. d)–e): At Cedar Creek confluence, longitudinal and lateral thermal structures differ between the two platforms.

Rodriguez et al., 2013). Surface divergence was also observed at the riffle. Furthermore, increased velocities were observed with increasing Q, as expected (Booker et al., 2001).

Resolution of thermal structure by synthetic UAS sampling strategies

Across the series of synthetic sampling experiments, increasing R^2 values (interpolated temperatures vs. modeled temperatures, representing the ability of the sampling strategy to resolve the thermal structure of the cold-water zone created by groundwater inflow) were observed with decreasing amplitude, A, wavelength, λ, and stream flow velocity Q (Table 5.5). The highest R^2 values were found in cases of pools with low A and λ (mean R^2=0.68), and were independent of Q. Conversely for riffles, where much higher velocities and turbulent kinetic energy (TKE) lead to quick dispersion of groundwater inflow, the R^2 values for all cases were below 0.5, independent of the in-stream parameters. Changes in magnitude

of groundwater inflow flux had a negligible effect on the diffusion of groundwater inflow and thus the temperature field.

When we compared the synthetic manual and GPS-guided sampling strategies, we found that manual sampling outperformed GPS-guided sampling when groundwater inflow occurs in pools, with 9 vs. 0 (of 23) with R^2>0.5 and mean R^2 of all cases equaling 0.31 vs. 0.02. With manual sampling, we observed that the intensive grid upstream of and covering the groundwater inflow location resolved the thermal structure of cold-water zones across the range of in-stream parameters explored in the idealized models, while the intensive downstream grid and extensive grid were unable to resolve the thermal structure in all but few cases.

Furthermore, for manual sampling, we observed a general improvement of R^2 when the horizontal mixing length scale of the pool exceeded the sampling grid resolution, as shown in Figure 5.6. In cases where the sampling grid resolution was smaller than the mixing length scale due to decreased depth of the channel, synthetic UAS sampling was able to resolve the thermal structure of the cold-water zone from groundwater inflow. When the grid resolution was larger than the mixing length scale in cases with deep pools, synthetic sampling data did not capture the temperature heterogeneities and was not able to accurately resolve the thermal structure.

Parameter	Value	Mean R^2
A	0.5 m	0.39
	1	0.28
	2	0.25
λ	10 m	0.52
	20	0.12
Q	1.5 cu. m/s	0.37
	5	0.24

Table 5.5: R^2 values for manual sampling experiments of groundwater inflow in pools.

5.4 Discussion

A comparison of UAS- and in situ sensor-derived temperature data shows that the two platforms are comparable in resolving the main flow behavior and thermal structures produced when a cold inflow interacts with stream surface water. The UAS platform offers several advantages: It is able to overcome the spatial constraints of currently used methods, sample on a fine grid throughout the water column, and offers increased resolution of vertical fine-scale variability of the water column compared to in situ sensor arrays. This results in improved detection of spatial coherence and structure in temperature fields for fine spatial scales. Because thermal refugia require coherence in cold-water zones, the UAS platform can

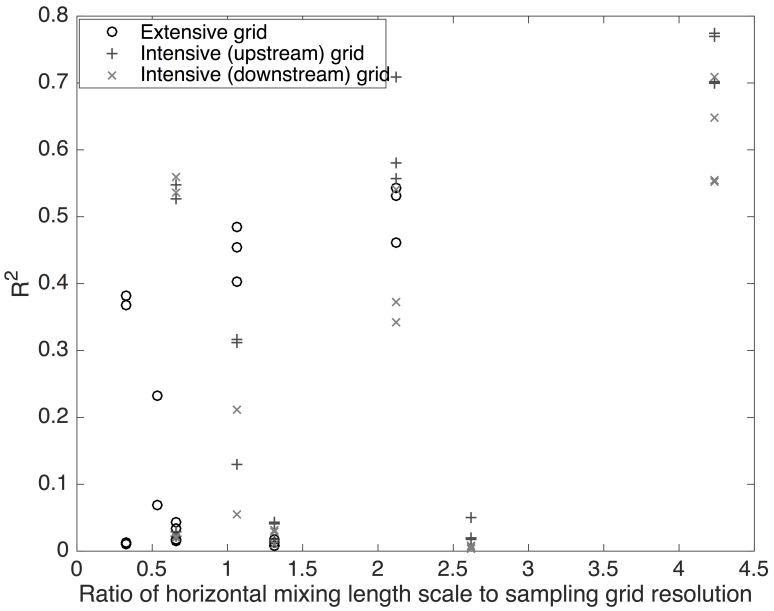

Figure 5.6: R^2, or the ability of the UAS sampling strategy to resolve the thermal structure of a cold-water zone, increases with increasing ratio of horizontal mixing length scale to sampling grid resolution in manual sampling mode.

assist in more accurate identification of the cold-water zones that result in critical habitat under high temperatures and low flows.

This advantage, however, is constrained by the choice of measurement location and coverage that can lead to errors in interpolated thermal structures. Measurement locations that are irregularly spaced or provide partial spatial coverage of temperature variations can result in interpolation artifacts such as sharp thermal gradients or patch-like nature of isotherms. Unfortunately, this can pose a challenge to researchers because the full spatial coverage of thermal interactions in the field may initially be unknown. While tributary confluences are visible, the exact location of groundwater discharge is often times unknown. In this case, employing a range of measurement densities can be useful. Extensive sampling with a large grid resolution can help zero in on locations with thermal heterogeneity; once these locations have been detected, an intensive sampling grid can capture the small-scale thermal variations. An intensive grid upstream of the inflow location in the pool is preferred to a grid downstream: Upstream sampling grids will better capture the spatial extent of a cold-water zone, as deeper pools can also increase recirculating flow that does not interact with the primary streamflow, resulting in circulation and an asymmetric distribution of cold inflow upstream. Furthermore, high flow or high wind conditions can also introduce error to UAS temperature measurements, as increased wind or flow results in instability of the UAS and

can induce mixing of the water column by the sensor and cable. Drag on the sensor and uncertainty of data location can compound with any errors in sampling grid or domain to produce further interpolation artifacts and hinder the understanding of the spatial extent of cold-water zones. Though Ore and Detweiler (2018) found that in lentic water, the pressure-temperature sensor's depth accuracy was not associated with lateral disturbances such as wind and GPS drift, this study suggests that the effects of flow drag on the sensor's positional accuracy in lotic environments may need more consideration.

In addition to these challenges, the UAS platform's use in environmental flows is limited due to inherent hydrodynamic processes that affect the resolution of thermal gradients. When using trilinear interpolation to reconstruct 3D thermal structures from point-scale temperature data, the horizontal mixing length scale is the primary determinant of resolvable structures. Because trilinear interpolation effectively smooths out thermal gradients between sampling points, the distance between points should be shorter than the mean free path of a water particle. If the sampling resolution is larger than this length scale, the measurement locations cannot fully resolve the existing thermal structure. This can result in false smoothing of gradients in interpolation or missing small-scale temperature heterogeneities entirely.

We conclude that an ideal UAS sampling strategy to characterize potential cold-water stream refugia should be based on a ratio of horizontal mixing length scale to sampling grid resolution that is greater than 1. This, however, is limited by both the system and operational constraints of the UAS platform and in-stream conditions. As the depth of a stream increases from 1 to 4 m, the horizontal mixing length scale decreases from approximately 5.5 m to 1.4 m. Current GPS horizontal accuracy and resolution of 3 m constrain temperature sampling with the UAS to the shallow reaches of a stream channel (depth <2 m), and thus, the manual sampling operational mode is preferable to depending on the GPS coordinates for geo-location. Yet, manual operation while sampling, in which the sampling grid must be visually approximated by the operator and coordinates assigned in post-processing, is subject to operator exhaustion and limits the sampling grid size to 30 sampling locations. Therefore, the UAS's ability to detect thermal signatures of cold-water inflows in streams is currently limited to 30 sampling locations in confluences and small, shallow pools (<150 m^2, 2 m depth) under low-flow conditions. This unfortunately restricts the detection of potential cold inflow-fed thermal refugia for salmonids to select locations along the stream.

Because the current state of the on-board GPS serves as a major system constraint, future work should primarily focus on obtaining accuracy in horizontal positioning, as improvement of the UAS's GPS unit can provide more accurate measurement coordinates and decrease the sampling grid resolution. Decreased dependence on manual sampling can also relieve operational exhaustion, thereby increasing the maximum number of sampling points per survey. This would improve detection of small cold-water zones that serve as critical habitat and widen the range of in-stream conditions for which the UAS can provide data on hydrodynamically-important temperature structures. There are several options: The current on-board GPS unit could be used in conjunction with another unit placed at a fixed, known location that serves as a reference, or it could be replaced with a real-time kinematic

(RTK) unit that allows centimeter-level position accuracy, a significant improvement over the meter-level accuracy of traditional GPS receivers. Replacement of the on-board GPS unit with a new unit, however, requires careful consideration of payload and likely a slightly larger UAS.

Lastly, the use of the UAS platform can also be useful for other applications. Climate change, resulting in shifts in temperature and precipitation (Arnell, 1999; Nijssen et al., 2001), coupled with increased land use (Beguería et al., 2003; Tu, 2009), are predicted to alter the flow regimes and hydrodynamic environments of water bodies worldwide. Temperature is an easily measured physical variable that can be used to both determine a background state of thermal structure and characterize such changes with hydrodynamic modeling (Beletsky and Schwab, 2001; Gooseff et al., 2005; Komatsu et al., 2007). We have shown that the horizontal mixing length scale should ideally be larger than the sampling grid resolution. In large rivers, deltas, and lakes with anisotropic mixing due to stratification, the vertical scales are much smaller than the horizontal scales, and eddy sizes and the horizontal mixing length scale can reach up to basin scale (Fischer et al., 1979). In ecohydrologically-important bodies of water, especially where difficult to monitor, the UAS may be able to provide data from which more accurate spatial patterns or distributions can be inferred than from in situ sensors. From these thermal structures, researchers can then understand the hydrodynamics and ecological processes governing the water body to evaluate the effects of a changing environment.

5.5 Conclusion

Unmanned aerial systems are able to capture vertical temperature profiles at multiple sampling locations to overcome the spatial constraints of currently used methods and provide high resolution, 3D temperature data. When used to resolve in-stream thermal structures and understand the extent of cold-water zones, the additional sampling points gained by the use of the UAS allows finer-scale variabilities in water temperature to be detected, assuming that the appropriate spatial domain is sampled. This can aid researchers in identifying locations in stream reaches with cold inflows that act as dry-season thermal refugia for threatened salmonids. Currently, however, use of the UAS platform is constrained by its system and operational limitations, as well as the hydrodynamic processes in stream environments that influence measurements. To accurately characterize cold-water zones that may serve as critical habitat and sustain stream ecosystems, the sampling strategy must facilitate manually taking temperature measurements at a spatial resolution that is finer than the inherent horizontal mixing length scale of the stream reach. Because such limitations are the dominant controls that determine the maximum number of sampling points per survey, as well as sampling resolution, improvement of geo-location is considered the top priority for future development of the aerial platform.

Chapter 6

Cold-water zone detection along stream networks

6.1 Introduction

In freshwater ecosystems, temperature is a primary determinant of habitat quality. Changes in water temperature affect food supply, disease, competition, and migration patterns, which in turn influence species composition and distribution of the stream biotic community (Bowler et al., 2012; Wilby et al., 2010). Increasing summer water temperatures and declining low flows, expected with climate change and increased seasonal extrema (Arnell, 1999; Nijssen et al., 2001), threaten aquatic species with low physiological tolerance for high temperatures (Balcombe et al., 2011; Bowler et al., 2012; Eaton and Scheller, 1996; Mohseni et al., 2003; Todd et al., 2005; Wilby et al., 2010). Under these conditions, freshwater fish, invertebrates, and primary producers must seek cold-water habitats where they can take advantage of the cooler, stabilized temperature regime of groundwater-fed zones (Bjornn and Reiser, 1991; Brunke and Gonser, 1997; Constantz, 1998). Thermal refugia are particularly important in seasonally-dry, Mediterranean-type climates, such as in Northern California, where peak radiation and air temperatures coincide with minimum streamflows to exaggerate summer warming in unregulated rivers (van Vliet et al., 2013).

Identification of refugia along a river network and fine-scale thermal characterization are therefore essential for inferring the state of critical freshwater habitat and management of these ecosystems. However, zones resulting from groundwater-surface water interactions are difficult to detect, unlike cold-water refugia arising in shaded riparian sites or at the confluence of cold-water tributaries with main stem streams. By contrast, the sites of groundwater entry to surface waters are cryptic, posing a challenge to the initial detection of these groundwater-fed cold-water zones along a river.

Initial identification of cold-water zones at the basin scale is limited by the extent of current methods available to researchers to detect groundwater intrusions in flow. Standard measurements of groundwater flow into a stream are made with mini-piezometers, which are

inserted into the streambed to obtain estimates of vertical hydraulic gradient and hydraulic conductivity (Baxter et al., 2003; Dahm et al., 2006). Such measurements are feasible only in easily accessible areas and at small spatial scales. Temperature (i.e. heat transport) is thus increasingly used as a tracer for groundwater (Anderson, 2005; Constantz, 2008): Field researchers have several options for measuring the thermal structure of water bodies, but all options have inherent tradeoffs between spatial and dimensional coverage (Chung et al., 2015). Due to these tradeoffs, multiple methods are often used in concert to observe groundwater-surface water exchange in stream networks (Briggs et al., 2013; Hare et al., 2015). In situ temperature sensors, which are fixed in space, can be deployed in a high density grid to capture fine-scale temperature variations (Matthews and Berg, 1997), but such grids become costly when exceeding the stream reach scale. Distributed temperature sensing (DTS) can produce spatially extensive and continuous temperature fields but is confined to measurements at the stream bed, rendering three-dimensional (3D) observations of stream temperature along a network a challenging task (Buck and Null, 2013; Torgersen et al., 2001, 1999b).

Thermal infrared (TIR) imaging is one field technique that has been successful in providing point-in-time evaluations of groundwater seepage zones across large spatial scales. TIR can be ground, airborne, and satellite-based (Banks et al., 1996; Deitchman and Loheide, 2009; Handcock et al., 2006), and can produce observations of spatially continuous and extensive temperature fields by using the relationship between intensity of emitted radiation of a water body with radiant temperature to infer kinetic temperatures (Torgersen et al., 2001). TIR's surface measurements can be useful in the initial detection of stream surface temperature anomalies (Briggs et al., 2013; Deitchman and Loheide, 2009; Hare et al., 2015). Specifically, airborne TIR has been used to map potential thermal refugia (Dugdale et al., 2015; Kurylyk et al., 2015; Monk et al., 2013), defined as any discrete area of the river channel at least 0.5 °C cooler than the main stem ambient water temperature and greater than 1 m^2, over 700 km of streams (Dugdale et al., 2015) and geo-locate thermal plumes prior to collection of temperature profiles over large spatial scales (DeMario et al., 2017).

TIR provides a skin or surface measurement and assumes that the surface water temperature measurements are valid representations of stream temperature (Torgersen et al., 2001, 1999b), meaning that its data cannot be used to understand the full, 3D thermal structure of a stream reach. This dimensional challenge associated with TIR stream temperature monitoring, however, can be overcome with the emergence of TIR cameras designed specifically for use with small unmanned aerial systems (UAS), which have the ability to combine fine-scale temperature monitoring and extensive spatial coverage. Our UAS platform, which includes an immersible pressure-temperature sensor system, has previously been shown to be comparable to traditional in situ temperature sensors in temperature measurement accuracy (Chapter 3) and ability to resolve the 3D thermal structure of cold-water zones, i.e. potential in-stream thermal refugia. Furthermore, previous work suggests that the UAS can be used in small, shallow (depth, h<2 m) pools to resolve the 3D thermal structure of cold-water zones with minimal disturbance to the water column or natural environment (Chapter 5).

Even when used in concert with a UAS platform, accuracy of TIR imaging for ground-

water detection in streams can be expected to be significantly affected by environmental and physical factors. TIR has so far been shown to be able to identify seepage zones only where groundwater-surface water mixing was expected to measurably modify the water temperature, such as in shallow reaches (z<0.5 m) with moderate flow or where groundwater seeps were relatively strong (2% of surface water discharge) (Hare et al., 2015). Additionally, because TIR measures infrared radiation, thermal measurements can be influenced by both the emissivity and reflectivity of the target surface, as well as absorption and emission by atmospheric conditions (FLIR Systems, 2016). The influence of neighboring surfaces also manifests in a degradation in measurement accuracy due to effects of light, optics, and sensor image processing, known as the spot size effect (FLIR Systems, 2016).

The aim of this study was to evaluate the challenges associated with employing TIR imaging to detect cold-water zones under conditions when thermal refugia are ecologically essential: during the summer months, when the combination of high water temperatures and low flow minimize suitable habitat for freshwater species. A modeling study was undertaken to simulate idealized groundwater inflow into a stream and used to identify the in-stream conditions under which TIR imaging could detect cold-water zones generated by groundwater intrusions. Field data and observations made using a TIR camera on a small UAS, as well as an immersible temperature-pressure sensor system, were also used to define further limitations to detecting cold-water zones specific to this platform.

6.2 Materials and methods

Site description

The South Fork Eel River drains a 1784 km^2, mostly forested and minimally regulated catchment in Mendocino County, Northern California. The river is primarily fed by groundwater inflows (Salve et al., 2012) derived from bedrock seeps and springs. Ongoing observations in the watershed suggest that during periods of summer low flow conditions and elevated main stem water temperatures (>20 °C), groundwater inflows (10–17 °C) can provide habitat that is preferentially used by salmonids (Wang et al., prep).

At the two study sites in the Eel River Watershed (Figure 6.1), groundwater seeps have previously been observed through snorkel surveys. The first site, Elder Hill Pool, is a main stem pool fed by groundwater subsidies from a main stem tributary, Elder Creek; the short distance and elevation gradient between Elder Creek and the main stem results in a hydraulic gradient and potentially significant groundwater inputs into the South Fork Eel River. Seeps also occur further downstream at Wilderness Pool, though the exact mechanism of groundwater inflow remains less clear. Study areas of both sites (Elder Hill: 50 m^2; Wilderness: 60 m^2) were selected for temperature monitoring with the UAS, specifically to identify TIR imaging capabilities and collect data for use in the modeling study.

Figure 6.1: Study sites and areas along the South Fork Eel River.

Idealized modeling

The idealized modeling scenarios focused on lateral groundwater seeps to a stream reach under low flow conditions typical of the dry season in Northern California. As in the South Fork Eel River, groundwater inflow in the model was provided by bedrock fractures in the stream channel. Three groundwater inflow types (discrete seep, horizontal seepage face, and vertical seepage face) and two locations (near the stream surface, near the stream bed) were considered (Figure 6.2), as well as inflow volume as a percentage of main stem streamflow, ranging from 0.5 to 5%. A series of models was created using a factorial combination of model parameters (Table 6.1) for both riffle and pool reaches. Model parameters were chosen to represent field-observed dry-season conditions in the Eel River Watershed.

The mixing and transport of groundwater inflows through the modeled reach is described by the Navier-Stokes equations in three dimensions, coupled with the heat transport equation. These equations were solved in OpenFOAM (Weller et al., 1998), an open-source computational fluid dynamics model, using the buoyantBoussinesqPimpleFoam solver and run to steady state. OpenFOAM's blockMesh mesh generation utility was used to create a 3D, hexahedral mesh of the stream channel. Boundary conditions under hydrostatic pressure were set to: zero at the stream bed and walls, slip at the surface, and zero normal gradient at the outlet. Initial conditions were set to reflect stream discharge, Q, at the inlet, and groundwater discharge, Q_{gw}, at the groundwater inflow location. Temperature was initially set to have zero normal gradient everywhere other than the inlet and groundwater inflow

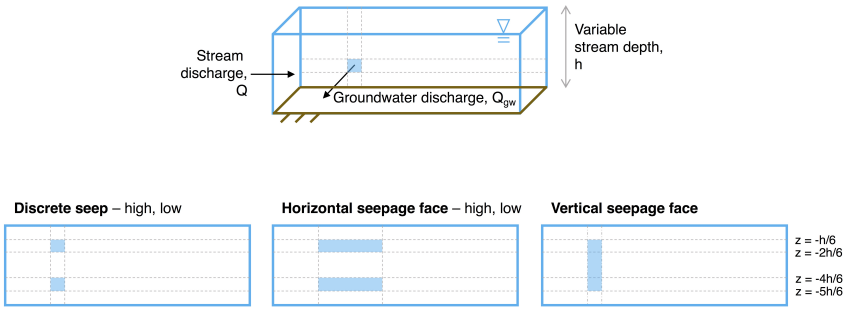

Figure 6.2: Model setup and parameters used in CFD simulations of idealized groundwater-surface water mixing.

Parameter	Value
Stream width	15 m
Stream depth, h	0.42, 1 m (riffle, pool)
Stream discharge, Q	2 cu. m/s
Ambient stream temperature, T	25 °C
Groundwater discharge, Q_{gw}	0.5, 1, 1.5, 2, 3, 4, 5% of Q
Groundwater temperature, T_{gw}	15 °C
Seep location	near stream surface (high), bed (low)
Seep type	discrete seep; horizontal, vertical seepage face

Table 6.1: Model parameters used in CFD simulations of idealized groundwater-surface water mixing.

location.

A cold-water zone in the model output was considered to be "detectable" by a UAS-TIR system if: 1) a temperature anomaly was located at the stream surface, 2) the anomaly was at least 0.5 °C colder than the ambient stream temperature (Dugdale et al., 2015), and 3) the anomaly was greater than 20 TIR pixels in diameter (FLIR Systems, 2016). The 3D thermal structure or temperature field of each model was reconstructed using trilinear interpolation of the model temperature output, and the structure was filtered for temperatures more than 0.5 °C colder than the ambient stream temperature, or the temperature at the upstream model boundary. At 10 m altitude flight, 20 pixels in an image spans 1.34 m of the target surface. Therefore, if the area of this cold-water zone exceeded that of a 1.34 m diameter circle, the groundwater inflow types and locations in the model were deemed to result in a cold-water zone accurately detectable by a UAS-TIR system.

Vehicle and sensors

The UAS platform, first introduced in Chapter 3 and updated in Chapter 5 is an Ascending Technologies Hummingbird quadcopter that has been custom-equipped with a 6 m flexible cable, spooling mechanism, and pressure-temperature sensor system consisting of a thermistor and piezoresistive pressure sensor. The quadcopter has a payload of 200 g and the pressure temperature sensor system weighs 140 g. As in previous studies with the UAS system (Chapters 3 and 5), direct temperature measurements are taken by lowering the UAS altitude such that the unspooled sensor moves through the water column until reaching the stream bed; the UAS is then flown higher to raise the sensor out of the stream before moving to the next location.

For TIR imaging, the spooling mechanism and pressure-temperature sensor system were replaced with a FLIR Duo R camera. The Duo R camera is an airborne dual-sensor thermal and visible light imager designed specifically for UASs. Camera specifications are shown in Table 6.2. For thermal imaging, the Duo R detects and images long wave infrared radiation. It is also equipped with the Multi Spectral Dynamic Imaging (MSX) feature, which provides visible camera definition and detailing to thermal images.

This camera was chosen specifically for its small size and payload. The camera (84 g) is powered by an external battery (119 g), for a total payload of 203 g. Data files are saved to an on-board microSD card.

FLIR Duo R	
Weight	84 g
Sensor resolution	160 × 120
Spectral band	7.5–13.5 µm
Thermal measurement accuracy	5% of reading
Visible camera resolution	1920 × 1080

Table 6.2: TIR camera specifications.

Thermal sensing in the field

Temperature and TIR data were collected with the UAS at Elder Hill and Wilderness Pools on August 12, 2017. Flights took place in the afternoon, with air temperature of 32 °C and average wind speed of 1.4 m/s. In addition to standard protocol checks, flights required ample prep time to secure the TIR camera on-board the UAS and switch between the TIR camera and the pressure-temperature sensor system (approximately 30 min each).

At Wilderness Pool, the UAS platform was flown twice over the study area: 1) with the Duo R camera at 10 m altitude, to identify any possible groundwater seepage zones (5 min flight) and 2) with the pressure-temperature sensor system, to collect direct stream water temperature data from the same location (5 min flight). Both IR and visible image videos were offloaded from the on-board microSD card. The IR video was checked for any

thermal anomalies that could indicate a cold-water zone in the river channel. The thermal anomalies were then compared to the visible image video to identify the possible sources of the anomaly and distinguish potential groundwater seeps from other sources, such as riparian shading or reflection, or camera errors. If an anomaly could not be attributed to other sources or camera errors, the cold-water zone was assumed to be fed by groundwater seeps and locations were recorded. The 3D thermal structure of Wilderness Pool was reconstructed using trilinear interpolation of the temperature data from the UAS's immersible pressure-temperature sensor system. The TIR-identified cold-water zones were compared to this thermal structure to evaluate physical presence in the stream, i.e. corroboration by water column temperature data.

At Elder Hill Pool, the UAS platform was flown only with the pressure-temperature sensor system to collect additional water temperature data (10 min flight). The 3D thermal structure of Elder Hill Pool was also reconstructed using trilinear interpolation of the temperature data from the immersible sensor. The 3D thermal maps from both sites were used in a qualitative analysis of existing seepage and stratification dynamics in the river channel.

Further testing of the TIR camera was conducted at San Leandro Bay, offshore from Bay Farm Island in Alameda County, Northern California on September 3 and 10, 2017. Testing took place in the afternoon, with average air temperature of 30 °C and average wind speed of 4.5 m/s.

6.3 Results and discussion

In models: Detecting cold-water zones with a surface signal

For the thermal signature of groundwater discharge in an idealized stream to be observed with confidence by a TIR camera, we found that the groundwater discharge generally needs to be at least 1% of stream discharge (Table 6.3).

In pools, both discrete groundwater seeps and seepage faces needed to be located close to the stream surface (located at z<-0.3 m in a 1 m deep pool) for their thermal signatures to be present at the surface. With seeps located close to the stream surface, cold inflow effects were observed both at the surface and the bed as the cold water spread from the discharge location in all three directions: longitudinally downstream, laterally cross-stream, and vertically toward the bed. When seeps, regardless of type, were located close to the stream bed, cold inflow effects were not observed at the surface (Figure 6.3) due to thermal stratification. With increasing groundwater discharge, water temperature decreased below the discharge location while the cold water increasingly spread longitudinally downstream and laterally, perpendicular to mean flow and away from the channel; however, the vertical effects were minimal through the water column.

In riffles, the thermal signature of groundwater was present at the surface regardless of type and location due to the shallower stream depth. With increasing groundwater discharge, water temperature decreased both at the stream surface and bed as the cold water

Seep location	Seep type	Stream reach	Min. $\frac{Q_{gw}}{Q}$ %	Area (m^2)
low	discrete	pool	–	0
low	discrete	riffle	1.5%	14.5
high	discrete	pool	0.5%	1.9
high	discrete	riffle	0.5%	2.4
low	horizontal seepage face	pool	–	0
low	horizontal seepage face	riffle	1%	13.4
high	horizontal seepage face	pool	1%	3.1
high	horizontal seepage face	riffle	1%	16.1
	vertical seepage face	pool	1%	3.3
	vertical seepage face	riffle	1%	16.4

Table 6.3: Measured area at the stream surface of the cold-water zone, as observed in each model scenario.

increasingly spread in all three directions. The cold-water zones in riffles remained pinned to the channel bank due to higher mean and stronger cross flow, while in pools, they tended to float away, perpendicular from the bank with high groundwater discharge (Figure 6.4).

In addition to groundwater thermal signature at the stream surface being strongly dependent on groundwater inflow location, the type of seep also governed the behavior of groundwater-surface water mixing and thus the spatial extent of the cold-water zone. Seepage faces have smaller cross-stream velocities than discrete seeps and thus resulted in less lateral, cross-stream spreading of cold-water and smaller area at the water surface of cold-water zones (Figure 6.5). A vertical seepage face, with less groundwater discharge focused near the stream surface, also resulted in a smaller cold-water zone surface area when compared to a horizontal seepage face located near the surface.

In the field: More TIR limitations

Thermal images from the UAS-TIR system at Wilderness Pool showed warmer ambient, main stem temperatures (lighter shades on greyscale palette), with colder thermal anomalies near the outer bank bedrock and in the thalweg (darker shades). There was little contrast of TIR in water, but contrast between the stream and landforms such as vegetation and rocks was observed. The thermal anomaly in the thalweg did not correspond to riparian shading as observed in the visible light image and was assumed to be derived from groundwater seeps. Water column temperature data from the immersible temperature sensor also showed cooler water temperatures, both at the stream surface and at depth, near the thalweg cold-water zone (x=6 m) than downstream (x>6 m). However, the TIR image was skewed by a camera reflection (Figure 6.6). The thermal anomaly located near the outer bank bedrock, on the other hand, corresponded in space to riparian shading (Figure 6.7) and thus could not be concluded to be sourced from groundwater seeps. Furthermore, this thermal anomaly could

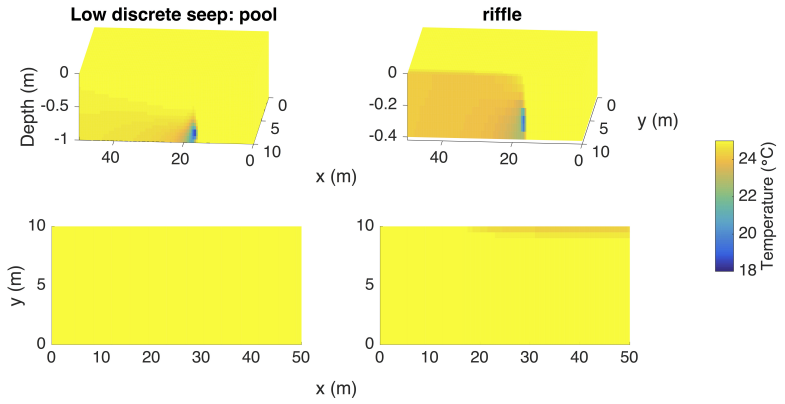

Figure 6.3: CFD model results show that when seeps are located close to the stream bed, cold inflow effects at the stream surface are observed to be negligible in pools but significant in riffles (Q_{gw}=1.5% of Q).

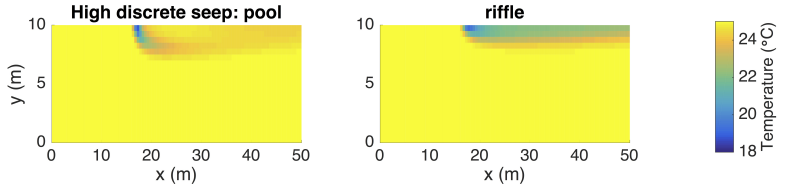

Figure 6.4: CFD model results show that in pools, cold-water zones float toward the thalweg, while in riffles, higher cross flow results in pinning of the cold-water zone to the bank (Q_{gw}=5% of Q).

not be verified by the immersible sensor, which recorded warmer temperatures with a thicker warm layer at the surface near the outer bank (y=3 m) than in the cooler thalweg (y=0 m).

Wilderness and Elder Hill Pools were both generally stratified, with cold temperatures (<19 °C) below z=-0.5 m (Figure 6.8). In deeper flow, thermal stratification by temperature-driven density differences can prevent the thermal signal of the cooler groundwater from reaching the water surface (Hare et al., 2015). Though a surface thermal signal was observed in the thalweg at Wilderness Pool (around x=6 m), no surface signals were observed in the more stratified Elder Hill Pool, perhaps suggesting density-driven stratification of a cold-water inflow that sinks upon entry into the stream channel.

Flights with the UAS-TIR system showed the many challenges associated with airborne

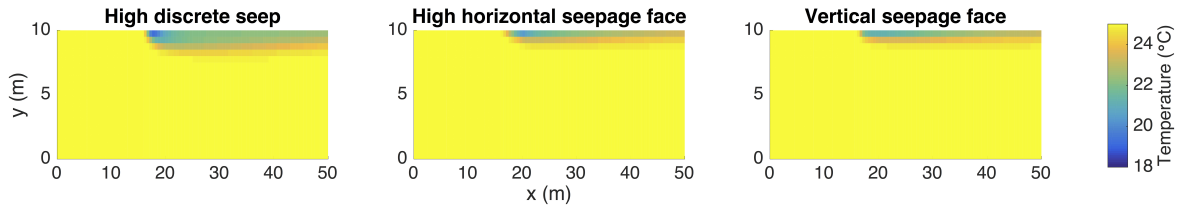

Figure 6.5: CFD model results show that the type of seep affects the behavior of groundwater thermal signature, with less lateral, cross-stream spreading of cold-water in seepage faces (Q_{gw}=1.5% of Q).

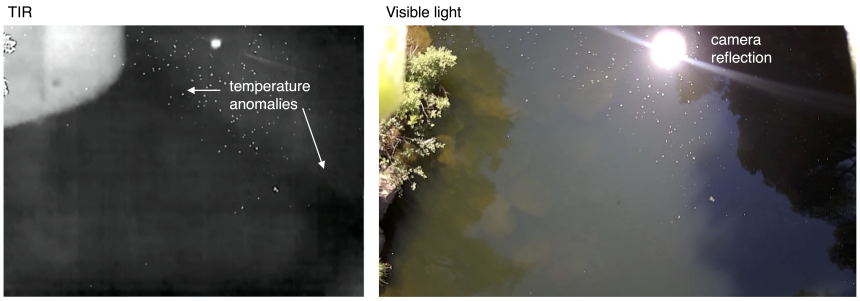

Figure 6.6: Comparison of TIR and visible light images shows that the thermal anomaly identified in TIR near the thalweg can be assumed to be sourced from groundwater seeps. However, a reflection of the camera is captured in both TIR and visible light images.

TIR. "Sun glints" were recorded in the thermal images due to the reflection of the sun against flows. Because the camera senses both heat from the target surface temperature as well as the reflected background environmental temperature, such reflections in the thermal image can cause temperature inaccuracies of hundreds of degrees. To minimize sun glints, the camera was initially affixed to make straight-on measurements, though straight-on measurements from the system in flight at 10 m altitude resulted in a camera reflection. Further testing with the TIR camera found that neither the camera angle nor altitude had an effect on the presence of sun glints in images, though an airborne system flying away from the sun reduced the sun glints. However, we did not observe camera reflections over an estuary, compared to reflections over the freshwater South Fork Eel River.

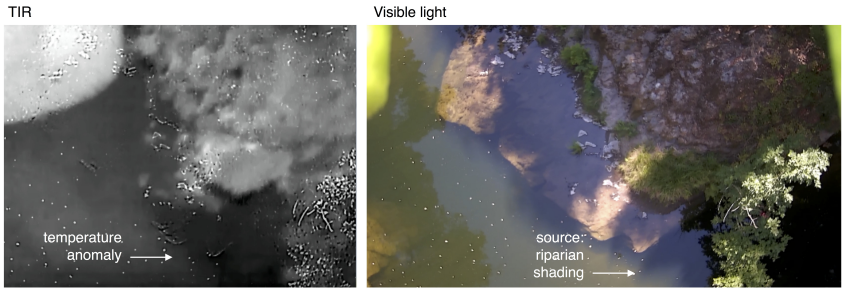

Figure 6.7: Comparison of TIR and visible light images shows that the thermal anomaly identified in TIR near the outer bank bedrock corresponds to riparian shading observed in the visible light image.

What does this mean for UAS-TIR systems?

Identifying cold-water zones serving as thermal refugia using TIR imaging can be complex, as detection depends on the expression of a surface thermal signal. To create a surface temperature anomaly that spans 20 pixels in diameter at 10 m altitude for airborne TIR, groundwater discharge needs to be at least 1% of stream discharge. In riffles, cold inflow at these rates from discrete seeps, horizontal seepage faces, and vertical seepage faces will produce a thermal signal with extensive spatial coverage at the stream surface. In pools, discrete seeps and horizontal seepage faces need to be located near the surface (z<-0.3 m) for cold inflow effects to be observed at the water surface.

This dependence on a surface expression and the effects of in-stream conditions on cold-water mixing, however, do not necessarily mean that TIR fails to detect the more cryptic thermal refugia. Cold-water zones are indeed created by groundwater discharge less than 1% of stream discharge and they exist in pools with cold inflows near the stream bed, but in either case, the cold-water zones may not be as valuable for freshwater species as those that result in surface thermal signals. For example, cold-water zones created by lower discharge rates are smaller in volume than those created by higher discharge and may not be preferentially used by fish. In pools, where groundwater discharge does create large-volume cold-water zones without a surface thermal signal due to thermal stratification, the same processes that establish these cold-water zones can increase concentrated hypoxic or anoxic regions (Ebersole et al., 2003). These cold-temperature regions in which groundwater with low dissolved oxygen levels dominates cannot serve as thermal refugia. In such cases, cold-water zones that do not have a thermal signature at the stream surface may not be suitable habitat for fish and are thus not a priority for detection.

Nevertheless, a set of limitations particular to small UAS-TIR platforms arises when employing airborne TIR for cold-water zone detection. Firstly, it is important to note that UASs must be typically flown a safe distance from riparian vegetation that may hang over

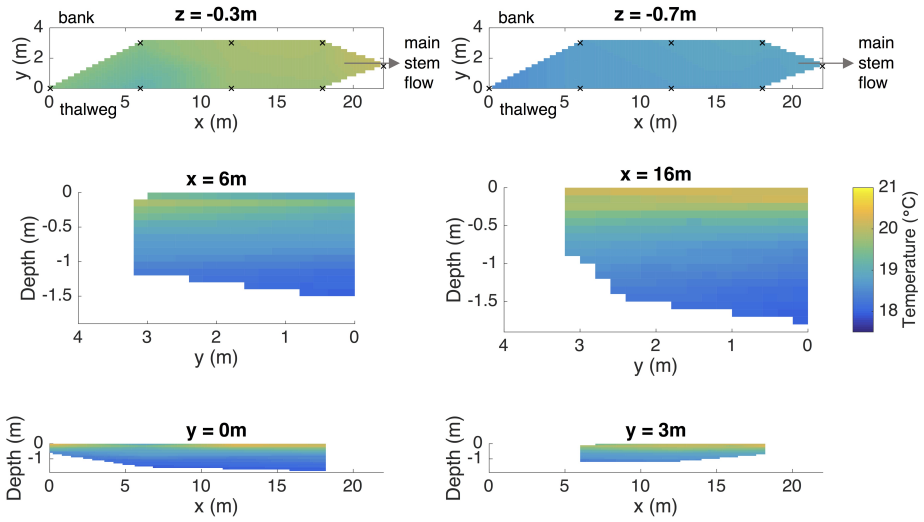

a) Wilderness Pool

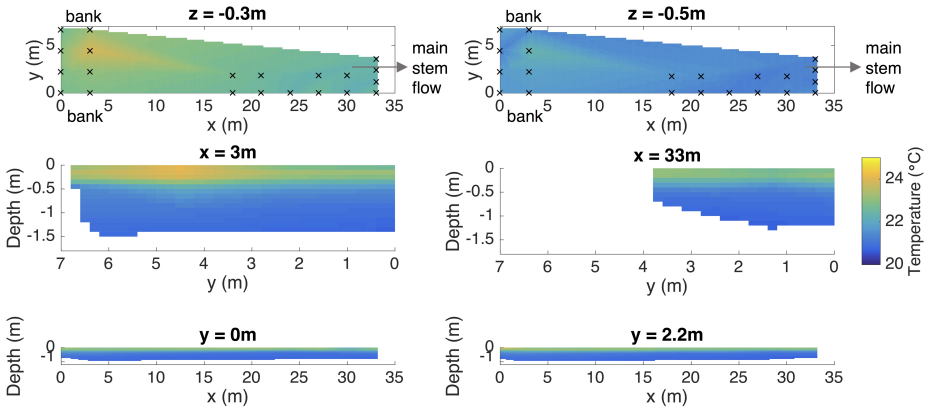

b) Elder Hill Pool

Figure 6.8: Interpolated thermal structures at a) Wilderness and b) Elder Hill Pools show few surface temperature anomalies with density-driven stratification of cold water. ×s indicate the locations of measurements with the immersible temperature sensor.

the bank to avoid collision or entanglement. A UAS-TIR platform may not be able to detect thermal anomalies at the water surface in riffles though cold-water zones resulting from groundwater discharge occur across multiple seep types and locations because such a zone will be pinned closer to the channel bank than in pools, where the cold-water zone can float towards the thalweg. Additionally, the challenges associated with using the UAS to directly measure stream temperatures in riffles have been discussed in Chapter 5.

While the use of the platform for identification of cold-water zones that serve as potential thermal refugia would be most useful in a summer-dry watershed, the hot atmospheric temperatures and relative humidity characteristic of coastal Northern California's dry season do not provide the ideal atmospheric conditions for TIR. A hot and humid atmosphere increasingly influences the thermal image as the atmosphere absorbs and emits TIR radiation based on air density and clarity. Furthermore, reflections of both the sun and the camera in the thermal image can result in inaccurate measurements (FLIR Systems, 2016). This combination of atmospheric effects and reflectivity of the target surface, the stream, results in the degradation of measurement accuracy, which requires researchers to use a higher number of pixels to accurately describe temperature anomalies in a thermal image.

There are a few established recommendations for avoiding these challenges in the field: The atmospheric effects can be reduced through lower flight altitudes and camera reflection can be minimized by avoiding straight-on measurements (FLIR Systems, 2016). However, we found that sun glints in flowing water could not be corrected by camera angle. Rather, sun glints were minimized when the UAS-TIR platform was directed in the opposite direction from the sun. And though the camera reflection could be avoided in an estuarine bay, we were unable to find a suitable solution in flights over a river, perhaps due to differences in salinity or bed material. Also, as the distance equivalent to one TIR pixel is determined by a camera's pixel pitch, focal length, and thermal sensor resolution, using a camera with a higher sensor resolution can expand the range of cold-water zone sizes detectable with negligible spot size effect. A larger UAS with an increased maximum payload could serve as a base for UAS-specific TIR cameras with higher sensor resolutions, as currently available models are larger than the FLIR Duo R used in this study. Another approach to increase the target surface distance per pixel is to fly the platform at a lower altitude; this, however, may complicate image post-processing as each image becomes confined to a smaller surface area of the stream with fewer identifying features and absolute horizontal GPS accuracy is currently limited to 3 m (WAAS TE Team, 2017).

6.4 Conclusion

TIR is often touted as a valuable technology for freshwater habitat assessment, as it has been shown to detect groundwater intrusion in streams by discerning the surface expression of a groundwater thermal signal. Our modeling study shows that cold-water zones created by groundwater-surface water mixing can be submerged with no surface thermal signal in a variety of cases. These cases, however, represent smaller-volume and potentially low-

oxygen zones, suggesting that TIR may indeed be capable of detecting the most valuable (i.e. large and oxygenated) habitat for freshwater species during an extended period of low flow conditions. Nevertheless, the operational and technical challenges specific to combining TIR and a small UAS vehicle pose limitations to using this new technology for identifying potential thermal refugia along a stream and certainly at the basin scale.

Chapter 7

Conclusion

Coastal Northern California faces a growing water budget deficit during its dry seasons due to its characteristic period of very low precipitation combined with warm summer atmospheric conditions. This deficit, exacerbated by increasing seasonal extrema and rising temperatures brought on by climate change, will increasingly threaten Northern California's terrestrial and aquatic ecosystems during their periods of peak ecosystem productivity. In forests and scrublands, diminishing availability of water resources is expected to result in increased plant water stress, whereas in ponds and streams, significant changes in thermal regime will threaten already-vulnerable freshwater habitats of species that are steadily experiencing population declines.

The work in this dissertation stems from the need to monitor the dry-season hydrologic balance and thermal regime of a watershed to accurately assess watershed conditions and understand their sensitivities to a changing climate. This dissertation harnesses existing technology, such as sensors and robotics, to create new field methods that allow field researchers to collect spatially distributed watershed data. A summary of methods and a synthesis of findings are presented below.

7.1 Part I: Quantifying fog water flux

Understanding coastal summer fog's quantitative effects on a watershed's water budget requires watershed-averaged estimates of fog water flux and evapotranspiration suppression. Despite observed spatiotemporal heterogeneity in fog occurrence and deposition, traditional averaging methods for precipitation do not consider the watershed features that may be spatially correlated to fog throughfall. The presented spatial averaging scheme (Chapter 2) employs a combination of cost-effective and easily deployable sensors recording point-scale observations, time-lapse imagery, remote sensing data, as well as watershed vegetation

and elevation data, to first identify areas of fog occurrence and then quantify variability in deposition with respect to canopy type and topography.

This scheme allows evaluation of the mechanisms through which fog contributes to and its effects on the overall water budget, and is based on the identified dominant controls of heterogeneity in fog occurrence and flux in the Upper Pilarcitos Creek Watershed: topography, vegetation, and interannual variability. Though throughfall inputs from coastal summer fog are small in volume at watershed scales, fog's suppression of evapotranspirational loss can significantly reduce summer water deficits (by 25%) in a San Francisco Peninsula watershed.

To be applied across all watersheds, an increased number of fog collectors and sensors can be deployed to monitor the effects of watershed features on fog water flux. In larger and more accessible watersheds, monitoring across several different degrees of fog exposure, topographic gradients, canopy conditions, and vegetation types is recommended using inexpensive leaf wetness sensors. The scheme can then be adjusted based on this data to reflect possible forest edge effects (i.e. noncollinearity between distance from the forest edge and elevation in a single watershed), dependence between vegetation and elevation, and throughfall-leaf wetness relationships specific to the watershed of interest.

7.2 Part II: Characterizing surface water thermal variations

To characterize how groundwater-fed inflows interact with the main stem streamflow to create cold-water zones that potentially serve as thermal refugia for freshwater fish, researchers need to be able to complete two tasks: 1) identify locations of cold-water zones along a stream network and 2) obtain detailed measurements of temperature at these locations. However, traditional methods for detection of groundwater-surface water interactions that use heat as a tracer have inherent tradeoffs between spatial and dimensional coverage that preclude researchers from accomplishing both tasks. In this work, an unmanned aerial system (UAS) platform is custom-equipped with a thermal infrared (TIR) imager (Chapter 6) and a pressure-temperature sensor system (Chapters 3 and 5) to create a mobile data collection system to conduct both tasks. Though the UAS platform provides detailed temperature measurements that can be used to reconstruct the three-dimensional thermal structure of known cold-water zones in several stream reaches of the Eel River Watershed, its use in initial identification of the cold-water zones remains a challenge due to operational and system limitations.

With the many challenges identified through field trials and modeling studies, it is difficult to advocate use of the UAS platform in place of traditional stream temperature sensing techniques. Use of the current UAS platform is limited to single pools and stream reaches in which groundwater discharge is at least 1% of main stem flow and enters the stream from discrete seeps or seepage faces located near the stream surface. Previous studies (Dugdale et al., 2015; Hare et al., 2015) and the modeling study in Chapter 6 have shown TIR to

be an effective approach to detect stream surface temperature anomalies, but its use with a small, unmanned aerial platform significantly decreases its measurement accuracy. To improve accuracy and collect data that represent significant temperature measurements, UAS-specific TIR cameras with higher sensor resolutions on-board larger platforms with increased maximum payload are recommended. The small UAS-TIR platform should then be flown to both minimize sun glints and camera reflections in the TIR data: Flights should be oriented in the opposite direction of the sun with the camera at a pre-tested, optimal camera angle.

The pressure-temperature sensor system on-board the UAS may serve as a more valuable tool for field researchers; the immersible sensor truly becomes advantageous when high reflectance of the stream on hot summer days at the peak of the dry season causes significant inaccuracies in TIR measurements. However, to widen the range of pool sizes in which this platform can collect temperature data when flying in GPS-guided mode, which relies on GPS and waypoints for positioning, improvements to GPS positioning must be made. Updating the on-board GPS to improve the platform's horizontal positional accuracy, whether with an additional reference GPS unit or real-time kinematic unit, allows resolution of fine-scale thermal structures in larger and deeper pools with shorter mixing length scales. Improved geo-location through positional accuracy also reduces researchers' dependence on manual flights and relieves operator exhaustion, currently an unavoidable result of the UAS platform's application in stream temperature sensing.

Lastly, several unavoidable pitfalls surrounding UAS use and performance must be recognized. Environmental conditions such as high flow velocities and wind speeds result in uncertainty in the sensor location and continuous positional adjustment by the operator. The platform must also be flown to evade riparian vegetation and rocks, which may cause the sensor to miss riparian phenomena such as cold-water zones pinned to banks. In addition to system and operational challenges, field researchers using UASs face a complex and dynamic regulatory landscape. Currently, environmental sensing with UASs in low-risk and low-population areas remains enmeshed in rules and regulations that hamper usefulness and feasibility. These challenges are certainly not present when using more traditional stream temperature sensing methods. However, with steady improvements to system constraints, small UAS characterization of potential groundwater-fed thermal refugia may become an increasingly attractive approach that reduces field equipment costs and workload and allows researchers to collect fine-scale stream temperature data in distributed stream networks.

	Current	As technology improves	Not feasible
Spatial scale	Reach	Basin	Basin with overhanging riparian vegetation
Location	Previously identified cold inflow areas	Along-stream to identify cold inflow areas	
Stream depth	Shallow	Deeper	

Table 7.1: Summary of current and future UAS temperature sensing feasibilities.

As the importance of both fog and groundwater-fed thermal refugia in coastal watersheds is only likely to increase with climate change and increasing water demands, the methods presented in this dissertation can aid field researchers in collecting watershed data key to understanding the ecosystem's current health as well as future vulnerability.

Bibliography

Achtelik, M., Doth, K., Gurdan, D., and Stumpf, J. (2012). Design of a Multi Rotor MAV with regard to Efficiency, Dynamics and Redundancy. In AIAA Guidance, Navigation, and Control Conference, pages 1–17. AIAA.

Adams, H. D., Guardiola-Claramonte, M., Barron-Gafford, G. A., Villegas, J. C., Breshears, D. D., Zou, C. B., Troch, P. A., and Huxman, T. E. (2009). Temperature sensitivity of drought-induced tree mortality portends increased regional die-off under global-change-type drought. Proceedings of the national academy of sciences, 106(17):7063–7066.

Akob, D. (2015). Personal communication.

Alabaster, J. S. and Lloyd, R. S. (2013). Water quality criteria for freshwater fish. Elsevier, London, UK.

Allen, C. D., Macalady, A. K., Chenchouni, H., Bachelet, D., McDowell, N., Vennetier, M., Kitzberger, T., Rigling, A., Breshears, D. D., Hogg, E. T., et al. (2010). A global overview of drought and heat-induced tree mortality reveals emerging climate change risks for forests. Forest ecology and management, 259(4):660–684.

Anderson, M. (2005). Tending the wild. University of California Press.

Arnell, N. W. (1999). The effect of climate change on hydrological regimes in Europe: a continental perspective. Global environmental change, 9(1):5–23.

Azevedo, J. and Morgan, D. (1974). Fog precipitation in coastal California forests. Ecology, 55:1135–1141.

Bacchi, B. and Kottegoda, N. T. (1995). Identification and calibration of spatial correlation patterns of rainfall. Journal of Hydrology, 165:311–348.

Balcombe, S. R., Sheldon, F., Capon, S. J., Bond, N. R., Hadwen, W. L., Marsh, N., and Bernays, S. J. (2011). Climate-change threats to native fish in degraded rivers and floodplains of the Murray–Darling Basin, Australia. Marine and Freshwater Research, 62(9):1099–1114.

Banks, W. S., Paylor, R. L., and Hughes, W. B. (1996). Using thermal-infrared imagery to delineate ground-water discharge. Groundwater, 34(3):434–443.

Baxter, C., Hauer, F., and Woessner, W. (2003). Measuring groundwater-stream water exchange: new techniques for installing minipiezometers and estimating hydraulic conductivity. Transactions of the American Fisheries Society, 132:493–502.

Beer, W. N. and Anderson, J. J. (2001). Effect of spawning day and temperature on salmon emergence: interpretations of a growth model for Methow River Chinook. Canadian Journal of Fisheries and Aquatic Sciences, 58(5):943–949.

Beguería, S., López-Moreno, J. I., Lorente, A., Seeger, M., and García-Ruiz, J. M. (2003). Assessing the effect of climate oscillations and land-use changes on streamflow in the Central Spanish Pyrenees. AMBIO: A Journal of the Human Environment, 32(4):283–286.

Beletsky, D. and Schwab, D. J. (2001). Modeling circulation and thermal structure in Lake Michigan: Annual cycle and interannual variability. Journal of Geophysical Research: Oceans, 106(C9):19745–19771.

Bernardo, J. M., Ilhéu, M., Matono, P., and Costa, A. M. (2003). Interannual variation of fish assemblage structure in a mediterranean river: implications of streamflow on the dominance of native or exotic species. River Research and Applications, 19(5-6):521–532.

Bjornn, T. and Reiser, D. (1991). Habitat requirements of salmonids in streams. American Fisheries Society Special Publication, 19(837):138.

Blaustein, A. and Wake, D. (1990). Declining amphibian populations — a global phenomenon. Trends in Ecology Evolution, 5:203–204.

Booker, D. J., Sear, D. A., and Payne, A. J. (2001). Modelling three-dimensional flow structures and patterns of boundary shear stress in a natural pool-riffle sequence. Earth Surface Processes and Landforms, 26(5):553–576.

Bowler, D., Mant, R., Orr, H., Hannah, D., and Pullin, A. (2012). What are the effects of wooded riparian zones on stream temperature? Environmental Evidence, 1:1–9.

Breazeale, E., McGeorge, W., and Breazeale, J. (1950). Moisture absorption by plants from an atmosphere of high humidity. Plant Physiology, 25:413–419.

Briggs, M. A., Voytek, E. B., Day-Lewis, F. D., Rosenberry, D. O., and Lane, J. W. (2013). Understanding water column and streambed thermal refugia for endangered mussels in the Delaware River. Environmental science & technology, 47(20):11423–11431.

Brooks, J. R., Barnard, H. R., Coulombe, R., and McDonnell, J. J. (2010). Ecohydrologic separation of water between trees and streams in a Mediterranean climate. Nature Geoscience, 3:100–104.

Brunke, M. and Gonser, T. (1997). The ecological significance of exchange processes between rivers and groundwater. Freshwater Biology, 37(1):1–33.

Buck, C. and Null, S. (2013). Modeling insights from distributed temperature sensing data. Hydrology and Earth System Sciences Discussions, 10(8):9999–10034.

Burgess, S. and Dawson, T. (2004). The contribution of fog to the water relations of Sequoia sempervirens (D. Don): foliar uptake and prevention of dehydration. Plant, Cell and Environment, 27:1023–1034.

Caissie, D. (2006). The thermal regime of rivers: a review. Freshwater Biology, 51(8):1389–1406.

Carpenter, S. (2005). Eutrophication of aquatic ecosystems: bistability and soil phosphorus. PNAS, 102(29):10002–10005.

Carpenter, S., Ludwig, D., and Brock, W. (1999). Management of eutrophication for lakes subject to potentially irreversible change. Ecological Applications, 9(3):751–771.

Chestnut, T., Anderson, C., Popa, R., Blaustein, A., Voytek, M., Olson, D., and Kirshtein, J. (2014). Heterogeneous occupancy and density estimates of the pathogenic fungus Batrachochytrium dendrobatidis in waters of North America. PLoS ONE, 9(9).

Chung, M., Detweiler, C., Hamilton, M., Higgins, J., Ore, J., and Thompson, S. (2015). Obtaining the thermal structure of lakes from the air. Water, 7(11):6467–6482.

Chung, M., Dufour, A., Pluche, R., and Thompson, S. (2017). How much does dry-season fog matter? Quantifying fog contributions to water balance in a coastal California watershed. Hydrological Processes, 31(22):3948–3961. hyp.11312.

Cobos, D. R. (2013). Predicting the amount of water on the surface of the LWS dielectric leaf wetness sensor. Decagon Devices, Inc.

Combs, B. D. (1965). Effect of temperature on the development of salmon eggs. The Progressive Fish-Culturist, 27(3):134–137.

Constantz, J. (1998). Interaction between stream temperature, streamflow, and groundwater exchanges in alpine streams. Water Resources Research, 34(7):1609–1615.

Constantz, J. (2008). Heat as a tracer to determine streambed water exchanges. Water Resources Research, 44:1–20.

Cox, T. J. and Rutherford, J. C. (2000). Predicting the effects of time-varying temperatures on stream invertebrate mortality. New Zealand Journal of Marine and Freshwater Research, 34(2):209–215.

Crook, D. and Robertson, A. (1999). Relationships between riverine fish and woody debris: implications for lowland rivers. Marine and Freshwater Research, 50(8):941–953.

Dahm, C., Valett, H., Baxter, C., and Woessner, W. (2006). Hyporheic zones. In Hauer, F. and Lamberti, G., editors, Methods in stream ecology. 2nd ed., pages 119–142. Academic Press, San Diego, CA.

Dale, M. R. and Fortin, M.-J. (2014). Spatial analysis: a guide for ecologists. Cambridge University Press.

Daufresne, M., Bady, P., and Fruget, J.-F. (2007). Impacts of global changes and extreme hydroclimatic events on macroinvertebrate community structures in the French Rhône River. Oecologia, 151(3):544–559.

Daufresne, M. and Boet, P. (2007). Climate change impacts on structure and diversity of fish communities in rivers. Global Change Biology, 13(12):2467–2478.

Dawson, T. (1996). The use of fog precipitation by plants in coastal redwood forests. In Conference on coastal redwood forest ecology and management, Humboldt State University, pages 90–93.

Dawson, T. (1998). Fog in the California redwood forest: ecosystem inputs and use by plants. Oecologia, 117:476–485.

Deitchman, R. S. and Loheide, S. P. (2009). Ground-based thermal imaging of groundwater flow processes at the seepage face. Geophysical Research Letters, 36(14).

DeMario, A., Lopez, P., Plewka, E., Wix, R., Xia, H., Zamora, E., Gessler, D., and Yalin, A. P. (2017). Water plume temperature measurements by an Unmanned Aerial System (UAS). Sensors, 17(2):306.

Dominguez, F., Rivera, E., Lettenmaier, D., and Castro, C. (2012). Changes in winter precipitation extremes for the western United States under a warmer climate as simulated by regional climate models. Geophysical Research Letters, 39(5).

Dugdale, S. J., Bergeron, N. E., and St-Hilaire, A. (2015). Spatial distribution of thermal refuges analysed in relation to riverscape hydromorphology using airborne thermal infrared imagery. Remote Sensing of Environment, 160:43–55.

Dunbabin, M., Grinham, A., and Udy, J. (2009). An autonomous surface vehicle for water quality monitoring. In Australasian Conference on Robotics and Automation, pages 2–4. ACRA.

Dunbabin, M. and Marques, L. (2012). Robots for environmental monitoring: Significant advancements and applications. Robotics and Automation Magazine, IEEE, 19(1):24–39.

Eaton, J. G. and Scheller, R. M. (1996). Effects of climate warming on fish thermal habitat in streams of the United States. Limnology and oceanography, 41(5):1109–1115.

Ebersole, J. L., Liss, W. J., and Frissell, C. A. (2001). Relationship between stream temperature, thermal refugia and rainbow trout Oncorhynchus mykiss abundance in arid-land streams in the northwestern United States. Ecology of Freshwater Fish, 10(1):1–10.

Ebersole, J. L., Liss, W. J., and Frissell, C. A. (2003). Cold water patches in warm streams: physicochemical characteristics and the influence of shading. JAWRA Journal of the American Water Resources Association, 39(2):355–368.

Ebersole, J. L., Wigington, Jr, P. J., Leibowitz, S. G., Comeleo, R. L., and Van Sickle, J. (2015). Predicting the occurrence of cold-water patches at intermittent and ephemeral tributary confluences with warm rivers. Freshwater Science, 34:111–124.

Elliott, J. (1975). The growth rate of brown trout (Salmo trutta L.) fed on maximum rations. The Journal of Animal Ecology, pages 805–821.

Elliott, J. and Hurley, M. (1997). A functional model for maximum growth of Atlantic salmon parr, Salmo salar, from two populations in northwest England. Functional Ecology, 11(5):592–603.

Elliott, J., Hurley, M. A., and Maberly, S. (2000). The emergence period of sea trout fry in a Lake District stream correlates with the North Atlantic Oscillation. Journal of Fish Biology, 56(1):208–210.

Ewing, H., Weathers, K., Templer, P., Dawson, T., Firestone, M., Elliott, A., and Boukili, V. (2009). Fog water and ecosystem function: heterogeneity in a California redwood forest. Ecosystems, 12:417–433.

Fatichi, S., Ivanov, V. Y., and Caporali, E. (2012). Investigating interannual variability of precipitation at the global scale: Is there a connection with seasonality? Journal of climate, 25(16):5512–5523.

Fellers, G., Cole, R., Reinitz, D., and Kleeman, P. (2011). Amphibian chytrid fungus (Batrachochytrium dendrobatidis) in coastal and montane California, USA anurans. Herpetological Conservation and Biology, 6(3):383–394.

Feng, X., Vico, G., and Porporato, A. (2012). On the effects of seasonality on soil water balance and plant growth. Water Resources Research, 48(5).

Fischer, D., Still, C., and Williams, A. (2009). Significance of summer fog and overcast for drought stress and ecological functioning of coastal California endemic plant species. Journal of Biogeography, 36:783–799.

Fischer, D. T. and Still, C. J. (2007). Evaluating patterns of fog water deposition and isotopic composition on the California Channel Islands. Water Resources Research, 43.

Fischer, H. B., List, J. E., Koh, C. R., Imberger, J., and Brooks, N. H. (1979). Mixing in Inland and Coastal Waters. Elsevier.

Fisher, R. and Shaffer, H. (1996). The decline of amphibians in California's Great Central Valley. Conservation Biology, 10:1387–1397.

FLIR Systems (2016). UAS Radiometry. FLIR Systems.

Garnier, B. and Lanzetta, F. (2011). Tutorial 4: In situ realization/characterization of temperature/heat flux sensors. Technical report, Université de Nantes.

Garreaud, R., Barichivich, J., Christie, D. A., and Maldonado, A. (2008). Interannual variability of the coastal fog at Fray Jorge relict forests in semiarid Chile. Journal of Geophysical Research: Biogeosciences, 113.

Genkai-Kato, M. and Carpenter, S. R. (2005). Eutrophication due to phosphorus recycling in relation to lake morphometry, temperature, and macrophytes. Ecology, 86(1):210–219.

Gerecht, K. E., Cardenas, M. B., Guswa, A. J., Sawyer, A. H., Nowinski, J. D., and Swanson, T. E. (2011). Dynamics of hyporheic flow and heat transport across a bed-to-bank continuum in a large regulated river. Water Resources Research, 47(3):n/a–n/a. W03524.

Gooseff, M. N., Strzepek, K., and Chapra, S. C. (2005). Modeling the potential effects of climate change on water temperature downstream of a shallow reservoir, Lower Madison River, MT. Climatic Change, 68(3):331–353.

Haines, F. (1952). The absorption of water by leaves in an atmosphere of high humidity. Journal of Experimental Botany, 3:95–98.

Haines, F. (1953). The absorption of water by leaves in fogged air. Journal of Experimental Botany, 4:106–107.

Handcock, R., Gillespie, A., Cherkauer, K., Kay, J., Burges, S., and Kampf, S. (2006). Accuracy and uncertainty of thermal-infrared remote sensing of stream temperatures at multiple spatial scales. Remote Sensing of Environment, 100(4):427–440.

Hardin, P. J. and Jensen, R. R. (2011). Small-scale unmanned aerial vehicles in environmental remote sensing: Challenges and opportunities. GIScience and Remote Sensing, 48(1):99–111.

Hare, D. K., Briggs, M. A., Rosenberry, D. O., Boutt, D. F., and Lane, J. W. (2015). A comparison of thermal infrared to fiber-optic distributed temperature sensing for evaluation of groundwater discharge to surface water. Journal of Hydrology, 530:153–166.

Harr, R. (1980). Streamflow after patch logging in small drainages within the Bull Run Municipal watershed, Oregon. USDA Forest Service Research Paper, PNW-268.

Harr, R. (1982). Fog drip in the Bull Run Municipal Watershed, Oregon. Water Resources Bulletin, 18:785–789.

Hawkins, C. P., Hogue, J. N., Decker, L. M., and Feminella, J. W. (1997). Channel morphology, water temperature, and assemblage structure of stream insects. Journal of the North American Benthological Society, 16(4):728–749.

Hiatt, C., Fernandez, D., and Potter, C. (2012). Measurements of fog water deposition on the California Central Coast. Atmospheric and Climate Sciences, 2:525–531.

Hof, C., Araujo, M., Jetz, W., and Rahbek, C. (2011). Additive threats from pathogens, climate and land-use change for global amphibian diversity. Nature, 480(7378):516–519.

Holtby, L. B. (1988). Effects of logging on stream temperatures in Carnation Creek, British Columbia, and associated impacts on the coho salmon (Oncorhynchus kisutch). Canadian Journal of Fisheries and Aquatic Sciences, 45(3):502–515.

Horsch, G. and Stefan, H. (1988). Convective circulation in littoral water due to surface cooling. Limnology and Oceanography, 33(5):1068–1083.

Hutley, L., Doley, D., Yates, D., and Boonsaner, A. (1997). Water balance of an Australian subtropical rainforest at altitude: the ecological and physiological significance of intercepted cloud and fog. Australian Journal of Botany, 45:311–329.

Huver, J., Koprivnikar, J., Johnson, P., and Whyard, S. (2015). Development and application of an eDNA method to detect and quantify a pathogenic parasite in aquatic ecosystems. Ecological Applications, 25:991–1002.

Hyatt, A., Boyle, D., Olsen, V., Boyle, D., Berger, L., Obendorf, D., Dalton, A., Kriger, K., Hero, M., Hines, H., Phillott, R., Campbell, R., Marantelli, G., Gelason, F., and Colling, A. (2007). Diagnostic assays and sampling protocols for the detection of Batrachochytrium dendrobatidis. Disease of Aquatic Organisms, 73(3):172–192.

Ingraham, N. and Matthews, R. (1988). Fog drip as a source of groundwater recharge in northern Kenya. Water Resources Research, 24:1406–1410.

Ingraham, N. and Matthews, R. (1995). The importance of fog-drip water to vegetation: Point Reyes Peninsula, California. Journal of Hydrology, 164:269–285.

Ingwersen, J. (1985). Fog drip, water yield, and timber harvesting in the Bull Run Municipal Watershed, Oregon. Water Resources Bulletin, 21:469–473.

International Union for Conservation of Nature and Natural Resources (2015). IUCN Red List Status. Online.

Jankowski, T., Livingstone, D. M., Buhrer, H., Forster, R., and Niederhauser, P. (2006). Consequences of the 2003 European heat wave for lake temperature profiles, thermal stability, and hypolimnetic oxygen depletion: Implications for a warmer world. Limnology and Oceanography, 51(2):815–819.

Jensen, A., Hvidsten, N., and Johnsen, B. (1998). Effects of temperature and flow on the upstream migration of adult Atlantic salmon in two Norwegian Rivers. Fish Migration and Fish Bypasses, page 45.

Jensen, A. M., Neilson, B. T., McKee, M., and Chen, Y. (2012). Thermal remote sensing with an autonomous unmanned aerial remote sensing platform for surface stream temperatures. In 2012 IEEE International Geoscience and Remote Sensing Symposium, pages 5049–5052. IEEE.

Joffre, R., Rambal, S., and Damesin, C. (1999). Functional attributes in Mediterranean-type ecosystems. Handbook of functional plant ecology, pages 347–380.

Johnson, P. and Chase, J. (2004). Parasites in the food web: linking amphibian malformations and aquatic eutrophication. Ecology Letters, 7(7):521–526.

Johnson, P., Chase, J., Dosch, K., Hartson, R., Gross, J., Larson, D., Sutherland, D., and Carpenter, S. (2007). Aquatic eutrophication promotes pathogenic infection in amphibians. PNAS, 104(40):15781–15786.

Johnstone, J. and Dawson, T. (2010). Climatic context and ecological implications of summer fog decline in the coast redwood region. Proceedings of the National Academy of Sciences, 107:4533–4538.

Juvik, J. O. and Nullet, D. (1995). Comments on "A proposed standard fog collector for use in high-elevation regions". Journal of Applied Meteorology, 34(9):2108–2110.

Kay, J. E., Kampf, S. K., Handcock, R. N., Cherkauer, K. A., Gillespie, A. R., and Burges, S. J. (2005). Accuracy of lake and stream temperatures estimated from thermal infrared images. Journal of the American Water Resources Association, 41(5):1161–1175.

Kennedy, V., Kendall, C., Zellweger, G., Wyerman, T., and Avanzino, R. (1986). Determination of the components of stormflow using water chemistry and environmental isotopes, Mattole River basin, California. Journal of Hydrology, 84:107–140.

Keppeler, E. (2007). Effects of timber harvest on fog drip and streamflow, Caspar Creek Experimental Watersheds, Mendocino County, California. In Redwood Science Symposium: What does the future hold?, pages 85–93.

Kirshtein, J., Anderson, C., Wood, J., Longcore, J., and Voytek, M. (2007). Quantitative PCR detection of Batrachochytrium dendrobatidis DNA from sediments and water. Diseases of aquatic organisms, 77(1):11–15.

Knapp, R., Boiano, D., and Vredenburg, V. (2007). Removal of nonnative fish results in population expansion of a declining amphibian (mountain yellow-legged frog, Rana muscosa). Biological Conservation, 135(1):11–20.

Komatsu, E., Fukushima, T., and Harasawa, H. (2007). A modeling approach to forecast the effect of long-term climate change on lake water quality. Ecological Modelling, 209(2):351–366.

Koohafkan, M., Thompson, S. E., and Dawson, T. E. (2014, unpublished material). Can dielectric leaf wetness sensors be used to quantify surface water storage on leaves of Californian tree species?

Kurylyk, B. L., MacQuarrie, K. T., Linnansaari, T., Cunjak, R. A., and Curry, R. A. (2015). Preserving, augmenting, and creating cold-water thermal refugia in rivers: concepts derived from research on the miramichi river, new brunswick (canada). Ecohydrology, 8(6):1095–1108.

Laval, B., Bird, J. S., and Helland, P. D. (2000). An autonomous underwater vehicle for the study of small lakes. Journal of Atmospheric and Oceanic Technology, 17(1):69–76.

Leipper, D. (1995). Fog forecasting objectively in the California coastal area using LIBS. Weather Forecast, 10:741–762.

Lewis, Q. W. and Rhoads, B. L. (2015a). Rates and patterns of thermal mixing at a small stream confluence under variable incoming flow conditions. Hydrological Processes, 29(20):4442–4456.

Lewis, Q. W. and Rhoads, B. L. (2015b). Rates and patterns of thermal mixing at a small stream confluence under variable incoming flow conditions. Hydrological Processes, 29(20):4442–4456.

Longo, A., Rodriguze, D., da Silva Leite, D., Toledo, L., Mendoza Almeralla, C., Burrowes, P., and Zamudio, K. (2013). ITS1 Copy Number Varies among Batrachochytrium dendrobatidis strains: Implications for qPCR estimates of infection intensity from field-collected amphibian skin swabs. PLoS ONE, 8(3).

MacWilliams, M. L., Wheaton, J. M., Pasternack, G. B., Street, R. L., and Kitanidis, P. K. (2006). Flow convergence routing hypothesis for pool-riffle maintenance in alluvial rivers. Water Resources Research, 42(10):n/a–n/a. W10427.

Markarian, R. K. (1980). A study of the relationship between aquatic insect growth and water temperature in a small stream. Hydrobiologia, 75(1):81–95.

Marouchos, A., Muir, B., Babcock, R., and Dunbabin, M. (2015). A shallow water AUV for benthic and water column observations. In OCEANS 2015 — Genova, pages 1–7. IEEE.

Matthews, K. R. and Berg, N. H. (1997). Rainbow trout responses to water temperature and dissolved oxygen stress in two southern California stream pools. Journal of Fish Biology, 50(1):50–67.

Matthews, K. R., Berg, N. H., Azuma, D. L., and Lambert, T. R. (1994). Cool water formation and trout habitat use in a deep pool in the Sierra Nevada, California. Transactions of the American Fisheries Society, 123(4):549–564.

Michael, C. and John, F. (1994). The radiatively driven natural convection beneath a floating plant layer. Limnology and Oceanography, 39(5):1186–1194.

Mohseni, O., Stefan, H. G., and Eaton, J. G. (2003). Global warming and potential changes in fish habitat in US streams. Climatic change, 59(3):389–409.

Monk, W. A., Wilbur, N. M., Curry, R. A., Gagnon, R., and Faux, R. N. (2013). Linking landscape variables to cold water refugia in rivers. Journal of environmental management, 118:170–176.

Montgomery, D. R. and Buffington, J. M. (1997). Channel-reach morphology in mountain drainage basins. Geological Society of America Bulletin, 109(5):596–611.

Mooji, W. M., Hulsmann, S., De Senerpont Domis, L. N., Nolet, B. A., Bodelier, P. L. E., Boers, P. C. M., M., D. P. L., Gons, H. J., Ibelines, B. W., Noordhuis, R., Portielje, R., Wolfstein, K., and Lammens, E. H. R. R. (2005). The impact of climate change on lakes in the Netherlands: a review. Aquatic Ecology, 39:381–400.

Mooney, H. and Zavaleta, E. (2016). Ecosystems of California. Univ of California Press.

Moore, R. D., Spittlehouse, D. L., and Story, A. (2005). Riparian microclimate and stream temperature response to forest harvesting: a review. Journal of the American Water Resource Association, 41(4):813–834.

Moran, P. A. P. (1950). Notes on continuous stochastic phenomena. Biometrika, 37(1/2):17–23.

Morrongiello, J. R., Beatty, S. J., Bennett, J. C., Crook, D. A., Ikedife, D. N., Kennard, M. J., Kerezsy, A., Lintermans, M., McNeil, D. G., Pusey, B. J., et al. (2011). Climate change and its implications for Australias freshwater fish. Marine and Freshwater Research, 62(9):1082–1098.

Mulero-Pázmány, M., Stolper, R., Van Essen, L., Negro, J. J., and Sassen, T. (2014). Remotely piloted aircraft systems as a rhinoceros anti-poaching tool in Africa. PLoS ONE, 9(1).

Nijssen, B., O'Donnell, G. M., Hamlet, A. F., and Lettenmaier, D. P. (2001). Hydrologic sensitivity of global rivers to climate change. Climatic change, 50(1-2):143–175.

NOAA Office of Satellite and Product Operations (2015). Operational SST Anomaly Charts for 2016. `http://www.ospo.noaa.gov/Products/ocean/sst/anomaly`.

Oberlander, G. (1956). Summer fog precipitation on the San Francisco peninsula. Ecology, 37:851–852.

Oldham, C. E. and Sturman, J. J. (2001). The effect of emergent vegetation on convective flushing in shallow wetlands: Scaling and experiments. Limnology and Oceanography, 46(6):1486–1493.

Ore, J.-P. and Detweiler, C. (2018). Sensing water properties at precise depths from the air. In Field and Service Robotics, pages 205–220. Springer.

Ore, J.-P., Elbaum, S., Burgin, A., and Detweiler, C. (2015). Autonomous aerial water sampling. Journal of Field Robotics.

Oshun, J., Dietrich, W. E., Dawson, T. E., and Fung, I. (2016). Dynamic, structured heterogeneity of water isotopes inside hillslopes. Water Resources Research, 52:164–189.

Peace, R. J. (1969). Heavy-fog regions in the conterminous United States. Monthly Weather Review, 97:116–123.

Pilgrim, J. M., Fang, X., and Stefan, H. G. (1998). Stream temperature correlations with air temperatures in Minnesota: implications for climate warming. JAWRA Journal of the American Water Resources Association, 34(5):1109–1121.

Potter, C. (2016). Measurements of fog water interception by shrubs on the California central coast. Journal of Coastal Conservation, pages 1–11.

Power, M. E., Bouma-Gregson, K., Higgins, P., and Carlson, S. M. (2015). The thirsty Eel: summer and winter flow thresholds that tilt the Eel River of northwestern California from salmon-supporting to cyanobacterially degraded states. Copeia, 103(1):200–211.

Prada, S. and da Silva, M. (2001). Fog precipitation on the Island of Madeira (Portugal). Environmental Geology, 41:384–389.

Priestley, C. and Taylor, R. (1972). On the assessment of surface heat flux and evaporation using large scale parameters. Monthly Weather Review, 100:81–92.

Reinitz, D., Yoshino, T., and Cole, R. (2007). A Ribeiroia spp. (Class: Trematoda) — specific PCR-based diagnostic. Journal of Parasitology, 93(5):1234–1238.

Rhoads, B. L. and Kenworthy, S. T. (1995). Flow structure at an asymmetrical stream confluence. Geomorphology, 11(4):273–293.

Rhoads, B. L. and Kenworthy, S. T. (1998). Time-averaged flow structure in the central region of a stream confluence. Earth Surface Processes and Landforms, 23(2):171–191.

Rice, S. P., Kiffney, P., Greene, C., and Pess, G. R. (2008). The ecological importance of tributaries and confluences. In Rice, S., Roy, A., and Rhoads, B., editors, River confluences, tributaries and the fluvial network. John Wiley & Sons, Chichester, UK.

Rinke, K., Huber, A. M. R., Kempke, S., Eder, M., Wolf, T., Probst, W. N., and Rothhaupta, K.-O. (2009). Lake-wide distributions of temperature, phytoplankton, zooplankton, and fish in the pelagic zone of a large lake. Limnology and Oceanography, 54(4):1306–1322.

Rodriguez, J. F., Garcia, C. M., and Garcia, M. H. (2013). Three-dimensional flow in centered pool-riffle sequences. Water Resources Research, 49(1):202–215.

Romero, J. R. and Kling, G. W. (2002). Spatial-temporal variability in surface layer deepening and lateral advection in an embayment of Lake Victoria, East Africa. Limnology and Oceanography, 47(3):656–671.

Ruesch, A. S., Torgersen, C. E., Lawler, J. J., Olden, J. D., Peterson, E. E., Volk, C. J., and Lawrence, D. J. (2012). Projected climate-induced habitat loss for salmonids in the John Day River network, Oregon, USA. Conservation Biology, 26(5):873–882.

Salve, R., Rempe, D. M., and Dietrich, W. E. (2012). Rain, rock moisture dynamics, and the rapid response of perched groundwater in weathered, fractured argillite underlying a steep hillslope. Water Resources Research, 48(11):n/a–n/a. W11528.

Sawaske, S. and Freyberg, D. (2015). Fog, fog drip, and streamflow in the Santa Cruz Mountains of the California Coast Range. Ecohydrology, 8:695–713.

Scheffer, M. and Carpenter, S. (2003). Catastrophic regime shifts in ecosystems: linking theory to observation. Trends in Ecology Evolution, 18(12):648–656.

Scheffer, M., Carpenter, S., Foley, J., Folke, C., and Walker, B. (2001). Catastrophic shifts in ecosystems. Nature, 413(6856):591–596.

Schemenauer, R. and Cereceda, P. (1991). Fog-water collection in arid coastal locations. Ambio, 20:303–308.

Schmugge, T. J., Kustas, W. P., Ritchie, J. C., Jackson, T. J., and Rango, A. (2002). Remote sensing in hydrology. Advances in Water Resources, 25:1367–1385.

Scholl, M., Gingerich, S., and Tribble, G. (2002). The influence of microclimates and fog on stable isotope signatures used in interpretation of regional hydrology: East Maui, Hawaii. Journal of Hydrology, 264:170–184.

Selker, J., Thevenaz, L., Huwald, H., Mallet, A., Luxemburg, W., van de Giesen, N., Stejskal, M., Zeman, J., Westhoff, M., and Parlange, M. (2006). Distributed fiber-optic temperature sensing for hydrologic systems. Water Resources Research, 42:1–8.

Shuttleworth, W. (1977). The exchange of wind-driven fog and mist between vegetation and the atmosphere. Boundary-Layer Meteorology, 12:463–489.

Sinokrot, B. and Gulliver, J. (2000). In-stream flow impact on river water temperatures. Journal of Hydraulic Research, 38(5):339–349.

Sinokrot, B., Stefan, H., McCormick, J., and Eaton, J. (1995). Modeling of climate change effects on stream temperatures and fish habitats below dams and near groundwater inputs. Climatic Change, 30(2):181–200.

Sparrow, F. (1968). Ecology of freshwater fungi, volume 3, pages 41–53. Academic Press, New York.

Sutton, R. J., Deas, M. L., Tanaka, S. K., Soto, T., and Corum, R. A. (2007). Salmonid observations at a Klamath River thermal refuge under various hydrological and meteorological conditions. River Research and Applications, 23(7):775–785.

Sutton, R. J. and Soto, T. (2012). Juvenile coho salmon behavioural characteristics in Klamath river summer thermal refugia. River Research and Applications, 28(3):338–346.

Templer, P. H., Weathers, K. C., Ewing, H. A., Dawson, T. E., Mambelli, S., Lindsey, A. M., Webb, J., Boukili, V. K., and Firestone, M. K. (2015). Fog as a source of nitrogen for redwood trees: evidence from fluxes and stable isotopes. Journal of Ecology, 103(6):1397–1407.

Todd, C. R., Ryan, T., Nicol, S. J., and Bearlin, A. R. (2005). The impact of cold water releases on the critical period of post-spawning survival and its implications for Murray cod (Maccullochella peelii peelii): a case study of the Mitta Mitta River, southeastern Australia. River Research and Applications, 21(9):1035–1052.

Tonolla, D., Acuna, V., Uehlinger, U., Frank, T., and Tockner, K. (2010). Thermal heterogeneity in river floodplains. Ecosystems, 13(5):727–740.

Torgersen, C. E., Faux, R., McIntosh, B., Poage, N., and Norton, D. (2001). Airborne thermal remote sensing for water temperature assessment in rivers and streams. Remote Sensing of Environment, 76:386–398.

Torgersen, C. E., Price, D. M., Li, H. W., and McIntosh, B. A. (1999a). Multiscale thermal refugia and stream habitat associations of chinook salmon in northeastern Oregon. Ecological Applications, 9(1):301–319.

Torgersen, C. E., Price, D. M., Li, H. W., and McIntosh, B. A. (1999b). Multiscale thermal refugia and stream habitat associations of chinook salmon in northeastern Oregon. Ecological Applications, 9(1):301–319.

Torgerson, C. E., Faux, R. N., McIntosh, B. A., Poage, N. J., and Norton, D. J. (2001). Airborne thermal remote sensing for water temperature assessment in rivers and streams. Remote Sensing of Environment, 76:386–398.

Trauth, N., Schmidt, C., Maier, U., Vieweg, M., and Fleckenstein, J. (2013). Coupled 3-D stream flow and hyporheic flow model under varying stream and ambient groundwater flow conditions in a pool-riffle system. Water Resources Research, 49(9):5834–5850.

Tu, J. (2009). Combined impact of climate and land use changes on streamflow and water quality in eastern Massachusetts, USA. Journal of Hydrology, 379(3):268–283.

Tyler, S. W., Selker, J. S., Hausner, M. B., Hatch, C. E., Torgerson, T., Thodal, C. E., and Schladow, S. G. (2009). Environmental temperature sensing using Raman spectra DTS fiber-optic methods. Water Resources Research, 45(4):1–11.

USGS (2007). USGS ARMI Backcountry Chytrid-water Field Protocol. Technical report, USGS Amphibian Research and Monitoring Initiative.

van Vliet, M. T., Franssen, W. H., Yearsley, J. R., Ludwig, F., Haddeland, I., Lettenmaier, D. P., and Kabat, P. (2013). Global river discharge and water temperature under climate change. Global Environmental Change, 23(2):450 – 464.

van Vliet, M. T., Ludwig, F., Zwolsman, J., Weedon, G., and Kabat, P. (2011). Global river temperatures and sensitivity to atmospheric warming and changes in river flow. Water Resources Research, 47(2).

Vannote, R. L. and Sweeney, B. W. (1980). Geographic analysis of thermal equilibria: a conceptual model for evaluating the effect of natural and modified thermal regimes on aquatic insect communities. The American Naturalist, 115(5):667–695.

Vico, G. and Porporato, A. (2010). Traditional and microirrigation with stochastic soil moisture. Water resources research, 46(3).

Vincent, J. B., Werden, L. K., and Ditmer, M. A. (2015). Barriers to adding UAVs to the ecologist's toolbox: Peer-reviewed letter. Frontiers in Ecology and the Environment, 13(2):74–75.

Vogl, R. (1973). Ecology of knobcone pine in the Santa Ana Mountains, California. Ecological Monographs, 43:125–143.

WAAS TE Team (2017). Global Positioning System (GPS) Standard Positioning Service (SPS) Performance Analysis Report. Technical report, William J. Hughes Technical Center.

Wang, L., Kaseke, K. F., and Seely, M. K. (2017). Effects of non-rainfall water inputs on ecosystem functions. Wiley Interdisciplinary Reviews: Water, 4(1):e1179–n/a. e1179.

Wang, T., Kelson, S., Greer, G., Thompson, S., Nussle, S., and Carlson, S. (In prep). Tributary confluences as thermal refuge in a warming river network.

Wang, W., Anderson, B., Phillips, N., Kaufmann, R., Potter, C., and Myneni, R. (2006). Feedbacks of vegetation on summertime climate variability over the North American Grasslands. Part I: statistical analysis. Earth Interactions, 10:1–27.

Ward, J. V. and Stanford, J. A. (1992). Thermal responses in the evolutionary ecology of aquatic insects. Annual Review of Entomology, 27:97–117.

Weathers, K., Lovett, G., and Likens, G. (1995). Cloud deposition to a spruce forest edge. Atmospheric Environment, 29:665–672.

Weathers, K., Lovett, G., Likens, G., and Caraco, N. (2000). Cloudwater inputs of nitrogen to forest ecosystems in southern Chile: forms, fluxes, and sources. Ecosystems, 3:590–595.

Weathers, K. C., Simkin, S. M., Lovett, G. M., and Lindberg, S. E. (2006). Empirical modeling of atmospheric deposition in mountainous landscapes. Ecological Applications, 16(4):1590–1607.

Weller, H. G., Tabor, G., Jasak, H., and Fureby, C. (1998). A tensorial approach to computational continuum mechanics using object-oriented techniques. Computers in physics, 12(6):620–631.

Whitehead, K. and Hugenholtz, C. H. (2014). Remote sensing of the environment with small unmanned aircraft systems (UASs), part 1: a review of progress and challenges. Journal of Unmanned Vehicle Systems, 2(3):69–85.

Whyard, S. (2015). Personal communication.

Wilby, R. L., Orr, H., Watts, G., Battarbee, R. W., Berry, P. M., Chadd, R., Dugdale, S. J., Dunbar, M. J., Elliott, J. A., Extence, C., Hannah, D. M., Holmes, N., Johnson, A. C., Knights, B., Milner, N. J., Ormerod, S. J., Solomon, D., Timlett, R., Whitehead, P. J., and Wood, P. J. (2010). Evidence needed to manage freshwater ecosystems in a changing climate: Turning adaptation principles into practice. Science of the Total Environment, 408(19):4150–4164.

Wüest, A. and Lorke, A. (2003). Small-scale hydrodynamics in lakes. Annual Review of Fluid Mechanics, 35(1):373–412.

Xu, L. and Baldocchi, D. D. (2003). Seasonal trends in photosynthetic parameters and stomatal conductance of blue oak (Quercus douglasii) under prolonged summer drought and high temperature. Tree Physiology, 23(13):865–877.

Zhang, F., Wang, J., Thon, J., Thon, C., Litchman, E., and Tan, X. (2014). Gliding robotic fish for mobile sampling of aquatic environments. In 2014 IEEE 11th International Conference on Networking, Sensing and Control, pages 167–172. IEEE.

Zhang, Y., Godin, M. A., Bellingham, J. G., and Ryan, J. P. (2012). Using an autonomous underwater vehicle to track a coastal upwelling front. IEEE Journal of Oceanic Engineering, 37(3):338–347.

Appendix A

Supporting Information for Chapter 2

A.1 Equipment and sensors

(a)  (b) 

Figure A.1: a) Trough-style throughfall and b) Juvik-type radial (Juvik and Nullet, 1995) fog collectors.

(a) 

(b) 

(c) 

Figure A.2: a) Leaf wetness sensor (Decagon LWS); b) soil moisture sensor (Decagon 5TM time domain reflectometers); and c) weather station (HOBO H21-002 Micro Station).

A.2 Examples of data sets

Time-lapse imagery

(a)  (b) 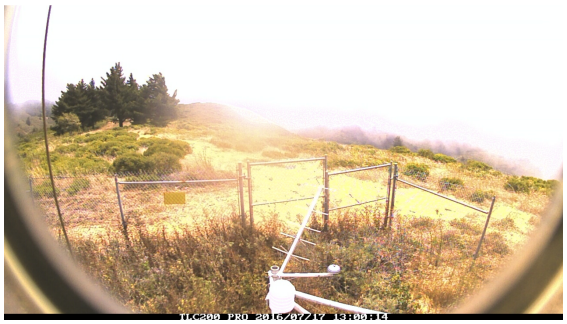

Figure A.3: Typical time-lapse images classified as a) "clear" and b) "fog everywhere."

(a)  (b) 

Figure A.4: Typical time-lapse images classified as a) "fog over ridge" and b) "fog in valley."

Landsat records

(a)  (b) 

Figure A.5: Landsat images show clear skies over the Peninsula Watershed and its subwatershed, the Upper Pilarcitos Creek Watershed.

(a) 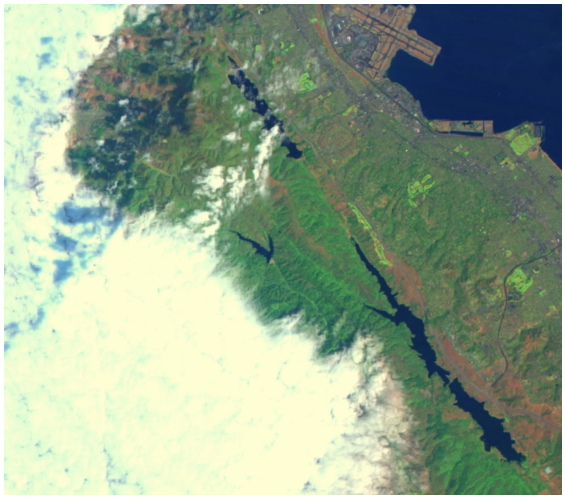 (b) 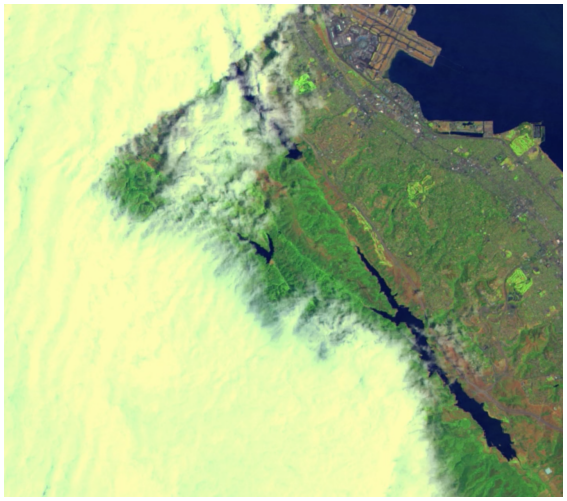

Figure A.6: Landsat images show fog on the western ridge of the watershed.

(a) 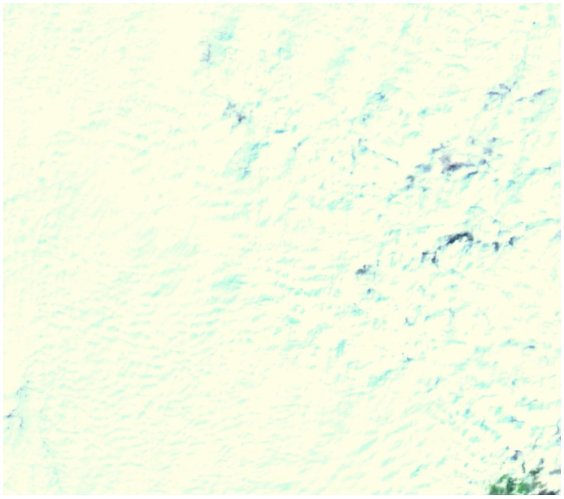 (b) 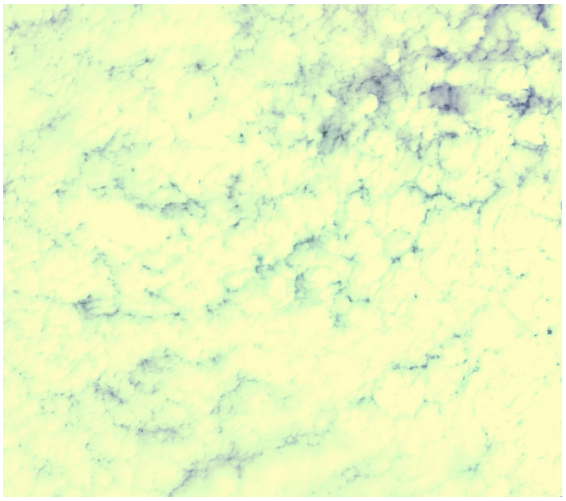

Figure A.7: Landsat images show foggy skies over the entire watershed.

A.3 Isotope sampling

Date	Type	Site	Date	Type	Site
6/17/2014	fog water	SP1	8/26/2014	soil (300 mm)	
7/9/2014	fog water	SP1	8/26/2014	stem	SP1
7/9/2014	fog water	CR	8/26/2014	streamflow	
7/9/2014	soil (75 mm)		9/5/2014	soil (75 mm)	
7/9/2014	stem	SP1	9/5/2014	soil (300 mm)	
7/9/2014	streamflow		9/5/2014	stem	SP1
7/21/2014	fog water	SP1	9/5/2014	stem	LWS2
7/21/2014	fog water	CR	9/5/2014	stem	CR
7/21/2014	fog water	SVR	9/5/2014	streamflow	
7/21/2014	soil (75 mm)		7/6/2015	soil (75 mm)	
7/21/2014	stem	SP1	7/6/2015	soil (300 mm)	
7/21/2014	streamflow		7/6/2015	stem	SP1
8/8/2014	soil		7/14/2015	stem	MM
8/8/2014	stem	SP1	8/4/2015	stem	SP1
8/8/2014	streamflow		8/21/2015	stem	MM
8/26/2014	soil (75 mm)		9/22/2015	stem	SP1

Table A.1: Dates, types, and sites of samples for isotope analysis. Site legend: CR - Cahill Ridge; LWS1 - leaf wetness sensor 1; MM - Montara Mountain; SP1 - Scarper Peak 1; SVR - Spring Valley Ridge.

Appendix B

Supporting Information for Chapter 4

B.1 Field methods: eDNA filtration

Without stirring up sediment, pump enough water to nearly clog a Sterivex 0.2 μm capsule filter. Clean the sample/filter with Phosphate Buffer Solution (PBS) and pump the capsule dry. Fill with 0.9 ml lysis buffer solution to preserve any DNA.

1. Put on a fresh pair of gloves.
2. Draw water directly from the pond into a 60 ml syringe to rinse the chamber.
3. Draw water from the pond to fill the syringe. Attach the luer-lock end of the Sterivex filter capsule to the syringe and push water through. Repeat the process until first sign of clogging or flow slows significantly.
4. Fill new syringe with 50 ml PBS and push through filter.
5. Keep pumping until capsule is nearly dry.
6. Seal downstream outlet port with clay sealant.
7. Attach the luer-lock end of the filter to a 1 ml syringe that is pre-filled with 0.9 ml cell lysis solution and push solution through filter.
8. Cap luer-lock end of filter capsule with sterile cap.
9. Label capsule with site code and date; label bag with site code and volume of water filtered.
10. Repeat at two other locations at site.

B.2 Lab protocol: eDNA extraction

DNA is extracted from filters with Puregene kit for tissue (Gentra Systems) with slight modification of the manufacturer's fungal DNA extraction protocol (Kirshtein et al., 2007).

1. Dilute proteinase K (20 mg/ml) to 1 mg/ml.
2. Add 0.1 ml proteinase K (1 mg/ml) to filter for final concentration of 0.1 mg/ml.
3. Seal capsule and incubate at 55 °C for 60 min with continual rotation to bathe filter in lysis solution.
4. Drain lysis mix from filter using a sterile syringe.
5. Add 300 µl Protein Precipitation Solution, and vortex vigorously for 20 s at high speed.
6. Centrifuge for 3 min at 13,000–16,000 x g. The precipitated proteins should form a tight pellet. If the protein pellet is not tight, incubate on ice for 5 min and repeat the centrifugation.
7. Pipet 900 µl isopropanol into a clean 2 ml microcentrifuge tube and add the supernatant from the previous step by pouring carefully. Be sure the protein pellet is not dislodged during pouring.
8. Add 1.5 µl Glycogen Solution.
9. Mix by inverting gently 50 times.
10. Centrifuge for 1 min at 13,000–16,000 x g.
11. Carefully discard the supernatant, and drain the tube by inverting on a clean piece of absorbent paper, taking care that the pellet remains in the tube.
12. Add 900 µl 70% ethanol and invert several times to wash the DNA pellet.
13. Centrifuge for 1 min at 13,000–16,000 x g. The precipitated proteins will form an invisible pellet.
14. Carefully discard the supernatant. Drain the tube on a clean piece of absorbent paper, taking care that the pellet remains in the tube. Allow to air dry for 5 min.
15. Add 300 µl DNA Hydration Solution and vortex for 5 s at medium speed to mix.
16. Incubate at 65 °C for 1 h to dissolve the DNA.
17. Clean up step: Following manufacturer's protocol, purify DNA with abbreviated MoBio spin filter cleanup.

B.3 qPCR assay protocol

Prep

Method 1

1. Prepare qPCR master mix:
    - 10 µl qPCR mix (2x)
    - 1 µl primer 1
    - 1 µl primer 2
    - 3 µl water
2. Add 15 µl qPCR master mix to wells.
3. Add 5 µl sample to wells or water for no-template control wells.
4. Seal wells and press down.
5. Vortex well using paper towel.
6. Centrifuge well for 1 min using paper towel and balance well.

Method 2 (USGS, 2007)

1. Prepare qPCR master mix:
    - 10 µl qPCR mix (2x)
    - 2 µl primer 1 (10µM)
    - 2 µl primer 2 (10µM)
    - 5.2 µl water
2. Add 19.2 µl qPCR master mix to wells.
3. Add 0.8 µl sample to wells or water for no-template control wells.
4. Seal wells and press down.
5. Vortex well using paper towel.
6. Centrifuge well for 1 min using paper towel and balance well.

Assay

Rib

Primers:
Ro-ITS primer sets were chosen due to their high sensitivity and stringency compared to the other primer sets (Huver et al., 2015). Rb-ITS primer sets were chosen due to their melting point temperatures and fewer matches to other taxa than Ro-ITS primers (i.e. higher specificity).

- Ro-ITS 3 F: 5-CGTGTTTGGCGATTTAGT-3
- Ro-ITS 3 R: 5-CAAAAATGAAGCAACAGT-3
- Rb-ITS 4 Fa: 5-GGTGGAGCTATGCTCGGGTTGGTA-3
- Rb-ITS 4 Fb: 5-CGGCATGCATATGACTACGGGTGG-3
- Rb-ITS 4 R: 5-AGCAACAGTAACGAAACGTGCATGGTA-3

qPCR using SYBR Green dye (Huver et al., 2015):

1. 94 °C for 5 min
2. followed by 40 cycles of:
    - 94 °C for 30 sec
    - variable annealing temperature ranging from 40–60 °C (optimal at 46 °C) for 30 sec
    - 72 °C for 30 sec
3. 72 °C for 4 min

Bd

Primers:

- ITS1-3 Chytr: 5-CCTTGATATAATACAGTGTGCCATATGTC-3
- 5.8S Chytr: 5-AGCCAAGAGATCCGTTGTCAAA-3

qPCR using SYBR Green dye (Kirshtein et al., 2007):

1. 95 °C for 9 min
2. followed by 50 cycles of:
    - 94 °C for 30 sec
    - 60 °C for 1 min